

Multi-Scale Modeling of Laser Powder Bed Fusion Process for Superalloys

by

Reza Tangestani

A thesis

presented to the University of Waterloo

in fulfillment of the

thesis requirement for the degree of

Doctor of Philosophy

in

Mechanical and Mechatronics Engineering

Waterloo, Ontario, Canada, 2022

© Reza Tangestani 2022

Examining Committee Membership

The following served on the Examining Committee for this thesis. The decision of the Examination Committee is by majority vote.

External Examiner

MOHSEN MOHAMMADI, Ph.D.,
Associate professor
Department of Mechanical Engineering
University of New Brunswick

Supervisor

ÉTIENNE MARTIN, Ph.D.,
Associate Professor
Department of Mechanical Engineering
Polytechnique Montréal

Adjunct Assistant Professor
Department of Mechanical and Mechatronics Engineering
University of Waterloo

Supervisor

KAAN INAL, Ph.D.,
Professor
Department of Mechanical and Mechatronics Engineering
University of Waterloo

Internal Member

MUSTAFA YAVUZ, Ph.D.,
Professor
Department of Mechanical and Mechatronics Engineering
University of Waterloo

Internal Member

CLIFF BUTCHER, Ph.D.,
Assistant Professor
Department of Mechanical and Mechatronics Engineering
University of Waterloo

Internal-External Member

HASSAN BAAJ, Ph.D.,
Professor
Civil and Environmental Engineering
University of Waterloo

Author's Declaration

This thesis consists of material all of which I authored or co-authored: see Statement of Contributions included in this thesis. This is a true copy of the thesis, including any required final revisions, as accepted by my examiners.

I understand that my thesis may be made electronically available to the public.

Statement of Contributions

My contributions to this thesis are outlined below:

- Developed all the experimental DOE, made the G-code for the 3D printer, and handled the extraction and measurement of the samples from the base plates.
- Developed all the FEM models, including the beam scale, HL, and LHL models presented in this thesis. Wrote all the Python and Fortran codes linking the process parameters to the FEM simulations.
- Performed all the experiments for the model calibration and validation. This includes the optical microscopy and melt-pool size measurement, the residual stresses measurement using the XRD machine, and the part distortion using the 3D scanner.
- Wrote all my papers, thesis, and performed edits based on the comments from my co-workers and journal reviewers.

The following co-authors have contributed to the current work as outlined below:

- Professor Étienne Martin (Polytechnique Montréal and Adjunct at University of Waterloo) provided guidance and mentorship throughout the research process, as well as funding and resources to support experimental and simulation activities.
- Professor Lang Yuan (University of South Carolina) supplied portions of the raw materials for the experiments and guided the experimental and simulation analyses.
- Dr. Trevor Sabiston (Former Postdoctoral Fellow, University of Waterloo) helped write the discussions and analyses of the modelling sections, provided mentorship and guidance, and reviewed parts of the work.
- Dr. Waqas Muhammad (Postdoctoral Fellow, University of Waterloo) performed material preparation, provided mentorship and guidance.
- Dr. Apratim Chakraborty (University of Waterloo) conducted and analyzed the experiments, helped write the discussions and analyses, and reviewed the presented experimental results.
- Nicholas Krutz helped with discussions of the modelling sections and reviewed parts of the work.

- Dr. Morteza Ghasri Khouzani (Former Postdoctoral Fellow, University of Waterloo) participated in the editing and writing of the paper.

The following first-author publications related to my PhD thesis have been published or submitted and constitute the body of my PhD thesis:

Chapter 5 – **Tangestani, R.**, Sabiston, T., Chakraborty, A., Muhammad, W., Yuan, L., Martin, É., An Efficient Track-Scale Model for Laser Powder Bed Fusion Additive Manufacturing: Part 1- Thermal Model. *Frontiers in Materials*.

<https://doi.org/10.3389/fmats.2021.753040>

Chapter 6 - **Tangestani, R.**, Sabiston, T., Chakraborty, A., Yuan, L., Krutz, N., Martin, É. An Efficient Track-Scale Model for Laser Powder Bed Fusion Additive Manufacturing: Part 2- Mechanical Model. *Frontiers in Materials*.

<https://doi.org/10.3389/fmats.2021.759669>

Chapter 7 - **Tangestani, R.**, Chakraborty, A., Sabiston, T., Martin, É. Interdependent Influences of the Laser Power and Printing Pattern on Residual Stresses in Laser Powder Bed Fusion Proceedings M2D2021: 9th International Conference on Mechanics and Materials in Design.

Chapter 8 - **Tangestani, R.**, Chakraborty, A., Sabiston, T., Yuan, L., Ghasri-Khouzani, M., Martin, É. Modular Numerical Modelling to Predict Thin Wall Part Failure in Laser Powder Bed Additive Manufacturing.

The research work carried out during my PhD has also contributed to the following publications. These published articles do not directly influence the achievement of the research objectives. However, some of the publications provide further insight on the modelling methodologies covered in this thesis.

Journal Articles:

Article 1 - Chakraborty, A., **Tangestani, R.**, Batmaz, R., Muhammad, W., Plamondon, P., Wessman, A., Yuan, L., & Martin, É. (2022). In-process failure analysis of thin-wall structures made by laser powder bed fusion additive manufacturing. *Journal of Materials Science and Technology*, 98. <https://doi.org/10.1016/j.jmst.2021.05.017>

Article 2 - Chakraborty, A., **Tangestani, R.**, Muhammad, W., Sabiston, T., Masse, J.-P., Batmaz, R., Wessman, A., & Martin, É. (2022). Micro-cracking mechanism of RENÉ 108 thin-wall components built by laser powder bed fusion additive manufacturing. Materials Today Communications, 30. <https://doi.org/10.1016/j.mtcomm.2022.103139>

Article 3 - Chakraborty, A., **Tangestani, R.**, Sabiston, T., Esmati, K., Yuan, L., & Martin, E. (2022). Mitigating inherent micro-cracking in laser additively manufactured RENÉ 108 thin-wall components. Additive Manufacturing. Under Review. June 2022.

Article 4 - Batmaz, R., Zardoshtian A., Sabiston T., **Tangestani, R.**, Chakraborty, A., Krutz, N., Pendurti, S., Natarajan A., Martin, E. (2022). An Investigation into Sinterability Improvements of 316L Binder Jet Printed Parts. Metallurgical and Materials Transactions A.

<https://doi.org/10.1007/s11661-021-06564-3>

Conference Proceedings:

Conference 1 - Chakraborty, A., **Tangestani, R.**, Sabiston, T., Krutz, N., Yuan, L., & Martin, E. (2022). Effect of build height on micro-cracking of additively manufactured superalloy RENÉ 108 thin-wall components. TMS 2022 Annual Meeting and Exhibition.

Technical talks:

Talk 1 - **Tangestani, R.**, Chakraborty, A., (2022). High- γ' Ni-based superalloys thin-wall part fabrication by laser powder bed fusion. GE technical presentation. April 28, 2022.

Talk 2 - **Tangestani, R.**, (2022). Material Properties and Boundary Conditions Calibration for Curing Process. GE technical presentation. July 12, 2022.

Abstract

Laser powder bed fusion (LPBF) is an additive manufacturing (AM) technique to fabricate complex geometries with minimal material waste. Over three hundred printing parameters can be altered to control the final part quality. Some significant factors include the laser power, speed, printing pattern, and part geometry. The parameters must be optimized to suit the type of material used. Accordingly, it is not efficient to use experimental methods as they are costly and time-consuming. This makes finite element analysis (FEA) a viable candidate to identify the optimal printing parameters based on parametric analysis. However, computational cost increases with the necessity for improved resolution in the predicted results (such as capturing stress directionality). This thesis presents a novel multi-scale model based on finite element modelling methods. The term multi-scale model is used because the model allows LPBF stress-temperature prediction at the micron scale (within the laser track) and at the part scales (cm) as additional layers are built. The model also enables simulation in a reasonable time frame for industrial application.

Firstly, a novel hybrid line (HL) heat input model was developed to overcome the step time limitation inherent in the beam-scale model. The HL model was calibrated using mechanical and thermal properties of high gamma-prime Ni-based superalloys and the predicted nodal temperature was compared with results obtained from the exponentially decaying (ED) heat input model. Two sets of design of experiments (DOEs) were used to validate the model both thermally and mechanically. The first DOE was designed to validate the thermal part of the simulation. This includes printed single tracks on a layer of RENÉ 65 powder using six different laser speeds and three different laser powers. The results showed that the HL and ED models are equally accurate in predicting cooling rates and nodal temperatures, essential to simulate the in-process strain and stress. In the second DOE, twelve components were printed using three laser powers and four different printing patterns and residual stress was measured using X-ray diffraction (XRD). The predicted results were in good agreement with the experimental results and the average stress error was below 4% of the yield stress at room temperature. The HL model accurately captures the stress directionality and significantly decreases the computational time. The HL model can become over 1,500 and 30 times faster than the ED model for the thermal and mechanical models, respectively.

Secondly, a multi-scale model was developed using a combination of the HL model and lumping approach. This new lumped HL (LHL) model allows laser track-powder layer lumping, which can be adapted to optimize computational efficiency for the desired accuracy. This enables simulation of the stress directionality in LPBF at the part-scale level. The LHL model was calibrated using the mechanical and thermal properties of high gamma-prime Ni-based superalloys. The model was validated by comparing the final part distortion (measured with a 3D scanner) to the simulation results of LPBF thin-wall components. Two different printing patterns were used for the validation of the model and the final experimental errors were found to be below 10% of the local deformation.

Finally, the two models were used to perform parametric studies on LPBF high gamma prime Ni-based superalloys. The HL model was first used to evaluate the effect of scanning pattern and laser power. The results show that vector length and scanning strategies have stronger effect on the residual stresses. Shorter vector length creates more compressive stresses while longer vector length generates more tensile stresses along the longitudinal directions. The laser power and interlayer rotations are also shown to be beneficial for stress reduction and homogenization. Finally, the LHL model was used to study the effect of printing patterns and part geometry on the limiting build height (LBH). This is when part abortion limits the final part height during LPBF. For this study, a DOE of 34 components was created with lengths between 20 mm and 60 mm (with an increment of 10 mm), 8 different printing patterns (with and without scan rotation), and a fixed wall thickness of 0.5 mm. Buckling mechanisms were identified as the major cause of in-process part failure. The best combination was found to be interlayer vector rotations that maximize the vector lengths. The model showed longer vector length promotes reduction of compressive residual stresses and increase in LBH. The part length has a small effect on the LBH but leads to a change in the buckling mechanism.

Acknowledgements

Firstly, I would like to thank both my supervisors, Professors Étienne Martin and Kaan Inal, for their support and motivation during my PhD journey. Throughout my challenging times, Professor Martin was always available for my questions. Professor Inal remained a father-like figure throughout my graduate studies, and he always believed in me when times were tough.

As a second note of gratitude, I wish to thank my dear friend and colleague, Dr. Trevor Sabiston, for his encouragement, motivation, and helps with my papers. Throughout my career and life, Dr. Waqas Muhammad has provided me with invaluable advice on how to achieve success and inspired me to think outside the box. I extend my sincere gratitude to Apratim Chakraborty, without whose superior experimental results I could not have completed my papers and this thesis. I am grateful for him staying up with me all night to discuss work and life, and for being there for me as a brother when I needed him. Thanks to my all my research colleagues and friends, but special thanks go out to Khadijeh Esmati, Solgang Im, Dr. Rasim Batmaz, and Heidar Karimialavijeh. They all provided me with valuable advice and helped me greatly with my experimental work.

I wish to thank Professor Lang Yuan at the University of South Carolina for his assistance in fabricating parts for my experiments. I am grateful to Professor Wessman for his valuable comments and feedback on some of my papers. University of Waterloo (UW) and Polytechnique Montréal (PolyMTL) laboratories provided excellent facilities for the experiment. Throughout my research and experiments, the MSAM, (CM)² and LAPOM management and staff were extremely supportive and accommodating. I am deeply thankful to Natural Sciences and Engineering Research Council of Canada (NSERC) under grant no. RGPIN-2019-04073 and Amber Andreaco, an engineer in GE additive's material supply division, who supported this project.

Finally, I would like to express my gratitude to my parents and brother for being there with me every step of the way, regardless of my emotional swings. “I have nothing except you, and you are the only reason I am moving. Love you all.”

Dedication

*For my parents and younger brother who
have always loved me unconditionally.*

Table of Contents

Examining Committee Membership	ii
Author’s Declaration	iii
Statement of Contributions	iv
Abstract	vii
Acknowledgements	ix
Dedication	x
List of Figures	xv
List of Tables	xxi
Chapter 1 Introduction	1
Chapter 2 Background	4
2.1 Overview of AM	4
2.2 Applications for High Gamma Prime Superalloys	5
2.3 Current Challenges for High Gamma Prime Superalloys in LPBF	6
2.3.1 Residual Stress	7
2.3.2 Microstructural Anisotropy	7
2.3.3 In-Process Part Failure	7
2.4 Finite Element Modeling of LPBF	8
2.4.1 Introduction to FEM	8
2.4.2 Modeling of LPBF Process	9
Chapter 3 Literature Review	12
3.1 Thermal Modeling for LPBF Process.....	12
3.1.1 Models for Heat Input	13
3.1.2 A Few Examples of Effective Parameters in Thermal Model	18
3.2 Thermo-Mechanical Modeling for LPBF Process.....	19
3.2.1 Approaches to Improve the Accuracy of Models	19

3.2.2 Approaches to Improve Computational Efficiency	23
3.3 Knowledge Gap	27
Chapter 4 Research Overview.....	29
4.1 Goal and objectives	29
4.2 Research Strategy	29
4.2.1 Developing a New Line Heat Input Model: Part 1-Thermal Model and Part 2-Mechanical Model (Knowledge Gaps 1&2)	29
4.2.2 Parametric Study on Interdependent Influences of the Laser Power and Printing Pattern on Residual Stress (Knowledge Gaps 2)	30
4.2.3 Developing Lumped HL Model to Simulate the Laser Powder Bed Fusion Process for Large Scale Components (Knowledge Gaps 2&3).....	31
4.3 Research Map	31
Chapter 5 Developing a New Line Heat Input Model: Part 1-Thermal Model	32
5.1 Introduction	33
5.2 Material and Experimental Method.....	34
5.2.1 Material Composition.....	34
5.2.2 LPBF Experimental Procedure.....	35
5.2.3 Melt Pool Characterization.....	35
5.3 Modelling of the Laser Heat Source.....	36
5.3.1 Beam Scale Exponentially Decaying Heat Input Model	36
5.3.2 Track Scale Hybrid Line Heat Input Model	37
5.3.3 Implementation of Heat Dissipation.....	37
5.3.4 Model Implementation in Finite Elements	38
5.4 Results and Discussion.....	44
5.4.1 LPBF Melt Pool Geometry Analyses	44
5.4.2 ED Model Evaluation	46
5.4.3 HL Model Calibration	47
5.4.4 Hybrid Line Model Evaluation.....	48
5.5 Conclusion.....	54
Chapter 6 Developing a New Line Heat Input Model: Part 2-Mechanical Model	56

6.1 Introduction	57
6.2 Material and Experimental Methods	58
6.2.1 Material Composition	58
6.2.2 LPBF Procedure	58
6.2.3 Residual Stress Measurement.....	60
6.3 Modeling	60
6.3.1 Single-Track Models	62
6.3.2 HL Part Scale Model	63
6.4 Results and Discussion.....	67
6.4.1 Comparison Between HL and ED Single Track Models.....	67
6.4.2 Model Computational Efficiency	71
6.4.3 Part Scale Simulation of Residual Stresses	73
6.5 Conclusion.....	79
Chapter 7 Parametric Study on Interdependent Influences of The Laser Power and Printing Pattern on Residual Stress.....	81
7.1 Introduction	82
7.2 Model Description	83
7.3 Results and Discussion.....	85
7.3.1 Computational Time.....	85
7.3.2 Interdependent Influences of the Laser Power and Printing Pattern	87
7.4 Conclusion.....	88
Chapter 8 Developing Lumped HL Model to Simulate the Laser Powder Bed Fusion Process for Large Scale Components	89
8.1 Introduction	90
8.2 Material and Experimental Methods	92
8.2.1 Feed Stock Material.....	92
8.2.2 LPBF Procedure	92
8.2.3 Evaluating the Printed Part Deformations	95
8.2.4 Limiting Build Height Measurement.....	95
8.3 Modeling	96

8.3.1 Simulation of LPBF Process	96
8.4 Model Evaluation	102
8.4.1 Computational Time	102
8.4.2 Model Accuracy	104
8.5 Results	106
8.5.1 Experimental Observations of LBH in Printed Thin-Wall Components.....	106
8.5.2 Part Failure Mechanism Causing LBH.....	108
8.5.3 Simulation of Part Distortion and LBH.....	109
8.6 Discussion	112
8.6.1 The Effect of Printing Pattern on Residual Stresses	113
8.6.2 The Effect of Part Length on Residual Stresses	115
8.7 Conclusion.....	116
Chapter 9 Conclusions and Recommendations	119
9.1 Major Conclusions	119
9.1.1 The Hybrid Line (HL) Model.....	119
9.1.2 The Lumped Hybrid Line (LHL) Model	121
9.2 Recommendations and Future Work	123
References	124

List of Figures

Figure 2-1: Classification of different additive manufacturing processes by feedstock, heat input, and process schematics [20].	4
Figure 2-2: A schematic of the LPBF process a) printing the first layer b) printing the nth layer of part c) finished part after the powder was removed [24].	5
Figure 2-3: (a) Distortion Profile of AlSi10Mg, and (b) Distorted Thin-Wall Sample (Taken from [38]).	8
Figure 2-4: Nodes and Integration points in elements a) Full integration b) Reduced integration. Yellow points show the position of integration points and green points show the nodes.	9
Figure 3-1: A schematic of the Gaussian heat input model.	14
Figure 3-2: A schematic of the semi-spherical heat input model.	15
Figure 3-3: A schematic of Goldak heat input model.	16
Figure 3-4: Comparisons of the heat input models based on the melt pool dimensions [57].	17
Figure 3-5: a) The schematic of island printing pattern. b) The meshing technique used to reduce the computational time [53].	19
Figure 3-6: An example of predicted melt pool in simulation [24].	21
Figure 3-7: Comparison of experimentally measured [77] and numerically computed (a) longitudinal residual stress and (b) through-thickness residual stress during the laser deposition [24].	22
Figure 3-8: Required number of elements with and without mesh-to-mesh solution mapping.	23
Figure 3-9: The accuracy of predicted displacement verses the time step size.	25
Figure 4-1: An interactive map showing correlations between paper-based research strategies.	31
Figure 5-1: a) Single track DOE parameters and configuration on the powder bed substrate. b) Optical microscope image showing R65 single track melt pool produced by LPBF with a laser speed of 800 mm/s and power of 200 W.	36
Figure 5-2: Meshed 3D model for the FE simulations. The powder layer and substrate are 0.04 and 0.96 mm thick, respectively. Mesh sizes for the powder are finer (10 μm) compared to the substrate to increase computational efficiency. The red line along the x-direction shows the laser path where the nodal temperatures are evaluated.	39
Figure 5-3: a) Experimental and modified temperature-dependent specific heat capacity and b) heat conduction as a function of temperature for R65.	40

Figure 5-4: ED model simulation showing the material state transition and temperature distribution. In a), the powder (blue) and liquid/solid (red) zones are shown. b) Nodal temperature during the process. In c), a schematic of the material state transition occurring in the melt pool is shown. 42

Figure 5-5: Nodal temperatures are shown in increments a) n and b) $n + 1$. The material state transition showing the lag effect in increment c) n and d) $n + 1$. The modified material state transition is shown in increment e) n and f) $n + 1$ without lag. Powder state is shown in blue and liquid/solid state is shown in red. The black ellipsoid shows the location of the applied heat. 43

Figure 5-6: Comparison between experimental and ED simulation melt pool widths and depths for different laser powers: (A) and (B) 180 W (C) and (D) 200 W, and (E) and (F) 220 W. 44

Figure 5-7: a) Effect of linear energy density (J/mm) on the experimental melt pool aspect ratio (depth over width). b) Melt pool cross-section obtained with a laser power of 220 W and laser speed of 800 mm/s. The red dashed line outlines the melt pool boundary. 46

Figure 5-8: Temperature variation surrounding the melt pool for the ED heat input model with 200 W laser power and 1,000 mm/s laser speed. The melted zone is shown in grey, the melt pool in light red, the powder state in blue, and the substrate in dark blue. 47

Figure 5-9: Example of an ED laser track simulation used for HL model calibration. The melt pool is shown in grey color. The nodal temperatures of the elements surrounding the melt pool are used for calibration of the HL model. The highlighted region (red cube) at the center of the cross section at the melt pool boundary is used to study the cooling rate in cooling rate. 48

Figure 5-10: Comparison of $Time_{ED} / Time_{HL}$ as a function of τ showing the computational efficiency of the HL model compared to the ED model. 49

Figure 5-11: Comparison of the experimental and HL simulation ($\tau = 5$) melt pool a) depth and b) width for 200 W laser power. 50

Figure 5-12: Nodal temperatures along laser paths in the ED model and the HL model for $\tau = 5$ and $\tau = 10$. The laser powers and speeds are a) 220 W–800 mm/s b) 200 W–1,000 mm/s and c) 180 W–1,300 mm/s. 51

Figure 5-13: Cooling rate profiles for the following laser powers and speeds: a) 220 W–800 mm/s b) 200 W–1,000 mm/s, and c) 180 W–1,300 mm/s. 53

Figure 5-14: Temperature distributions captured 1.2 ms after the track simulation finishes for a) the ED beam scale and b) the HL track-scale model ($\tau = 10$). 54

Figure 6-1: a) The four different printing patterns used to compare the HL models with experimental results. The perpendicular and longitudinal patterns have short (0.5 mm) and long (5 mm) vector lengths with zero rotation angle between the layers. The 90° and 45° rotations patterns have counterclockwise rotation of the laser direction after each layer. b) An example of the 45° rotation pattern is given for four layers..... 59

Figure 6-2: Track-scale model mesh showing the dimensions of the substrate and powder bed. The laser movement is parallel to the X-direction. The residual stresses are evaluated along the two lines highlighted in red..... 63

Figure 6-3: Part-scale meshed 30-layer model used to simulate the 12 different LPBF builds (3 powers and 4 scanning patterns shown in Figure 6-1). The dashed blue line shows the border between the printed layers and the substrate. The residual stresses are taken along the line shown in red..... 64

Figure 6-4: Flowchart of the computational framework including subroutines (blue) and interactions with customized Python programs. 65

Figure 6-5: Mesh-coarsening algorithm showing mesh evolution with the number of layers. For each layer, a new model is created and the results from the previous model are mapped as initial conditions for the new model. A python code is used to transfer nodal displacements between models. 66

Figure 6-6: Von Mises stress (Pa) distributions for the a) ED and b) HL ($\tau = 5$), c) HL ($\tau = 10$), d) HL ($\tau = 20$) models after cooling (10 s) and relaxing the part constraints. The laser power is 200 W, and the speed is 1,000 mm/s for all four images. 68

Figure 6-7: Single-track residual stress distributions along line 1 in Figure 6-2 for ED and HL models. a) von Mises b) SXX c) SY Y d) SZZ stresses. 69

Figure 6-8: Single-track residual stress distributions along line 2 in Figure 6-2 for ED and HL models. a) von Mises b) SXX c) SY Y d) SZZ stresses. 70

Figure 6-9: Comparison of $Time_{ED}Time_{HL}$ as a function of τ for the single-track mechanical models. 71

Figure 6-10: Comparison between the measured and predicted residual stresses in the x-direction (Sxx) evaluated at the center of the specimens. For each specimen ID, the first number refers to the laser power and the second number represents the scanning strategy given in Figure 6-1..... 74

Figure 6-11: Residual stress (Pa) comparison between the three laser powers for the transverse scanning patterns in Figure 6-1. The residual stresses are shown along a centerline cross section of the

part-scale simulations. Longitudinal stress (S_{xx}) for laser power a) 180 W and b) 220 W. Build direction stress (S_{zz}) for laser power c) 180 W and d) 220 W. Von Mises stress for laser power e) 180 W and f) 220 W. 75

Figure 6-12: Longitudinal residual stress (S_{xx} (Pa)) comparison between the four scanning patterns described in Figure 6-1 a) Perpendicular, b) longitudinal, c) 90° rotation and d) 45° rotation. The residual stresses are shown along a centerline cross section of the part-scale simulations. 77

Figure 6-13: Build direction residual stress (S_{zz} (Pa)) comparison between the four scanning patterns described in Figure 6-1 a) Perpendicular, b) longitudinal, c) 90° rotation, and d) 45° rotation. The residual stresses are shown along a centerline cross section of the part-scale simulations. 77

Figure 6-14: Transverse residual stress (S_{yy} (Pa)) comparison between the four scanning patterns described in Figure 6-1 a) Perpendicular, a) longitudinal, c) 90° rotation and d) 45° rotation. The residual stresses are shown along a centerline cross section of the part-scale simulations. 78

Figure 7-1: a) The 30-layer part was used to simulate the LPBF builds. The dashed blue line shows the border between the printed layers and the substrate. b) Two different printing patterns (90° and 45° rotation angles) were used to study the interdependent influences of laser power and printing pattern. 83

Figure 7-2: The algorithm for preparing and mapping the deformation to an updated model with coarser elements. Blue rectangles indicate the extracted section from each file 85

Figure 7-3: a) The required time to read, prepare, and writ the *.INP file. b) The processing time to map the deformation using griddata tool for each layer with respect to the number of elements in the fine layer..... 86

Figure 7-4: The residual stress following the completion of simulation. The parts are sectioned at the center along the X-direction and the laser powers and rotation angles used are a) 180W-90°, b) 220W-45°, c) 180W-90°, d) 220W-45°, respectively. The black circles highlight the regions demonstrating the effect of printing patterns on residual stress magnitude. 88

Figure 8-1: The DOE and configuration of the thin-wall components on the build plate shown in a) top 2D view and b) 3D view. All components, except the two used for validation, have identical thicknesses and heights, but varying lengths and printing patterns. Parts with identical lengths are grouped and labelled using color codes. Annotations are added to describe printing patterns (1, 2, 3, etc.,) detailed in Table 8-1. 93

Figure 8-2: Schematic of the track angle and printing pattern rotation. Small scanning angles result in long vector lengths and large vector angles produce short vector lengths. For example, a track angle (θ) of 90° corresponds to a vector length aligned with the part thickness. 95

Figure 8-3: LBH measurement criteria for a) partial and b) complete part failure. The red lines indicate the end positions of the LBH measurements. 96

Figure 8-4: Flowchart of the computational framework including subroutines (blue) and interactions with customized Python programs 98

Figure 8-5: Schematic showing a) single HL, b) layer lumping, c) laser track lumping, d) three-layer-three-track lumping, e) layer heating modelling techniques. 100

Figure 8-6: Part-scale meshed model to simulate the process for different LPBF parameters. Sections are colored to distinguish element sizes in Table 8-2..... 102

Figure 8-7: Computational time associated with part thickness and length for the eight printing patterns investigated here. The part height is kept constant at 16 mm. The error bars show the variation between the required time to simulate different printing patterns. 104

Figure 8-8: A comparison between simulation and experimental measurement of part distortion. Two different scanning strategies are compared. The deformations created by the “EL” scanning strategy, obtained from a) simulation and b) experimental measurement, and by the “ES” scanning strategy, obtained from c) simulation and d) experimental measurement, are demonstrated. 105

Figure 8-9: LBH of the as-built thin-wall parts processed under the conditions described in Table 8-1. The LBH values for components scanned with the a) printing patterns without inter-layer scan rotations, and b) printing patterns with inter-layer scan rotations are shown. Data for the 1 mm thick components (green) is derived from literature (Chakraborty et al. 2021). The gray and green dotted lines denote the target heights for 0.5 mm and 1 mm part thicknesses, respectively. 107

Figure 8-10: The two types of failure observed causing the LBH during LPBF process reported in Figure 8-9. Type one a) front and b) side views show a clear rupture along the centerline due to buckling in the X-Z plane. Type two c) front and d) side views show failure localized at part corners due to a combination of buckling in the X-Z (rotation along the X axis) and Y-Z planes (rotation along the Z axis). 109

Figure 8-11: Comparison between simulation and experimental distortion for 6 components with various dimensions fabricated using different printing patterns. The printing pattern and wall length are given above each figure. All thin-wall components are equally thick (0.5 mm)..... 110

Figure 8-12: Comparison between observed and simulated LBH for a) “ES” and b) “EL” printing patterns. 111

Figure 8-13: A schematic of the simulated laser track and the newly deposited layer illustrated with the distorted element (yellow color) causing model termination. 112

Figure 8-14: Stress along the build direction (SZZ) for the 8 different printing patterns investigated. The parts’ thickness, length and height are 0.5 mm, 30 mm and 17 mm, respectively. The printing patterns are labelled on top of each component according to labelling described in Table 8-1. The residual stresses are shown along a centerline cross section of the parts. 114

Figure 8-15: Longitudinal stress for the 8 different printing patterns investigated. The common part thickness, length and height are 0.5 mm, 30 mm and 17 mm, respectively. The printing patterns are labelled on top of each component as shown in Table 8-1. The residual stresses are shown along a centerline cross section of the parts..... 115

Figure 8-16: Comparison between a) build direction (SZZ) and b) longitudinal (SXX) residual stresses for three different part lengths. The part lengths are labelled above each component. The printing pattern is “ES”, the part height is 17 mm, and the wall thickness is 0.5 mm. The residual stresses are shown along a centerline cross-section of the parts..... 116

List of Tables

Table 2-1: Commercial Ni-based Single-Crystal Superalloys Used in Gas Turbine Engines [2].	6
Table 5-1: Comparison of the melt pool depths and widths for the ED models and experiments with increasing laser speed and power.	45
Table 5-2: Error in temperature prediction between ED and HL models for different temperature domains. The laser power and speed are 200 W and 1000 mm/s, respectively (Figure 5-12 (b)).	52
Table 6-1: Temperature-dependent thermal material properties for RENÉ 65	62
Table 6-2: Element size, in microns, for each meshed layer of the part-scale simulation.....	67
Table 6-3: Computational time (hours) comparison between the ED beam-scale and HL ($\tau = 10$) part-scale models with and without the mesh coarsening technique.	72
Table 8-1: The printing patterns used to manufacture the thin-wall components. The scan angles for the first 5+n layers are included under the column group labelled track angle. Each printing pattern corresponds to the label presented under the "Named as" column. The following nomenclature system is used: "EL" – extra-long; "L" – long; "S" – short; "ES" – extra-short; "EL-ES" – extra-long-extra-short; "L-L" – long-long; "S-S" – short-short; and R – random. "EL", "L", "S" and "ES" represent printing patterns without inter-layer rotations, while "El-ES", "L-L", "S-S" and "R" represent printing patterns with scan rotations between layers.	94
Table 8-2: Element size in micron for each meshed layer of the part-scale simulation.	102

Chapter 1

Introduction

Additive manufacturing (AM) is a promising technology to produce complex shapes with minimal waste [1]. Compared to conventional manufacturing techniques, AM technologies such as laser powder bed fusion (LPBF) produce near-net-shape parts reducing the time between design and final production [2]. AM has wide application potentials in aerospace [3], automotive [4], biomedical [5], and energy industries [6], [7]. Many industries are trying to adopt AM technologies to develop a competitive edge in the global market. The aerospace industry is attempting to use LPBF for the fabrication of complex parts for high-temperature applications. Gas turbine engines, for instance, consist of parts with very thin geometries and tight tolerances, and require materials which can maintain strength at high operating temperatures. To meet the criteria for high-temperature application in gas turbine engines, high-strength Ni-based superalloys with a high volume fraction of γ' precipitates need to be manufactured. However, fabrication of thin-wall parts using LPBF poses many in-process challenges such as excessive residual stress [8], microstructural anisotropy [9], and in-process part failure [10].

During LPBF processing, parts experience high thermal gradients and repetitive localized heat transfer, resulting in distortion and residual stress [11]–[14]. This adversely affects the structural integrity, geometrical tolerances and dimensional stability of the parts [15]. During the LPBF process, there are numerous printing parameters, including line energy, printing pattern, inter-layer rotation angle, and part geometry, which can affect the as-built part quality. An expensive and time-consuming trial-and-error method is commonly used to determine optimal conditions for printing LPBF parts without build failures. An efficient finite element analysis (FEA) tool could be applied to accurately predict build failures before the actual manufacturing process to reduce the number of costly experimental iterations and produce a functional AM part [16]. The main challenge in using the large scale finite element (FE) models is the enormous computational cost to calculate the results with enough accuracy (such as stress directionality) for parametric study. The FE model requires a large number of elements and time increments to predict the results accurately. For larger parts, more elements are required, which substantially increases the degree of freedom (DoF) and computational costs [17]. Best-case computational times (achieved using powerful clusters) can reach a few days or weeks and the largest simulated part is relatively small [18]. To overcome this problem, researchers use a larger heat input

technique called flash heating (layer heating) where the entire layer is heated in one increment [19]. However, these techniques ignore the stress directionality, which is highly important for thin-wall components and studying the effect of printing pattern. Furthermore, the model creation process takes time as a large number of inputs are required. Therefore, the existing models offer limited applications and are not suitable for accurate parametric evaluations.

The goal of this research is to develop a multi-scale thermo-mechanical model to maximize the speed while maintaining the accuracy of the part-scale simulation, which is essential for parametric evaluations. The emphasis is to study the effect of printing parameters such as laser power, speed, printing pattern, and part geometry on superalloy thin-wall builds. Process parameter optimization enables reduction of residual stress, in-process part failure, and unwanted part deformations in hard-to-weld high- γ' Ni-based superalloy thin-wall components produced by LPBF. Brief summaries of the subsequent chapters are provided below:

Chapter 2 provides a background of the additive manufacturing process, the Ni-based superalloy, problems associated with using high-gamma prime superalloys for LPBF, and an introduction to the finite element method.

Chapter 3 the essential literature concerning the thermal and mechanical models to simulate AM processes and the knowledge gaps in literature are presented.

Chapter 4 analyzes the research strategy and map linking the research work to the thesis goal. Detailed content overviews are provided for each chapter.

Chapter 5 presents the first part of developing a novel line heat input model for high gamma prime superalloy. This chapter focuses on thermal modeling and replicate the process of printing single tracks. The influence of laser speed and power on the melt pool size is parametrically evaluated.

Chapter 6 is the second part of line heat input model development. This includes the mechanical part of the simulation and analysis of the calculated result accuracy. The parametric evaluation is conducted to study the effect of laser power and printing pattern on the residual stress.

Chapter 7 explains the interdependence effect between laser power and printing pattern using simulations developed in the previous chapter.

Chapter 8 presents a novel framework to simulate full-scale components for parametric studies. A large DOE of experimental and simulation results is created. This is used to study the effect of printing pattern and thin-wall geometry on the limiting build height.

Chapter 9 summarizes the major conclusions from the PhD research and provides recommendations to improve thin-wall part processability and quality.

Chapter 2

Background

2.1 Overview of AM

Additive manufacturing (AM) is a cutting-edge technology to build three-dimensional (3D) parts with complex shapes. The AM processes have different operating principles, feedstock materials, and means of layer deposition. Processes such as laser powder bed fusion (LPBF), direct metal laser sintering (DMLS), and fused deposition modeling (FDM) melt or soften materials to build the layers (Figure 2-1). The processes are categorized by the type of heat source and feedstock. The speed, cost, and color capability of the feedstock are the main considerations to choose a machine for manufacturing [1], [2]. Recently, there has been a significant push towards using AM for structural aerospace applications due to the inherent design freedom of the process. To build metal parts, AM processes such as DMLS and LPBF are emphasized for industrial use [2]–[4].

Additive Manufacturing (AM) Processes														
Process	Laser Based AM Processes					Extrusion Thermal	Material Jetting	Material Adhesion	Electron Beam					
	Laser Melting		Laser Polymerization											
Process Schematic														
Name Material	SLS	■	DMD	■	SLA	■	FDM	■	3DP	■	LOM	■	EBM	■
	SLM	■	LENS	■	SGC	■	Robocasting	■	IJP	■	SFP	■		
	DMLS	■	SLC	■	LTP	■			MJM	■				
			LPD	■	BIS	■			BPM	■				
					HIS	■			Thermojet	■				
Bulk Material Type		Powder	■	Liquid	■	Solid	■							

Figure 2-1: Classification of different additive manufacturing processes by feedstock, heat input, and process schematics [20].

For the LPBF process, an operator uses a computer-aided-design (CAD) software to create a 3D model of the part and a computer-aided-manufacturing (CAM) software to analyze the model and determine

a manufacturing plan [17]. The software divides the part into several layers in correspondence with the powder layer thickness and sends the translated file as a code (G-code) to the LPBF machine. The LPBF machine uses the code and places a layer of powder on a movable platform (base plate) (Figure 2-2). The laser follows the designed scan pattern of the first layer creating the first layer of the part, then a new layer of powder is deposited and the second layer is processed (Figure 2-2 (a)). This process is repeated until the last layer is printed (Figure 2-2 (b)). Then the operator removes the part from the chamber and cleans the powder with a brush (Figure 2-2 (c)) [21].

Material properties need to be tailored according to the part application. LPBF is a premium method to print high-quality parts with a vast array of materials and properties. Common applications include the construction of aerospace components such as turbine blades and fuel injectors [22]. These parts need to sustain properties such as Young's modulus and plastic flow at elevated operating temperatures. Superalloys are good candidates for applications that require materials with high resistance to temperature and creep [12], [23].

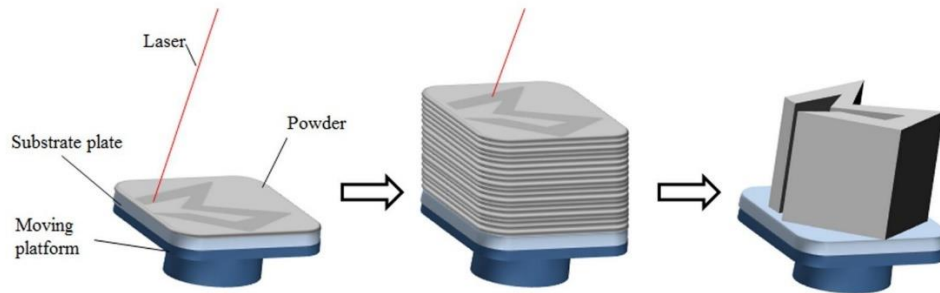


Figure 2-2: A schematic of the LPBF process a) printing the first layer b) printing the nth layer of part c) finished part after powder removal [24].

2.2 Applications for High Gamma Prime Superalloys

Superalloys represent a class of metal alloys exhibiting high strength relative to other alloys at elevated temperatures (between 540 °C and 1100 °C). They are strong and very suitable for high-temperature applications (such as turbine blades) due to the unique strengthening effect of the ordered face-centred-cubic (FCC) gamma-prime (γ') phase within the FCC gamma (γ) phase [25]. In addition to aerospace applications, superalloys are useful for marine, nuclear reactors, submarines, steam power plants, and petrochemical equipment [25]. Categories usually include nickel-based, iron-based, and cobalt-based

superalloys. The Ni-based superalloys have shown the highest phase stability (maintains FCC structure) at medium to high temperatures and are more widely used in the hot zone of the aircraft gas turbine engines [14], [26], [27].

These alloys are primarily made up of an average composition of 60 wt% nickel (Ni), 10 wt.% chromium (Cr), 6.5 wt.% aluminum (Al) and titanium (Ti), 7.5 wt.% molybdenum (Mo) and W, 2.5 wt.% niobium (Nb) and tantalum (Ta), 0.6 wt.% iron (Fe), 8.8 wt.% cobalt (Co), 0.1 wt.% carbon (C), 0.08 wt.% boron (B) and zirconium (Zr), and 0.3 wt.% hafnium (Hf) [28]. However, as observed in Table 2-1, the composition differs based on the desired material properties.

Table 2-1: Commercial Ni-based Single-Crystal Superalloys Used in Gas Turbine Engines [2].

Generation	Superalloy	Element Weight %												
		Cr	Co	Mo	W	Ta	Re	Nb	Al	Ti	Hf	C	B	Y
First	PWA 1480	10.0	5.0		4.0	12.0			5.0	1.5				
	René N4	9.8	7.5	1.5	6.0	4.8		0.5	4.2	3.5	0.15	0.05	0.00	
	CMSX-3	8.0	5.0	0.6	8.0	6.0			5.6	1.0	0.10			
Second	PWA 1484	5.0	10.0	2.0	6.0	9.0	3.0		5.6		0.10			
	René N5	7.0	7.5	1.5	5.0	6.5	3.0		6.2		0.15	0.05	0.00	0.01
	CMSX-4	6.5	9.0	0.6	6.0	6.5	3.0		5.6	1.0	0.10			
Third	René N6	4.2	12.5	1.4	6.0	7.2	5.4		5.8		0.15	0.05	0.00	0.01
	CMSX-10	2.0	3.0	0.4	5.0	8.0	6.0	0.1	5.7	0.2	0.03			

2.3 Current Challenges for High Gamma Prime Superalloys in LPBF

Despite the outstanding high-temperature performance, Ni-based superalloys have limited weldability due to the presence of a high γ' volume fraction (directly linked to the Ti + Al content). The LPBF process can be alternatively viewed as a multilayer/repeated welding process, which is associated with rapid cooling rates up to 10^4 K/s [29], [30]. This results in the formation of significant residual stresses as well as epitaxially grown microstructure, both resulting in structural integrity issues, anisotropy in mechanical properties, cracking, and in severe cases part failure [17], [18].

2.3.1 Residual Stress

Residual stress is defined as stationary stress at equilibrium within a material [18], [31]. In LPBF, the residual stresses developed during layer-by-layer processing are known to be complex and large, potentially causing part failure during manufacturing [32]. This is attributed to the large thermal gradients from localized rapid heating and cooling during processing. In general, the presence of residual stress (especially tensile residual stress) within AM parts is undesirable as it reduces the effective fatigue and tensile properties, and may distort the final geometry and induce cracks [20], [24]. When the residual stress overcomes the yield strength of the material, it causes distortion. Significant effort has been invested in the control and reduction of residual stresses in AM [21], [22], [33].

2.3.2 Microstructural Anisotropy

The rapid solidification, combined with the directionality in heat loss vertical to the base plate, results in epitaxial growth in LPBF [33], [34]. Some variability was observed in LPBF-fabricated structures, whereby the use of a chessboard scanning strategy (in which the laser moves randomly between square islands to evenly distribute the heat) resulted in the formation of nearly equiaxed grains embedded within primarily columnar grain regions [35]. Most Ni-based superalloy AM builds show either considerable levels of interdendritic segregation or other undesirable solidification-induced phases (e.g., Laves phase) [36]. As a result, there is always a need for a post-processing treatment, such as hot isostatic pressing (HIP) to heal the defects caused by the AM processes. Supplementary solution and ageing heat treatment is required to optimize the size and fraction of precipitates for high-temperature properties. These post-processing operations add to the cost of the AM process [37].

2.3.3 In-Process Part Failure

Part failure is a major concern during LPBF processing. Few authors have explored how thin-wall parts processed using LPBF are affected by build part thickness. As an example, Ahmed et al. [38] reported significantly higher distortion below 0.8 mm wall thickness (Figure 2-3 (a)). According to the authors, decreasing the wall thickness leads to increased thermal strains, shrinkage, and bending. Due to increased susceptibility to residual stresses developed by laser heat thermal cycling, samples between 0.5 and 1.5 mm showed statistically larger variations in distortion (Figure 2-3 (b)). Chakraborty et al. [10] showed that parts begin to fail below 1 mm wall thickness. The limiting build height (LBH)

terminology was used to define the part failure mechanism. The LBH is defined as the highest point from the base plate achievable without part failure. According to the authors, compressive residual stresses in the build direction increase the buckling susceptibility in the thin-wall components. Buckling generates large deformation which displaces the solidified layer from its original position. This adversely affects subsequent layer deposition, which could ultimately lead to part failure.

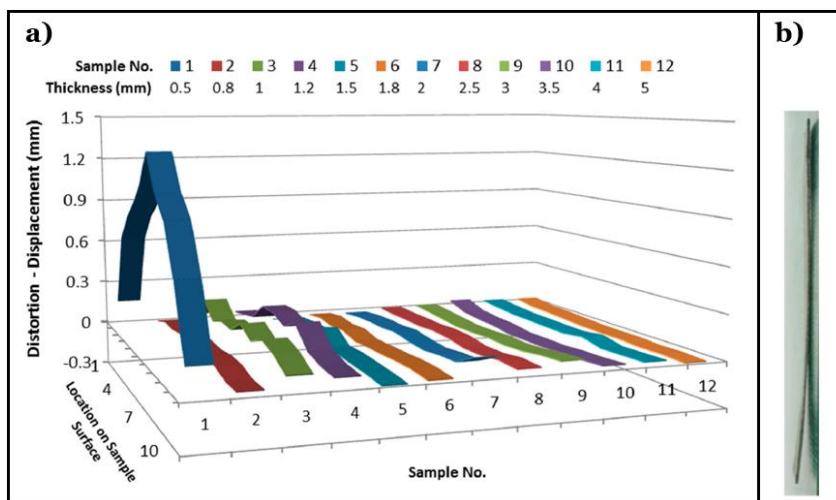


Figure 2-3: (a) Distortion Profile of AlSi10Mg, and (b) Distorted Thin-Wall Sample (Taken from [38]).

2.4 Finite Element Modeling of LPBF

In this section, the details of the finite element method (FEM) to study the LPBF process is discussed. Initially, the fundamental concept of FEM is explored, then the modeling approach for the LPBF process is described.

2.4.1 Introduction to FEM

Finite element modelling (FEM) is an important modeling tool to study the LPBF process. This method solves a model by dividing the 3D geometry into smaller segments called elements. The most common 3D shapes are cuboid shapes that consist of 8 nodes and 6 faces [39]. The fundamentals of finite element analysis are to solve the nodal displacements (X) using the material stiffness (K) and applied nodal forces (R) using an equation Eq. (2-1) [40]. The software uses Gaussian integration points to solve the FEM equations. The FEM software uses the Gaussian integration point, either “full” or “reduced”

integration [41], for the numerical integration approach. For full integration, the number of integration points is sufficient to integrate the virtual work expression exactly, at least for linear material behavior. Reduced integration can be used for quadrilateral and hexahedral elements. In this procedure, the number of integration points is sufficient to integrate exactly the contributions of the strain field [41].

$$[K][X] = [R] \quad (2-1)$$

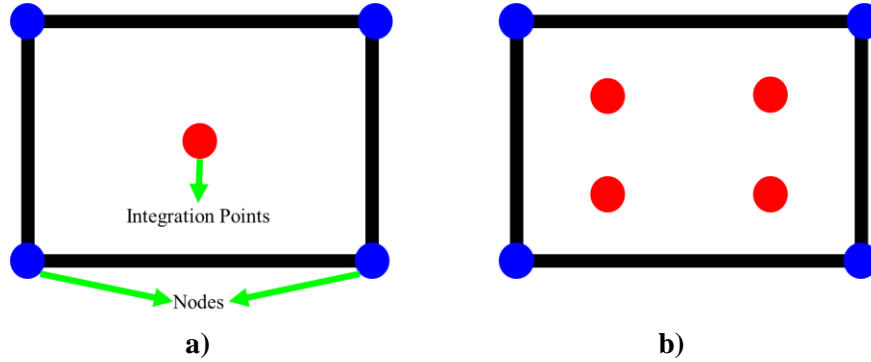


Figure 2-4: Nodes and integration points in elements a) Full integration b) Reduced integration. Yellow points show the position of integration points and green points show the nodes.

2.4.2 Modeling of LPBF Process

2.4.2.1 The couple and decouple models

To simulate the AM process, there are two procedures called the coupled and decoupled methods. An accurate implementation of Newton's method involves a non-symmetrical Jacobian matrix, as illustrated in the following matrix representation of the coupled equations:

$$\begin{bmatrix} K_{XX} & K_{X\theta} \\ K_{\theta X} & K_{\theta\theta} \end{bmatrix} \begin{bmatrix} X \\ \theta \end{bmatrix} = \begin{bmatrix} R_X \\ R_\theta \end{bmatrix} \quad (2-2)$$

The $K_{\theta\theta}$ and K_{XX} matrices represent thermal and mechanical material properties, respectively. The external load and boundary conditions are assumed as R_θ and R_X . The temperature and the nodal displacement are given by θ and X respectively. Solving this system of equations requires the use of the asymmetrical matrix storage and solution scheme. Furthermore, the mechanical and thermal equations must be solved simultaneously. In the coupled model, the mechanical behavior is assumed to affect the thermal behavior of the material.

In the decoupled model, the components in the off-diagonal submatrices ($K_{X\theta}$, $K_{\theta X}$) are small compared to the components in the diagonal submatrices. In other words, the decoupled method assumes that the thermal behavior of the material affects the mechanical but not vice versa. Hence, a costly solution may be obtained by setting the off-diagonal submatrices to zero giving the following set of equations:

$$[\mathbf{K}_{XX}][\mathbf{X}][\mathbf{R}_X] \quad (2-3)$$

$$[\mathbf{K}_{\theta\theta}][\boldsymbol{\theta}][\mathbf{R}_\theta] \quad (2-4)$$

This approximation allows the thermal and mechanical equations to be solved separately, with fewer equations to consider per subproblem. The savings, measured as solver time per iteration, are in the order of two, with similar significant savings in solver storage of the factored stiffness matrix. Furthermore, fully symmetric or approximately symmetric subproblems can be chosen to achieve a solution scheme minimizing systematic storage costs. The solver time savings for the symmetric solution is an additional factor of two [41].

2.4.2.2 Governing Equations

The FEM software solves a set of equations to solve the thermal history of the LPBF process. After the thermal simulation is completed, the quasi-static equilibrium of stress is determined for each time increment. The governing thermal equations solved by FEM software, along with the formulation of the thermal boundary conditions required to solve the temperature field throughout the history of the deposition process, are described below. Then, the governing stress equilibrium equation is explained.

2.4.2.2.1 Heat Transfer Model

FEM software solved the three-dimensional heat conduction in order to obtain the temperature field $T(x, y, z, t)$ through the domain.

$$\rho \cdot C \frac{\partial T}{\partial t} = \frac{\partial}{\partial x} \left(k \frac{\partial T}{\partial x} \right) + \frac{\partial}{\partial y} \left(k \frac{\partial T}{\partial y} \right) + \frac{\partial}{\partial z} \left(k \frac{\partial T}{\partial z} \right) + Q, \quad (2-5)$$

where T represents the temperature, ρ is the density, C is the specific heat, k is heat conductivity, and Q is latent heat [36], [42]. Heat convection and radiation are considered boundary conditions for the model. The Stefan-Boltzmann law calculates the thermal radiation q_{rad} :

$$q_{rad} = \varepsilon \sigma_b (T_s^4 - T_\infty^4), \quad (2-6)$$

where ε is the surface emissivity, σ_b is the Stefan-Boltzmann constant, T_s is the surface temperature of the workpiece, and T_∞ is the ambient temperature. The convection equation for heat loss is:

$$q_{rad} = h(T_s - T_\infty), \quad (2-7)$$

where h is the convective heat transfer coefficient.

2.4.2.2.2 Mechanical Model

FEM has been the most widely used numerical procedure in the field of solid and structural mechanics. The general form of the equation for the mechanical model in LPBF is:

$$\nabla \cdot \sigma = 0, \quad (2-8)$$

where σ is the stress. A constitutive equation is required to relate the stress, strain, and the material properties. The mechanical constitutive law is:

$$\sigma = C \varepsilon_e, \quad (2-9)$$

where C is the fourth order material stiffness tensor and ε_e is elastic strain. Strain for small deformation is:

$$\varepsilon = \varepsilon_e + \varepsilon_p + \varepsilon_T, \quad (2-10)$$

where ε , ε_p , and ε_T are the total strain, plastic strain, and thermal strain, respectively. The thermal strain is:

$$\varepsilon_T = \alpha(T - T^{ref}), \quad (2-11)$$

where α is the thermal expansion coefficient and T^{ref} is reference temperature. The plastic strain is computed by enforcing the von Mises yield criterion and flow rule:

$$f = \sigma_m - \sigma_y(\varepsilon_p, T) \leq 0, \quad (2-12)$$

$$\dot{\varepsilon}_p = \dot{\varepsilon}_q a, \quad (2-13)$$

$$a = \left(\frac{\partial f}{\partial \sigma} \right), \quad (2-14)$$

where f is the yield function, σ_m is Mises stress, σ_y is yield stress, ε_q is the equivalent plastic strain, and a is the flow vector [43].

Chapter 3

Literature Review

This chapter presents the literature review of modeling approaches to simulate the LPBF process. Since modeling of some AM processes such as direct metal deposition (DMD) and DMLS are close to LPBF processes, some of the provided studies are based on different processes. The first section describes LPBF thermal modeling approaches emphasizing the effect of the heat source profile and printing parameters on the thermal history of the part. The second section discusses the modeling approaches used to depict the thermo-mechanical behavior of the part during processing and is divided into two sub-sections. The first sub-section explains how to make an accurate model while the second sub-section describes the approaches to reduce the computational time.

3.1 Thermal Modeling for LPBF Process

Studying the effective parameters in the laser-based printing process is important to analyze the residual stress and strain in the manufactured part. Since the elements in the mechanical model contain the displacement degree of freedom (DoF), the residual stress and strain can be computed [41]. However, the temperature history of the material needs to be established first to study the residual stress of LPBF-printed parts. The thermal modeling of the LPBF process is similar to that of other laser processing techniques such as laser welding [44]–[46] and laser forming [47], [48]. Generally, to study and investigate the temperature evolution in the LPBF process, the finite element method (FEM) is used. Software such as Abaqus, COMSOL, and ANSYS are used for FEM simulations [48]–[50]. The physical phenomenon in a melt pool is mainly controlled by mass and heat transfer, which is highly complicated. The heating and cooling rates are extremely high because of the swift laser irradiation on the powder particles [51]. Also, the melt pool size correlates with the build part microstructures and properties [51]. The remelting of solidified material caused by melt pool geometry may significantly affect part quality such as porosity reduction and minimization of the macro-segregation defect [52]. However, excessive remelting may deteriorate part surface quality [53]. To illustrate the effect of melt pool on temperature history, it is essential to have accurate temperature distribution. Moreover,

studying boundary conditions and the effective parameters on models is necessary to maximize model accuracy.

3.1.1 Models for Heat Input

Many heat profiles with different pros and cons are available and are used to simulate the laser heat source. The models are categorized into two groups: (a) geometrically modified group (GMG), and (b) absorptivity profile group (APG). In GMG, the model size is modified, and the shape of the heat input is mimicked in experimental data, such as Gaussian model [54], Hemispherical [55], Goldak [65C], and conical shape [56]. For example, in J. Ding's research [11], a Goldak model was used and the melt pool size from experiment was considered as reference for model calibration. The APG group has the general form of a 2D Gaussian shape on the surface and a proposed absorptivity function for the depth direction [57]. The laser beam is assumed to be absorbed gradually along with the depth of the powder layer. Therefore, several absorptivity profiles have been proposed, such as the radiation transfer equation [58], linearly decaying equation [59], and exponentially decaying (ED) equation [57], [60].

3.1.1.1 Rosenthal Model

The Rosenthal model is one of the simplest heat input models (presented in 1935) that simulates the heat input as a temperature load [61]. The Rosenthal model became the most popular model for heat input profile since it can predict the material temperature analytically [62]–[65]. Many researches used this model despite its inability to predict the HAZ and temperature gradient precisely [55]. The reason for this limitation is attributed to assuming constant material behavior with changing temperature. In Rosenthal, the heat is applied to the nodes of the part surface and the behavior of the material is constant even with changing temperature [55]. The nodal temperature of the surface is calculated using the following formula [54].

$$T - T_0 = \frac{Q}{2\pi r K} e^{-\frac{v(x+r)}{2\alpha}}, \quad (3-1)$$

where T_0 is the initial temperature of the part, K is the conduction coefficient, α is the penetration coefficient, v is the velocity of heat flux, x is the longitudinal distances to the center of the laser, and r radial distance from the center of the heat source.

3.1.1.2 The Gaussian Heat Input Model

Since the Rosenthal model cannot predict the temperature in the HAZ, the researchers try to use different models to simulate the heat input. Pavelic et al. [55] were the first to suggest a 2D model heat input as a distributed heat profile to predict the temperature in the HAZ. The heat input model is applied as an external load on the surface of the material. The model is also commonly known as Gaussian heat distribution, as shown in Figure 3-1.

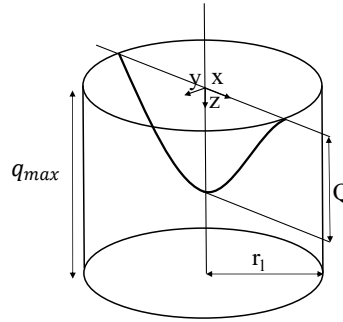


Figure 3-1: a schematic of the Gaussian heat input model

The expression of a 2D Gaussian distribution of the laser beam from [55] is:

$$Q = q_{max} e^{-kr^2}, \quad (3-2)$$

where q_{max} is the maximum heat flux, k is the concentration factor. The term k is related to the heat source width so the more concentrated source would have a smaller diameter and a larger value of k . The maximum heat flux q_{max} can be obtained by integrating the heat flux over the whole area. Therefore, the total thermal heat equals the effective power of heat input Q given in [66] as:

$$Q = \int q(r) dA = \int_0^{\infty} q_{max} e^{-kr^2} \cdot 2\pi r \cdot dr. \quad (3-3)$$

When 85% of the thermal heat is absorbed within the radius of the laser beam and considering Eq. (3-3), then,

$$Q = \frac{2P\eta}{\pi r_l^2} e^{\left(\frac{2(x^2+y^2)}{r_l^2}\right)}, \quad (3-4)$$

where x and y are the distances to the center of the laser, P is the laser power, η is the absorption factor, and r_l is the maximum radius laser spot. When the heat source moves along the scanning track, the

powder ahead of the laser beam continuously melts and solidifies behind the laser beam. In this case, the heat flux is a function of space and time, termed as the Gaussian moving heat input [66].

The semi-spherical input model is a 3D Gaussian model to account for the error due to the temperature distribution in melt pool size and depth. When the heat source is fixed, the distribution of heat flux can be described as:

$$Q = q_{max} e^{\left(-2\frac{x^2+y^2+z^2}{r_l^2}\right)} \quad (3-5)$$

Based on the conservation of energy, it is possible to find the value of q_{max} :

$$Q = \int_0^\infty \int_{-\infty}^\infty \int_{-\infty}^\infty q_{max} dx dy dz. \quad (3-6)$$

After finding q_{max} and replacing in Eq. (3-5) the final expression of the heat input model is:

$$Q = \frac{\sqrt{2^5} P \eta}{\pi \sqrt{\pi} r_l^2} e^{\left(\frac{2(x^2+y^2+z^2)}{r_l^2}\right)}, \quad (3-7)$$

and Figure 3-2 shows the semi-spherical geometry of the heat input model [67].

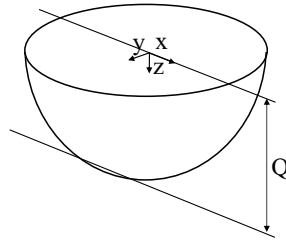


Figure 3-2: A schematic of the semi-spherical heat input model

3.1.1.3 The Goldak Heat Input Model

Based on the Experimental results, the temperature gradient in front of the heat input is steeper than that trailing edge of the molten pool. Thus, the power density of the region in front of the arc center and the region behind the arc center needs to be defined separately [68]. To overcome this limitation,

Goldak proposed a new heat input model that was a combination of two ellipsoids that have different length of heat profile in the rear and front regions [55] (see Figure 3-3). The Goldak equation is defined as:

$$Q_f = \frac{6\sqrt{3}P\eta f_f}{\pi\sqrt{\pi}a_f bc} e^{-3\left(\frac{x^2}{a_f^2} + \frac{y^2}{b^2} + \frac{z^2}{c^2}\right)}, \quad (3-8)$$

$$Q_r = \frac{6\sqrt{3}P\eta f_r}{\pi\sqrt{\pi}a_r bc} e^{-3\left(\frac{x^2}{a_r^2} + \frac{y^2}{b^2} + \frac{z^2}{c^2}\right)}, \quad (3-9)$$

$$f_r + f_f = 2, \quad (3-10)$$

$$\frac{f_r}{a_r} = \frac{f_f}{a_f}, \quad (3-11)$$

where a , b , and c define the size of the melt pool profile, as shown in Figure 3-3. The factors f_f and f_r are used to divide the laser power into two regions which can be acquired by the size of the melt pool. In Eq. (3-8) and Eq. (3-9), Q_r and Q_f are the heat distribution parameters for rear and front regions, respectively. The proposed model was compared with the Krutz FEM model and experimental results in [69]. A model of a single track in a welding process was created and the predicted nodal temperature results were compared with experimental findings. The evaluation showed that the double ellipsoid model matched the experimental results more closely than the Kurtz model (single ellipsoid model). The predicted temperature from the Goldak heat input had around 10% error in the HAZ and reached less than 5% in the distant regions.

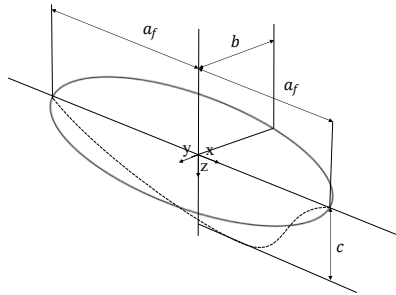


Figure 3-3: A schematic of Goldak heat input model

3.1.1.4 Exponentially Decaying (ED) Heat Input Model

It is possible to modify the heat penetration in the powder by changing the shape of the heat input from two-dimensional to three-dimensional geometries. In a study developed by Zhidong Zhang et. al. [57], 8 different types of heat inputs were studied, including APG, Goldak, and Gaussian heat profiles [57]. The models were compared to the size of the melt pool in the experiment. To measure the size of the melt pool, single tracks with different parameters were printed on a layer of powder. Then, the tracks were sectioned and prepared using metallographic techniques, after etching, the size of melt pools was measured by optical microscopy. The melted zone is shown with a brighter color compared to the substrate. As shown in Figure 3-4, all the heat input models could predict the melt pool width with higher accuracy compared to the melt pool depth. The Goldak and ED heat input models had minimum error in predicting the melt pool. However, since the Goldak coefficients could take a number of iterations, the ED heat input model was used for the study. For APG, a factor was added to the heat distribution equation to define the absorption through the depth of the powder [57]. The ED heat input model is a combination of Gaussian and absorptivity factor to model the heat absorption within the powder [44], [70].

$$Q = \frac{2P}{\pi r_l^2} e^{\left(-2\frac{x^2+y^2}{r_l^2}\right)} \eta \frac{1}{H} e^{\left[\left(-\frac{|z|}{H}\right)\right]}. \quad (3-12)$$

All variables are similar to the Gaussian model and the only difference in this model is the H parameter used to show the heat penetration through the powder.

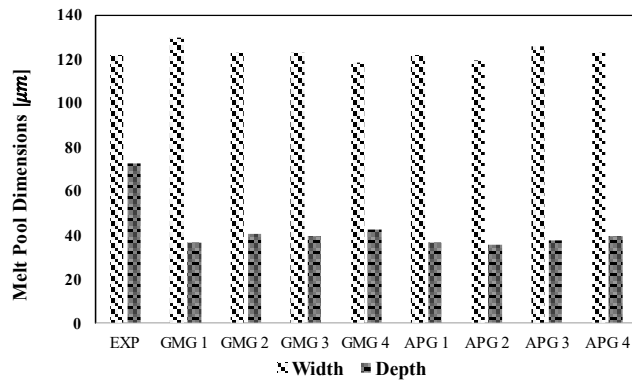


Figure 3-4: Comparisons of the heat input models based on the melt pool dimensions [57].

3.1.2 A Few Examples of Effective Parameters in Thermal Model

During the LPBF process, heat losses may occur due to thermal radiation, free convection, forced convection, or conduction through the surrounding powder [43]. For small builds, e.g., single line experimental depositions, a common modeling practice is to ignore heat losses altogether. This is a fair assumption, as most of the incident heat will be absorbed by the substrate. However, the effect of heat losses for thermal part-scale models has important influence in predicting results. Also, longer build times are more likely to heat the substrate which may necessitate fixturing loss considerations. There is also a modeling consideration that motivates the need for more accurate boundary loss estimations (the perpetuation of errors), which scale with volume or time. Commonly, thermal boundary losses are lumped together into a single effective heat transfer coefficient [43].

$$h = h_{free} + h_{forced} + h_{rad}, \quad (3-13)$$

where h_{free} , h_{forced} , and h_{rad} are the heat transfer coefficients of free convection, forced convection, and linearized radiation, respectively [43]. Radiation is a major part of heat loss at high temperatures because it is a 4th-order function of temperature (Eq. (2-6)). It is a nonlinear term which highly increases the computational expenses. Based on experimental data, an empirical formula combining convective and radiative heat transfer was given by Vinokurov as [71]:

$$h = 2.41 \times 10^{-3} \varepsilon T^{1.61}, \quad (3-14)$$

where h is the lumped heat transfer coefficient, T is the material temperature in Kelvins, and ε is the emissivity factor. The heat convection is used as a function of emissivity and temperature; therefore, the FILM subroutine must be used to implement the effect of temperature on the convection coefficient. The associated loss in accuracy using this relationship is estimated to be less than 5% [71]. This consideration is a common approach to combine radiative and convective heat losses in order to decrease the computational time [42], [72], [73].

Cheng et al. [53] studied the effect of hatch printing patterns on the melt pool size in the LPBF process for IN-718 superalloy (see Figure 3-5 (a)). The size of the melt pool was reported to be smaller at the beginning of the printing process and continuously grows until it reaches a stable dimension. Knowing the required distance to reach the stable melt pool dimension is important to print a uniform track. It was found that the laser power and speed affect the required length for the melt pool to stabilize. Larger

beam power and slower laser speed require a longer travelling distance for a melt pool to reach a stabilized melt pool dimension, while a smaller beam diameter may reduce this distance. The size of the patch depends on the laser speed, power, and diameter (Figure 3-5 (a)). In this study, the DFLUX and UMATHT subroutine codes are used to implement the heat flux and define the material state. Cheng et al. explained finer mesh size requires for the region which laser is interacting to keep the model accuracy [53] (Figure 3-5 (b)). However, the model still requires a large number of elements because of the used mesh algorithm.

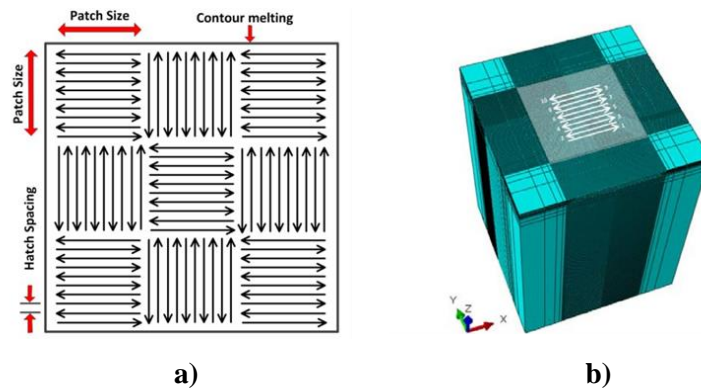


Figure 3-5: a) The schematic of island printing pattern. b) The meshing technique used to reduce the computational time [53]

3.2 Thermo-Mechanical Modeling for LPBF Process

Thermo-mechanical models are used to analyze the distortion and residual stress in a part. As explained in section 2.4.2.1, the model requires the thermal model results first, thus it will take longer to solve. Consequently, the computational time and the accuracy of the predicted results are the main challenges for this model. The assumptions made to simplify the mechanical model plays an important role in the computational time efficiency [43]. Here, a brief description of assumptions made in mechanical models is provided.

3.2.1 Approaches to Improve the Accuracy of Models

Based on the literature, there are several parameters involved in the LPBF process. Considering these parameters in a simulation has a significant impact on the accuracy of mechanical or thermo-mechanical models [43]. Many thermo-mechanical assumptions, such as fluid flow inside the melt pool and powder

shrinkage, are applicable to enhance the precision of the predicted results. In this section, studies on some of the assumptions are presented.

3.2.1.1 Powder Shrinkage

Powder shrinkage in the AM process is relatively large and the solidified layer thickness is not the same as the amount of powder added to the bed. In the study performed by M. Galati et al. [74], the powder shrinkage during manufacturing was studied. A new analytical approach was developed to emulate the volume variation of the powder bed during heating and melting. Particularly, the expansion of the powder particles and the porosity reduction within the powder bed were simultaneously considered. The thermal expansion and the shrinkage of solid material during heating and cooling and the stress formation within the solid material were also modelled. The model predicts the geometrical transformation of the powder into solid material in an efficient way. The material shrinkage Eq. (3-15) contains two factors, where the first one represents the increase of the volume due to the thermal expansion of the powder particles during the heating. The second factor describes the volume lost due to the reduction of the distance between the powder particles and the melting of the powder, which in turn decreases the porosity of the powder bed [74].

$$\delta V = (1 - \phi(T))V\alpha_{BULK}\delta T - \phi(T)V, \quad (3-15)$$

where V is the volume where the powder is contained, T defines the variable temperature, $\phi(T)$ is the temperature-dependent porosity, and α_{BULK} is the thermal volumetric temperature expansion coefficient of the bulk material. After comparing the results with experimental data, 15% error was observed between the measured melted areas. However, the coupled model needed about 45 times longer to processing time, indicating that it is not applicable for the part-scale model [74].

3.2.1.2 Melt pool geometry

Many researchers tried to minimize the residual stress in manufactured parts by modifying the size and maximum temperature of the melt pool, which requires fluid flow modelling in the liquid region. Mukherjee et al. [24] combined a well-tested three-dimensional transient heat transfer and fluid flow model of additive manufacturing with a thermo-mechanical model to accurately calculate the temperature fields, residual stresses, and distortion. Convective flow of the molten metal within the

melt pool is driven by the surface tension gradient on the top surface of the pool resulting from the spatial variation of temperature (Figure 3-6) [75], [76].

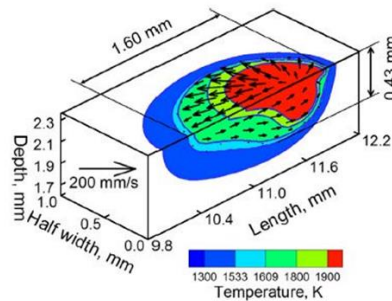


Figure 3-6: An example of predicted melt pool in simulation [24].

To link the thermal model with the mechanical model, a UTEMP subroutine code was used. This code transfers thermal data to the mechanical model and controls the temperature. Based on the results, Mukherjee et al. [24] found that the substrate acts as a heat sink. Hence, the maximum temperature increases along the build direction because the upper layers are further away from the substrate. The strain is directly related to the maximum temperature, but increasing the temperature decreases the residual strain. The calculated temperature and residual stress distributions were tested using independent experimental results. The comparison between the experimental results and mechanical model showed that the predicted results were close to the measured residual stress in the part [24] (Figure 3-7).

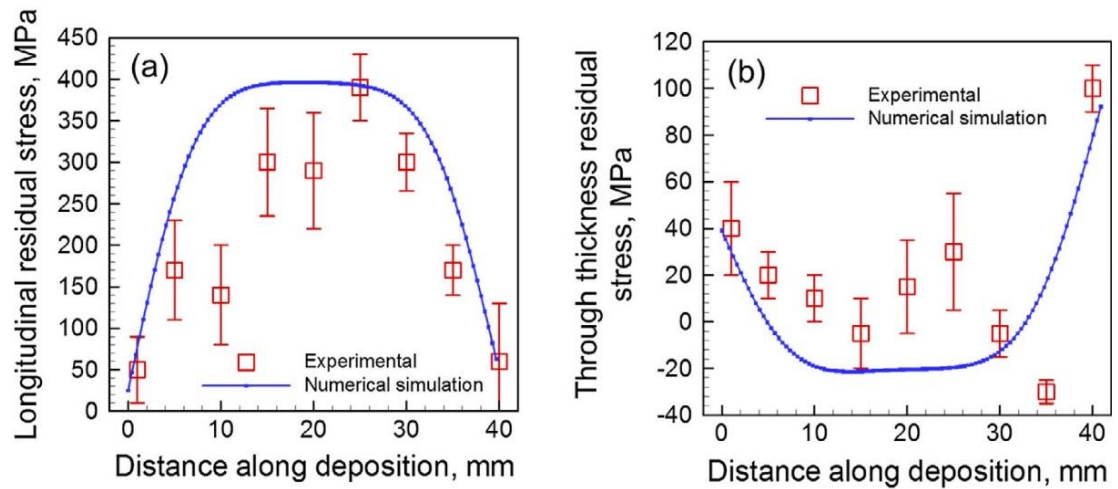


Figure 3-7: Comparison of experimentally measured [77] and numerically computed (a) longitudinal residual stress and (b) through-thickness residual stress during the laser deposition [24].

Several researchers have focused on improving thermal model accuracy to enhance the prediction of residual stress and strain in the mechanical model. Roberts et al. [67] validated a thermal model of the LPBF deposition of 0.15 mm^3 of titanium powder. Li et al. [78] developed and validated a temperature-dependent microstructural model for single-layer 2 mm^2 titanium builds. The thermal model developed in reference [79] was used to simulate the deposition of a 1 mm^3 volume of nickel. The noted LPBF thermal models provide insight into the thermal cycles experienced during the manufacturing process, showing the importance of the thermal model to accurately predict the mechanical results. However, it would be infeasible to simulate larger deposition volumes as the problems would become too computationally expensive [44].

3.2.1.3 Element size

The element size is important for model accuracy and computational time and performing a mesh sensitivity study is especially important for larger parts. However, knowing the appropriate element size is not enough for AM modeling since the zone close to the melt pool needs finer elements [80]. Consequently, the meshing should be dynamic, and the element size should be increased for layers far from the (heat affected zone) HAZ. Shiyan et al. [80] presented a new FE framework to update discretized geometries at regular intervals during the simulation process, allowing greater flexibility to

control the degree of mesh coarsening. The adaptive mesh coarsening technique during the analysis of the already deposited layers is not supported in the ABAQUS software package. The ABAQUS software also includes a useful tool, called solution mapping, only applicable for manual mesh refinement when the present mesh is incapable of handling high distortions. However, the solution mapping technique cannot be applied to the AM process simulations due to the continuous addition of material to the built part [81]. Therefore, a modeling framework in the Python script was developed to implement the proposed adaptive mesh coarsening in the AM processes [82]. The proposed framework helps to stabilize the number of DoFs, which reduces the computational time. It is shown that mesh coarsening reduces the DoF 15 times more than the conventional method (Figure 3-8). As shown in Figure 3-8, the number of DoFs are kept constant (after the 20th layer), which generates the same computational time to calculate the model for the upper layers. The new framework was evaluated by simulating direct metal deposition (DMD) of a thin-walled rectangular and a thin-walled cylindrical part, and comparing the computational speed and predicted results [80].

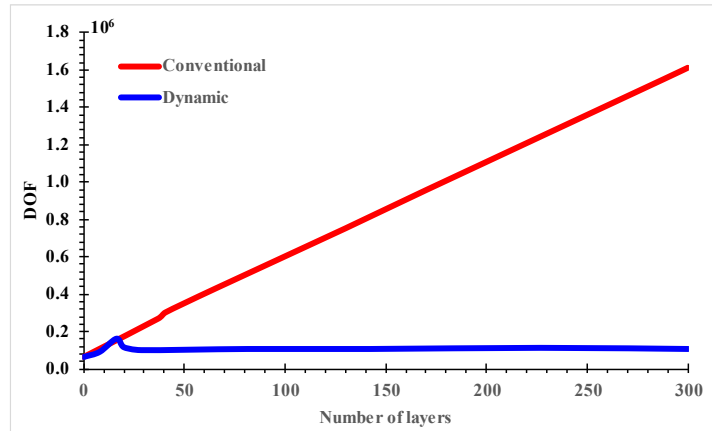


Figure 3-8: Required number of elements with and without mesh-to-mesh solution mapping

3.2.2 Approaches to Improve Computational Efficiency

Increasing the model accuracy to predict the residual stress close to experimental results, without the proposed assumption in the previous section, requires long computational time. As a result, few assumptions are necessary to decrease the computational time. In this section, a few common approaches are presented and explained how they might affect the model accuracy.

3.2.2.1 The Modified Heat Input Model

The laser spot size in the LPBF process is much smaller compared to other AM processes [19]. The laser radii are as small as 0.025 mm [83], 0.015 mm (laser micro sintering) [84], or even 0.010 mm [85], but typical values lie in the range of 0.05–0.25 mm [24], [42], [54], [74], [80]. Using smaller radii allows having finer resolution at the edges but takes more time and makes the modelling process difficult. A typical model might need over 100,000 elements and 1,000,000 time steps. To overcome this restriction, Irwin et al. [19] presented a new heat distribution using larger time steps. This model allows the simulation of an entire heat input scan in just one-time increment. Eq. (3-16) is averaged throughout the time increment:

$$\bar{Q} = \frac{1}{\Delta t} \int_{t_0}^{t_0+\Delta t} Q dt, \quad (3-16)$$

where t_0 is the time at the beginning of the increment. This time-average \bar{Q} of the Goldak's power distribution is referred to as the line input (LI). By substituting The Goldak equation into Eq. (3-16) and evaluating the integral, LI can be expressed as:

$$\bar{Q} = \frac{3P\eta}{\Delta t v_s \pi a b} e^{-3\left(\frac{x^2}{a^2} + \frac{y^2}{b^2}\right)} \operatorname{erf}\left(\frac{\sqrt{3}(z + v_s t)}{c}\right) \Big|_{t=t_0}^{t_0 + \Delta t}, \quad (3-17)$$

where erf is an error function. This formulation allows time increments to be made arbitrarily large, without skipping any elements as done in Goldak's model. However, large time steps can lead to inaccurate results. Instead, the scan is broken up into several linear segments, where each segment is applied in one time step. Based on the results shown in Figure 3-9, if the length of the heat input is 5.77 times larger than the regular heat input profile, the model will have the least error, which suggests that the computational time can be around 5.77 times smaller [19]. However, the presented results are based on a specific material and could change depending on material and manufacturing parameters such as speed and laser power.

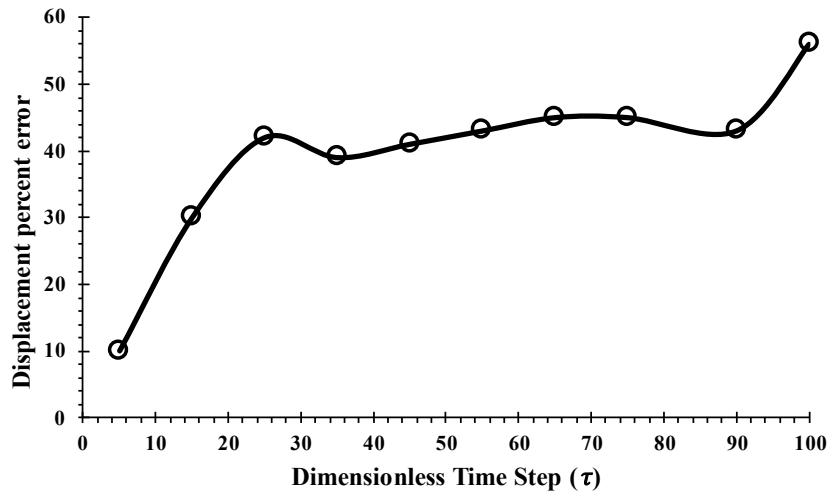


Figure 3-9: The accuracy of predicted displacement verses the time step size

3.2.2.2 Modified Models to Predict the Residual Stress

There are four fundamental approaches to the indirect modelling of LPBF distortion: lumped laser passes, flash heating, inherent strain, and multi-scale simulation. The details of each method and their potential limitations are given below.

1- Lumped Model:

Lumped models are the simplest indirect modelling method, whereby the simulation approximates the deposition of several individual layers into a single larger layer. Hodge et al. [18] showed that the deposition of 20 whole layers can be simulated by combining them in a process called agglomeration. The model is applied to 3 geometries, a horizontal prism, a vertical prism, and an L-shaped build. Comparison of simulation results with measurements of distortion and stress show good agreement. However, the code must be run on a cluster of 128-512 CPUs and the largest part simulated is relatively small – an equilateral trapezoidal prism with a length of 60 mm, a thickness of 10 mm, whose bases are 50 mm and 5 mm long.

2- Inherent Strain:

These models operate under the assumption of the uniformity of plastic strain developed during manufacturing [86]. Inherent strain models decompose the problem into 2 fundamental stages: plastic

strain calculation and plastic strain application [87]. Strains are typically calculated from a small moving heat input model [88] or measured from small experimental builds [89]. As the inherent strain method is founded upon the application of a uniform strain field, any non-homogeneity of distortion due to geometric differences is neglected [90]. The elastic part-scale models for these simulations can still take significant time, driven by the nodal density of uniform voxel meshes typically used in these codes, but the researchers in this area have been able to simulate significantly larger geometries than the direct method, with the largest reported inherent strain model size being $45.6 \text{ mm} \times 2.7 \text{ mm} \times 4.75 \text{ mm}$. However, a recreation of the small-scale method from Keller and Ploshkin [88] and the experimental strain measurement strategy (more common in commercial codes [89] by Bugatti and Semeraro) indicate significant limitations [90].

3- Flash Heating:

For the flash heating method, one or multiple layers are activated at an elevated temperature to approximate the heating process. C. Zaeh et al. [91] implemented this method to model the powder bed construction of a small cantilever. The authors reported good model- prediction agreement with neutron diffraction residual stress measurements showing just 13% maximum stress error. However, the model's peak deformations were off by an order of magnitude from the values reported in their experiments [92].

4- Multiscale Modeling:

Few publications describe a functioning multi-scale model in detail [93], [94]. Liang et al. [95] extracted normal strains from the thermo-mechanical modeling of two stacked DED laser passes, followed by the simulation of a multilayer rectangular structure construction. For a 10-layer deposition, the computational time for the part-scale simulation was reduced by over 98%, while incurring less than 10% error, compared to the moving heat input model. The authors admitted that their work was limited to the deposition of single bead walls, yet the speed and accuracy of the multi-scale process were shown [95]. Li et al. detailed a multi-scale model consisting of 3 stages to simulate the LPBF process [7]. First, a moving heat input is used to predict the nodal temperature within a HAZ. Next, a mesoscale thermo-mechanical analysis is performed and the integrated heat input from the first model is applied to a slightly larger deposition volume to calculate a residual stress tensor. Finally, mechanical

simulation of a part-scale geometry, $35 \text{ mm} \times 15 \text{ mm} \times 0.15 \text{ mm}$, is completed by mapping the residual stress tensor from the meso-scale model [95].

3.3 Knowledge Gap

An analysis of literature on the multi-scale AM simulation for nickel-based superalloys identified the following knowledge gaps:

1. The available line heat input model is based on the Goldak model, not yet developed for the LPBF process. The Goldak heat input model was proposed in 1984 for slow-moving heat sources and high energy density applications (such as welding), whereas the heat source in the LPBF process is 100 times faster and requires 10 times less power. As part of the Goldak equation, it is necessary to measure the experimental melt pool length, which is hard to accomplish for LPBF. Therefore, it is necessary to develop a new line heat input model based on a heat input that is a better representation of the heat source in LPBF. The ED heat input model would be an ideal candidate for this application. However, for high gamma prime superalloys, the mechanical and thermal properties vary dramatically and there are no comparable calibrated line/beam-scale models. Thus, it is essential to measure properties for a wide range of temperatures (from room temperature to $1400 \text{ }^\circ\text{C}$).
2. The literature on printing patterns contains very few parametric studies with simulations. Most parametric evaluation models utilize flash heating (layer heating) in order to overcome the large processing time problem. Since large heat input models combine all laser tracks into one single source of heat, they cannot capture the stress directionality. Therefore, LPBF parametric simulations are mostly limited to laser speeds and powers, and parametric studies for printing patterns are limited to experimental studies. To optimize printing pattern strategies for different part geometries, it is necessary to develop an efficient numerical model to capture stress directionality.
3. The limiting build height (LBH) phenomenon poses a significant challenge and reduces design flexibility for LPBF part construction. The laser scanning strategy presents an interesting alternative to mitigate the LBH phenomenon during thin-wall part construction. Currently, continuous rotation at 67° is widely regarded as the best strategy for processing LPBF

components. However, the effect of the optimal scan strategy on thin-wall part fabrication has not been investigated. Research on the LBH of thin-wall parts is very limited and failure mechanisms are still unknown. To better understand the effect of laser parameters on LBH, large experimental DOEs are necessary, which are expensive and time-consuming. While FEA is ideal for parametric evaluations, there are no simulation techniques available to capture stress directionality on a part-scale component within a feasible processing timeframe. This problem is more significant for thin-wall part simulation which requires capturing part failures and achieving high resolution results within the laser track direction.

Chapter 4

Research Overview

4.1 Goal and Objectives

The Canadian manufacturing sector faces intense global competition. To remain competitive, manufacturers must develop and implement new AM technologies and materials within Canadian aerospace manufacturing plants. Competitive technological advantage can be established by strengthening the Canadian aerospace sector and deterring manufacturing plants from migrating to lower-cost regions of the world. The purpose of this study is to develop a multiscale model that can simulate the LPBF process for large components while preserving the stress directionality created by the printing pattern. The framework requires minimum input to facilitate DOE development and parametric evaluation. This helps to study the impact of printing parameters such as printing pattern and part geometry on created residual stress and component construction. Therefore, it is possible to reduce the total number of trial and error iterations and manufacturing costs. In addition, the focus of this study is on superalloys with high gamma prime superalloys as they have unique behavior at the elevated temperature as well as lack of study on this material.

4.2 Research Strategy

To address the aforementioned knowledge gaps, the research is broken down into three key areas to explain how the new models were developed and how they were used to better understand the effect of printing patterns and other laser parameters on LPBF part integrity. The code is developed specifically for high gamma-prime Ni-based superalloys RENÉ 108 and RENÉ 65.

4.2.1 Developing a New Line Heat Input Model: Part 1-Thermal Model and Part 2-Mechanical Model (Knowledge Gaps 1&2)

This study aims to develop a new line heat input model for LPBF processes. The new HL heat input model is time-integrated over the ED beam-scale heat input. The HL model is calibrated for nickel-based superalloys based on temperature-dependent material properties provided by industrial partners. Experimental melt pool measurements are used to calibrate the model. According to previous studies,

this method is well accepted by the community as it has demonstrated its effectiveness and accuracy. As part of the first DOE, there are 90 single tracks with six different laser speeds and three different laser powers. Model coefficients are selected to minimize error between the simulated and measured melt pools. The HL model is then compared with the ED heat input model in terms of its ability to capture stress directionality. In the second DOE, twelve components are printed with different laser power and printing patterns, and residual stress is measured using XRD. The HL model is then validated using the experimental results.

The HL model coupled with the mesh coarsening technique is used for a parametric study. The laser power and printing pattern parameters are evaluated independently. A total of 3 laser powers and 4 printing patterns are considered for this evaluation. This study indicates how the printing pattern affects the compressive stress along the build direction and the tensile stress along the longitudinal direction. These stresses are believed to play important roles in micro-cracking and LBH of high gamma prime superalloy.

4.2.2 Parametric Study on Interdependent Influences of the Laser Power and Printing Pattern on Residual Stress (Knowledge Gaps 2)

This study fills the gap between the developed model in the previous chapter and the next chapter. The developed model is beneficial for the parametric study, especially for the printing pattern as it captures the stress directionality at high resolutions. Unlike the previous chapter, which evaluates the direct impact of printing parameters, this chapter focuses on the interdependent influence of creating residual stress through simulation. Moreover, the computational efficiency of mesh coarsening technique is explained in detail. Using the developed model from the previous chapter, two different laser powers of 180 W and 200 W are considered, as well as two different printing patterns with vector angles of 0° and 90° . Von Mises stress is a result of stress in different directions, hence considered for this evaluation. The required time for this study is divided into two sections and studied separately. Lastly, this chapter illustrates how printing parameters are interrelated and highlights the need to improve simulation efficiency for larger components presented in the following chapter.

4.2.3 Developing Lumped HL Model to Simulate the Laser Powder Bed Fusion Process for Large Scale Components (Knowledge Gaps 2&3)

This chapter evaluates the effect of printing strategy on minimizing the LBH phenomena in high gamma prime LPBF thin-wall parts. Thirty-four RENÉ 108 thin-wall parts with five different part lengths and eight printing patterns were investigated in the experiment. The experimental findings are linked to in-process stresses (predicted using numerical modelling methods) to gain comprehensive understanding of the LBH mechanism. Based on the presented findings, scan strategies to minimize in-process compressive stresses and mitigate LBH are proposed.

A lump hybrid line heat input model is developed by combining the layer lumping and laser track integration approaches. This allows improved computational efficiency and stress compilation along the laser track. A 3D scanner is used to measure the distortion of the component and validate the accuracy of the newly developed model. The presented model is used to evaluate the effect of printing pattern on part distortion and better explain the LBH mechanism.

4.3 Research Map

This research map illustrates how the research strategies (Section 4.1), the goal, and the objectives (Chapter 1) are related.

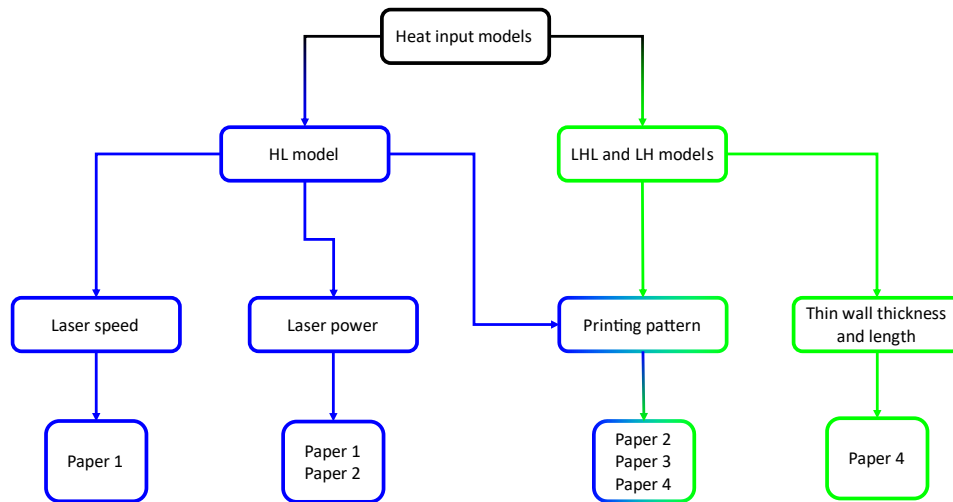


Figure 4-1: An interactive map showing correlations between paper-based research strategies.

Chapter 5

Developing a New Line Heat Input Model: Part 1-Thermal Model

In this chapter, a new line heat input model is proposed to enhance the computational efficiency as well as maintaining the results accuracy. A DOE of laser speed and power was used to create the experimental results for evaluating the models. The melt pool size from experiment was used to validate the results for a conventional beam scale model. The model was used as a reference to calibrate the track scale heat input model. The line heat input model heat input model enhances the computational time over 300 times. The predicted melt pool by the new mode was evaluated with experiment and beam scale model. To compare the new developed heat input model with conventional beam scale models the cooling rate, nodal temperature, and temperature distribution of a printed track for both models were compared.¹

The chapter presents an accepted manuscript of an article published in the Journal of Frontiers in Materials.

Frontiers in Materials. 2021 Nov 8:477 Doi: 10.3389/fmats.2021.759669

5.1 Introduction

Laser powder bed fusion (LPBF) is an additive manufacturing (AM) process where a laser is used to locally consolidate powder into a desired geometry. Development of LPBF parts generally requires expensive trial-and-error experiments to determine an ideal set of laser parameters. A finite element (FE) model could be used to determine a set of laser parameters to reduce the number of defects and experimental iterations required to produce a functional AM part [20], [96]. Modeling requires knowledge of the material's thermo-mechanical behavior at different length scales. For LPBF processes, the laser spot size ranges from 50 to 250 μm [19], [84], [85], while the final parts can achieve sizes in the centimeter scale. Consequently, to simulate full-scale AM parts, FE models must have large model sizes and high computational costs [97]. There are limited publications describing a functional multi-scale model in detail and even fewer papers predicting the temperature field in a part-scale model [92]–[95]. To simulate the thermal history and melt pool geometry, it is essential to accurately model the laser heat source. Depending on the length scale of the simulation, there are different types of heat input models such as beam-scale, track-scale, and layer-scale heat input models [92]. One common approach to model laser melting at the part scale (macroscopic) is the lumped laser model where the heat source is distributed over multiple build layers. Several publications have applied a lumped heat source approach to LPBF simulation [18], [97], [98]. This can accurately predict the part distortion and residual stresses but lacks resolution for thermal history at micro- and macroscopic scale. Beam-scale heat input models are capable of predicting the melt pool geometries, temperature distributions, and phase transitions within LPBF-printed parts as demonstrated in [24], [99]. However, to solve a typical transient beam-scale model, finite elements and time increments must be in the range of 100,000 and over 1,000,000, respectively, resulting in long computational times rendering it impractical at the part scale [19]. To successfully model the effect of the laser beam at multiple scales, a model accounting for the effect of the laser beam at a larger scale must be developed. One conventional approach to decrease the computational time at the laser-beam scale (microscopic) is to average the heat input over its path and simulate an entire track length in one increment. This is possible due to the high laser scan speed of the LPBF process. Luo and Zhao consider a simple Gaussian 2D track-scale heat source for a thermal model, which decreases the computational time by 70% [66]. However, a 3D heat input is required to accurately simulate the heat penetration within the powder [58] and the heat distribution

under the laser beam is far from a simple circular shape. Irwin and Michaleris propose a 3D heat source model to reduce the computational time by a factor of 100 with 10% error in predicted distortion [19]. The model developed by Irwin and Michaleris [19] simulates the entire Goldak et al. heat input [55] as a single heat input calculation. The semiellipsoidal power distribution proposed by Goldak et al. [55] was originally developed for welding processes. Recently, Liu et al. [100] developed a new equation to describe the LPBF heat source more accurately. It follows a Gaussian profile on the Cartesian coordinate system, and an exponentially decaying profile along the z- direction. Zhang et al. [57] showed that the exponentially decaying (ED) heat source model replicates the rapidly-moving LPBF laser heat source better than the model developed by Goldak et al. Besides the laser heat source, the effect of the powder on heat absorption and cooling of the consolidated material must be considered during modelling of LPBF processing. The Irwin and Michaleris model neglects the effects of the powder state on the heat transfer boundary conditions[19]. The powder properties have a significant effect on the LPBF thermo-mechanical performance, which has been described in [16]. Sih and Barlow [101] showed thermal conductivity of the powder is significantly lower than the solid state of the material, which influences the heat distribution and residual stress. In this series, a new track-scale model is proposed to account for the thermo-mechanical behavior at the microscopic scale. A new Hybrid Line (HL) heat input model is derived from the 3D ED heat input model from [60]. The model accounts for the material state transition from powder to solid. It is calibrated for high gamma prime nickel-based (Ni-based) superalloys by incorporating thermo-mechanical properties of the powder and fully dense material. The first part of this work focuses on simulating the thermal behavior of LPBF. The HL model is evaluated by comparing the processing time and thermal behavior to experimental results and single-track simulation using beam scale ED model. Predicted melt pool geometries, nodal temperatures, cooling rates and temperature distributions are evaluated.

5.2 Material and Experimental Method

5.2.1 Material Composition

Two In this study, a gas-atomized high- γ' Ni-based superalloy RENÉ 65 (R65) powder, produced by ATI Powder Metals, is used. Ni based superalloys are commonly used for high-temperature applications such as turbine blades and compressor vanes in aircraft gas turbine engines [102]–[104].

The powder particles were mostly spherical with a size distribution of 12–42 μm . The R65 chemical composition is 15% Cr, 13% Co., 4% W, 4% Mo, 3.5% Ti, 2.1% Al, 0.9% Fe, 0.7% Nb, 0.05% Zr, 0.04% Ta, 0.01% B and the balance is Ni.

5.2.2 LPBF Experimental Procedure

To validate the HL model, a single-track LPBF design of experiments (DOE) was completed. The DOE print was conducted on an Aconity MIDI LPBF machine under atmospheric pressure conditions. A 120 mm \times 85 mm \times 2mm substrate was printed on a non-pre-heated circular steel base plate using the as-received R65 powder. The as-built substrate was extracted and polished to minimize the surface roughness before printing a series of single tracks. A total of 90 single tracks were printed using 18 different process parameter combinations in a 40- μm thick powder layer on the polished substrate. Each set of parameters was repeated five times to achieve statistically consistent results. The process parameters investigated in this DOE included laser power and laser speed. The laser speed was varied from 800 to 1,300 mm/s in increments of 100 mm/s, and the laser power was varied from 180 to 220W in increments of 20 W. The single-track DOE is shown in Figure 5-1 (a). A laser beam radius of 60 μm was maintained for the printing process.

5.2.3 Melt Pool Characterization

The printed single-track experiments were cross-sectioned perpendicular to the laser-path. Each block was mounted, ground and polished using standard metallographic techniques, then etched for 30 s with Glyceregia (15 ml HCl, 10 ml Glycerol, 5 ml HNO₃). Optical microscopy using a Keyence VK-X250 confocal laser microscope was completed to measure the melt pool width and depth of the printed tracks. Figure 5-1 (b) shows an example of the melt pool dimensions obtained using this approach. The penetration into the substrate is considered the depth, and the distance between two edges of the melted zone is considered the width of the melt pool.

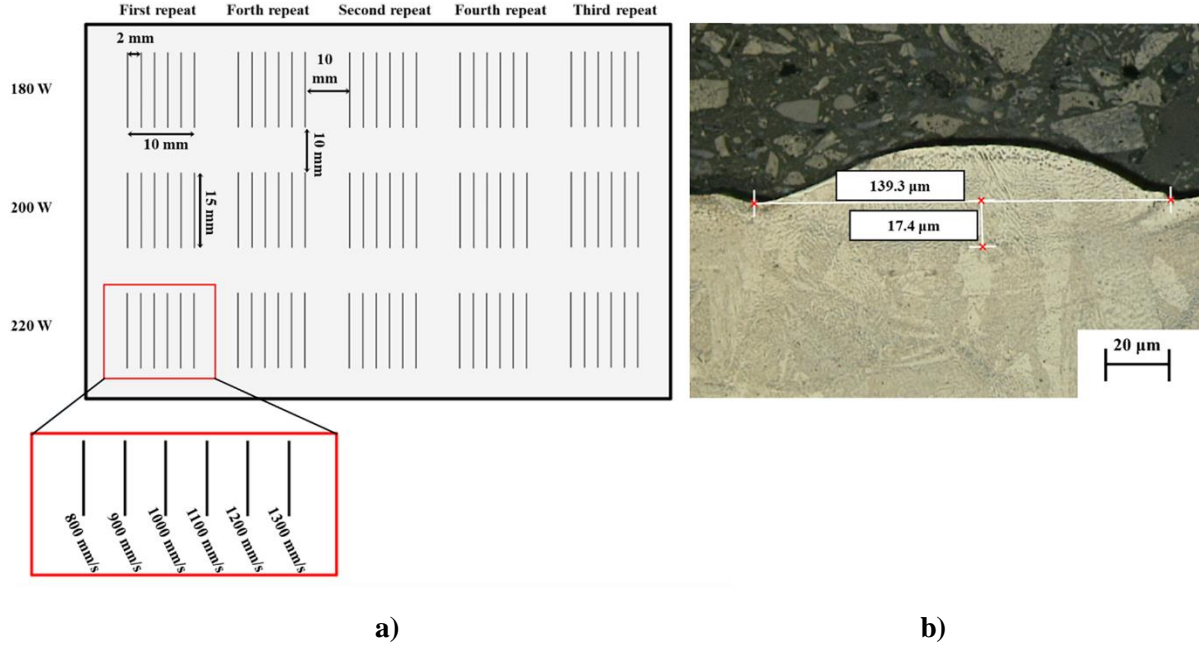


Figure 5-1: a) Single track DOE parameters and configuration on the powder bed substrate. b) Optical microscope image showing R65 single track melt pool produced by LPBF with a laser speed of 800 mm/s and power of 200 W.

5.3 Modelling of the Laser Heat Source

Accurate simulation of the LPBF process requires a thermal model capable of reproducing the laser heat input together with the dynamic phase transition between the solidified part and the powder bed. This section first describes the well established beam-scale ED model used as a reference. Secondly, the new track-scale 3D heat source model developed for LPBF is described. Finally, the heat dissipation and FE implementation methodology are provided.

5.3.1 Beam Scale Exponentially Decaying Heat Input Model

In the ED model, the heat input energy from the laser is represented as a Gaussian distribution heat source on the surface and absorbed exponentially through the powder depth. The energy input (Q) of the ED model is given by:

$$Q = \underbrace{\frac{2P}{\pi r_l^2} e^{\left(-2\frac{x^2+y^2}{r_l^2}\right)}}_{q_0} \frac{\eta}{H} e^{\left[\left(-\frac{|z|}{H}\right)\right]} \quad (5-1)$$

where Q is the input energy, η is the absorption coefficient, and P is the laser power. The parameters x , y , and z represent the orientations of the local coordinates, r_l is the radius of the laser, and q_0 is the value of a 2D Gaussian heat input profile. The energy penetration depth within the powder is computed using the coefficient H , equal to the powder layer thickness, as done in [60].

5.3.2 Track Scale Hybrid Line Heat Input Model

For the HL model, the energy from the ED heat input model given in Eq. (5-1) is integrated over a time increment using Eq. (5-2):

$$\bar{Q} = \frac{1}{\Delta t} \int_{t_0}^{t_0+\Delta t} Q dt \quad (5-2)$$

where Δt is the time increment, t_0 is the time at the beginning of the increment and \bar{Q} is the time-average of the beam-scale heat input model. By substituting Eq. (5-1) into Eq. (5-2), the moving HL heat input model in the x direction corresponding to the laser scanning direction becomes:

$$\bar{Q} = C \frac{P\eta}{\sqrt{2\pi}\Delta t v_s H r_l} e^{\left(-\frac{|z|}{H} - 2\left(\frac{y}{r_l}\right)^2\right)} \left(\operatorname{erf}\left(\frac{\sqrt{2}(x_{end} - x)}{r_l}\right) - \operatorname{erf}\left(\frac{\sqrt{2}(x_{start} - x)}{r_l}\right) \right) \quad (5-3)$$

The function erf is the error function while x_{start} and x_{end} are the spatial start and endpoints of the heat input model. These two variables are defined by the laser speed (v_s) and time increment (Δt). The parameter η is the absorption factor obtained from [105], and the coefficient C is calibrated to match the ED model and account for the effect of latent heat. The track-scale model is more computationally efficient than the beam-scale model due to the increased time increment Δt , allowing fewer computations over the same track length. The time increment is dictated by the displacement equation ($\Delta t = v_s \Delta t$) and the terminal points (x_{start} , x_{end}) of the scanned laser track.

5.3.3 Implementation of Heat Dissipation

The standard equations (Newton's laws) for heat dissipation during LPBF are taken from [31] and are applied to the two models. The equations developed by Sih and Barlow [101] are used to simulate the energy loss due to radiation. The overall emissivity is expressed as:

$$\varepsilon = A_H \varepsilon_H + (1 - A_H) \varepsilon_s \quad (5-4)$$

$$A_H = \frac{0.908\phi^2}{1.908\phi^2 - 2\phi + 1} \quad (5-5)$$

$$\varepsilon_H = \frac{\varepsilon_s \left[2 + 3.082 \left(\frac{1 - \phi}{\phi} \right)^2 \right]}{\varepsilon_s \left[1 + 3.082 \left(\frac{1 - \phi}{\phi} \right)^2 \right] + 1} \quad (5-6)$$

where ϕ is the powder bed relative density (65% from the machine settings), ε_s is the emissivity of the solid (0.22) [106], ε_H is the emissivity between adjacent powder particles, and A_H is the area fraction of pores. Open surfaces are accounted for using convective boundary conditions based on the work of Li et al. [16], and a value of $20 \left(\frac{W}{m^2 \cdot C} \right)$ is used as the coefficient for uniform natural convection. The ambient and initial temperatures for the model are both set to room temperature, 25°C.

5.3.4 Model Implementation in Finite Elements

The two heat transfer models (ED and HL) are implemented in Abaqus, a commercial finite element software. A part domain of $2.0 \times 0.5 \times 1.0$ mm is modelled to capture melt pool dimensions of the beam- and track-scale models, as shown in Figure 5-2. The domain dimensions are selected to ensure a stable melt pool during the simulation as studied in [53]. The powder layer thickness implemented in the model is 0.04 mm based on LPBF settings described in Laser Powder Bed Fusion Experimental Procedure. DC3D8 elements are used to mesh the substrate and powder layer. Based on a mesh sensitivity study, the powder region interacting with the laser is meshed with element dimensions of 10 μ m for the y and z directions, and 20 μ m for the x-direction. Coarser elements are employed for regions further from the laser heat source to decrease computation time.

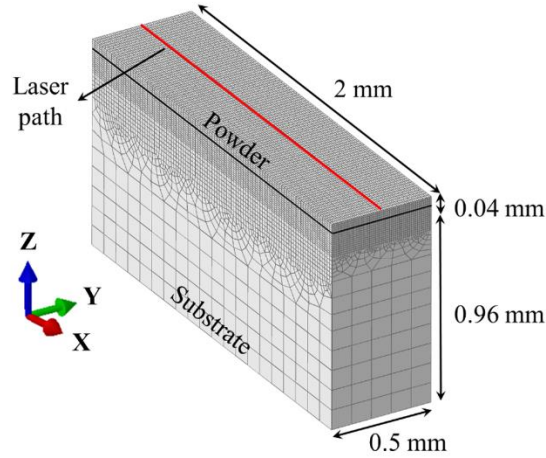


Figure 5-2: Meshed 3D model for the FE simulations. The powder layer and substrate are 0.04 and 0.96 mm thick, respectively. Mesh sizes for the powder are finer (10 μm) compared to the substrate to increase computational efficiency. The red line along the x-direction shows the laser path where the nodal temperatures are evaluated.

5.3.4.1 Material Properties

Temperature-dependent material properties such as specific heat capacity and thermal conductivity are used in the solid substrate and R65 powder, as demonstrated in Figure 5-3. The thermal conductivity was experimentally measured using the laser flash approach described in [107], and the specific heat capacity was measured by pulse heating and enthalpy methods from [108]. For the track-scale model, modified specific heat data is used to avoid failure in convergence. There is a spike in specific heat capacity around 1,000°C in Figure 5-3 (a) that could generate numerical instabilities. A line extended from the last point before the peak and a “cut-off temperature” of 1,100°C is used to modify the data, as done in [109]. This is necessary for Ni-based superalloys due to gamma prime phase transformation, resembling the approaches used in [110]–[113] for superalloys. However, this may not be required for the model’s application to other alloy systems depending on the specific heat capacity as a function of temperature. The heat conduction coefficient inside the melt pool is set 2.8 times higher than solid-state to compensate for the convective heat transfer due to fluid flow inside the melt pool (see Figure 5-3 (b)) [23]. The liquid state is not considered in the model, but a higher thermal conductivity is used for

nodal temperatures above the liquidus. The liquidus (1,381°C) and solidus (1,338°C) were obtained experimentally using differential scanning calorimetry (DSC).

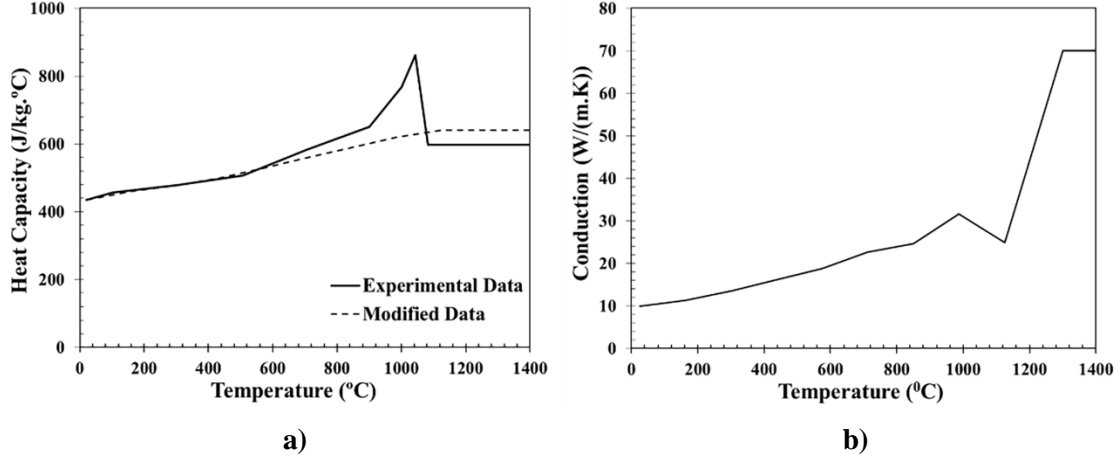


Figure 5-3: a) Experimental and modified temperature-dependent specific heat capacity and b) heat conduction as a function of temperature for R65.

For the powder bed, the effective thermal conductivity k is taken from [101], [114] and is defined as:

$$\frac{k}{k_f} = (1 - \sqrt{1 - \phi}) \left(1 + \frac{\phi k_r}{k_f} \right) + \sqrt{1 - \phi} \left(\frac{2}{1 - \frac{k_f}{k_s}} \left(\frac{1}{1 - \frac{k_f}{k_s}} \ln \left(\frac{k_s}{k_f} \right) - 1 \right) + \frac{k_r}{k_f} \right) \quad (5-7)$$

where k_s is the solid material thermal conductivity, k_f is the thermal conductivity of air, and k_r represents the thermal conductivity portion of the powder bed. The coefficient k_r accounts for radiation among particles, as described in the following equation taken from [114]:

$$k_r = \frac{4\sigma_r}{\left(\frac{2}{\varepsilon - 1} \right)} T^3 \frac{d_p}{k_f} \quad (5-8)$$

where d_p is the powder particle diameter. A value of $8,276 \left(\frac{kg}{m^3} \right)$ provided by the material supplier is used for the powder density and the following equation is used to determine the powder state density:

$$\rho_P = \phi \rho_s \quad (5-9)$$

where ρ_P is the powder bed density and ρ_s is the density of the fully dense material.

The latent heat of melting (247,075 J), obtained experimentally using DSC, is taken into consideration in the ED model but not in the track-scale model. This is because of the convergence issue described previously. The latent heat of evaporation is assumed to be 33 times larger than the melting energy based on [115] who used a similar alloy. The temperature range of the phase transformation for evaporation is assumed to be from 3,000°C to 3,500°C; however, these temperatures are not approached in the track-scale simulations.

5.3.4.2 Modelling Material State Transformation

During LPBF processing, the material undergoes phase changes from solid powder to a liquid in the melt pool and back to a consolidated solid material. The liquid phase of the material is modelled as solid state with higher conduction as explained in Material properties. Both FEM implementations (ED and HL models) account for the material state changes. Above the melting temperature, the powder to solid-state transition is incorporated within the model using the USDFLD subroutine code in Abaqus. The relative density of the material state is stored in an index as shown in the legend of Figure 5-4 (a). The powder value is 0.65 (shown in blue), while the consolidated solid and liquid states both have a value of 1 (shown in red). The nodal temperature and the region experiencing temperatures higher than the melting point are shown in Figure 5-4 (b). Comparison of the figures demonstrates the correlation of the material transition and the nodal temperature during the process.

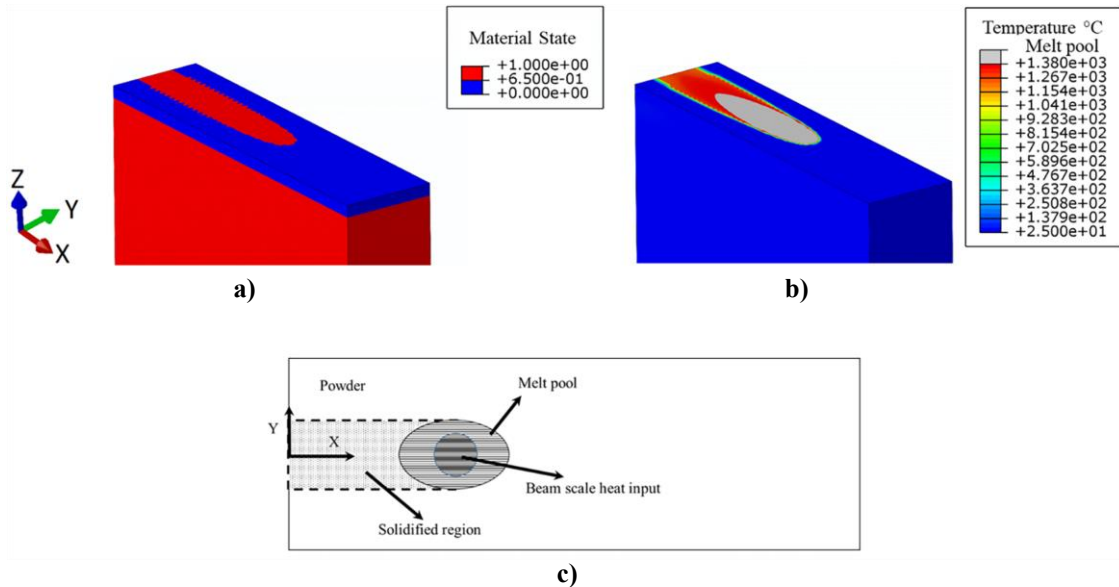


Figure 5-4: ED model simulation showing the material state transition and temperature distribution. In a), the powder (blue) and liquid/solid (red) zones are shown. b) Nodal temperature during the process. In c), a schematic of the material state transition occurring in the melt pool is shown.

The USDFLD subroutine is called at the beginning of every time step to read the material index of each integration point to determine the material state and resulting properties. Figure 5-5 (c) shows a schematic of the material state changes occurring at the beam scale. The heat source must always remain above the melt pool to accurately predict the material state transition. At time increment n , the DFLUX code applies heat to the material and the solver calculates the nodal temperatures. The material state at the time increment $n + 1$ is obtained from the nodal temperature of the previous increment (n). Consequently, the material state is always one time increment behind the applied heat source. Because the time increment in the ED model is small, the heat source is always situated above the melt pool allowing a low lag in material state transition. However, increasing the time step in the HL model causes significant delay in the material state transition and inaccuracy in thermal simulation, as shown in Figure 5-5 (a)-(d). Figure 5-5 (a), (b) show the nodal temperatures for subsequent time steps. The black ellipsoid shows the location of the applied heat. The lag of one increment between the heat input and the material state can be clearly observed in Figure 5-5 (c), (d), as the applied heat is one increment in front of the material state transition. To overcome any potential issue with the lag in phase transition,

a new method accounting for phase transformation is proposed. To resolve the problem presented in Figure 5-5 (a)-(d), the material state change is set to occur above 5% of the total energy absorption for the HL model, as shown in Figure 5-5 (e), (f). The value of 5% is calculated from the energy required to increase the material temperature to the melting point, which was used to predict the initial temperature of the activated material in [16]. This value might differ slightly for other materials but is not expected to influence the accuracy. of the results. The lag of one increment between the heat input and the material state is now eliminated. This approach enables faster convergence of line heat input models and improves the accuracy of the predictions.

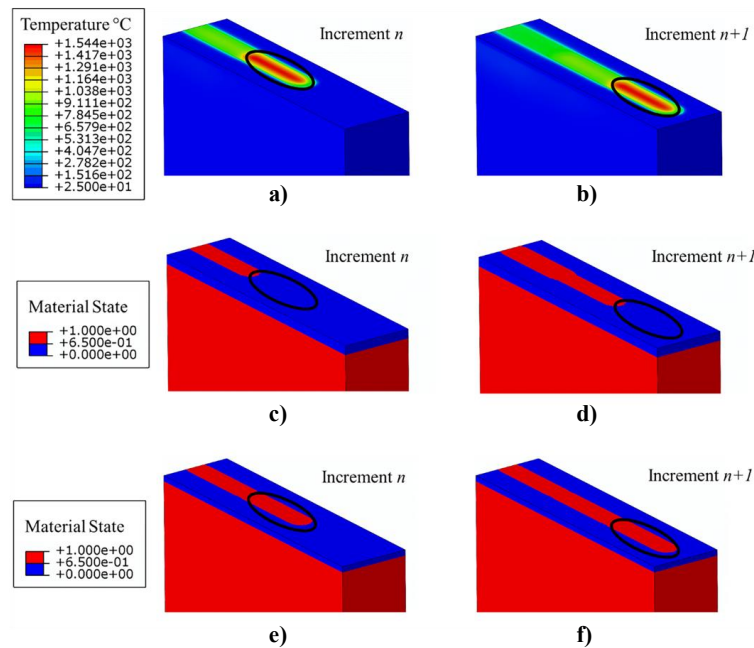


Figure 5-5: Nodal temperatures are shown in increments a) n and b) n + 1. The material state transition showing the lag effect in increment c) n and d) n + 1. The modified material state transition is shown in increment e) n and f) n + 1 without lag. Powder state is shown in blue and liquid/solid state is shown in red. The black ellipsoid shows the location of the applied heat.

5.4 Results and Discussion

5.4.1 LPBF Melt Pool Geometry Analyses

Figure 5-6 shows the measured melt pool dimensions (depth and width) associated with the 18 different line energies described in Figure 5-6 (a). Each set of adjacent Figure 5-6 (a) – (f) shows the melt pool depth and width with identical laser powers for different laser speeds. The error bars represent the maximum and minimum values of the five experimental repeats.

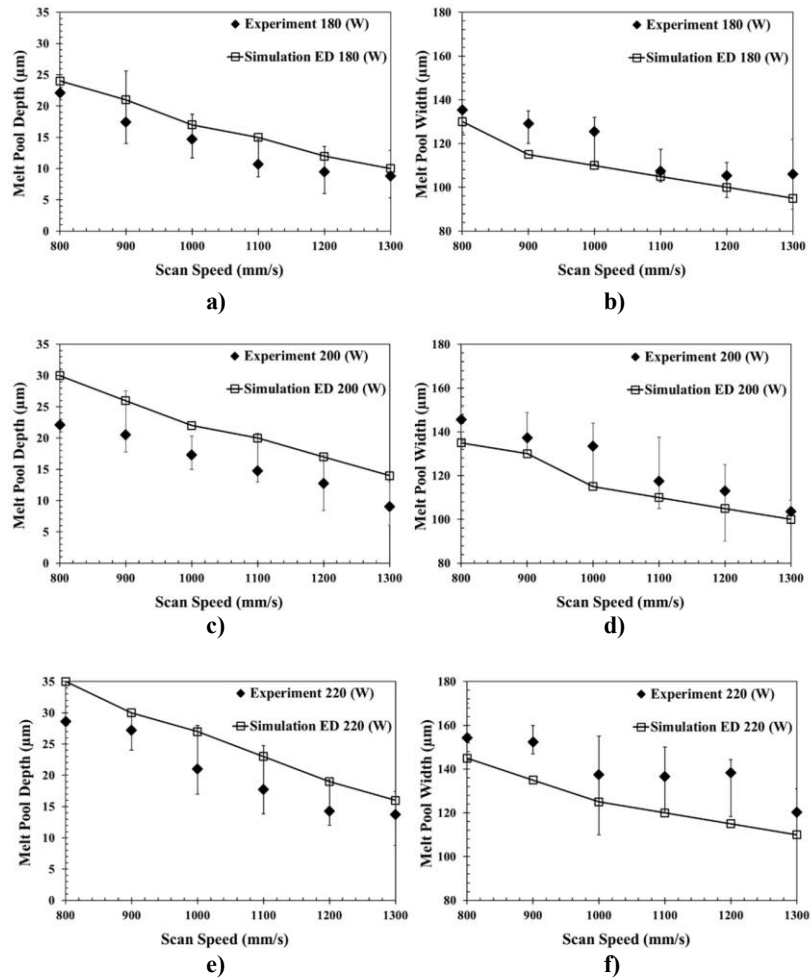


Figure 5-6: Comparison between experimental and ED simulation melt pool widths and depths for different laser powers: (A) and (B) 180 W (C) and (D) 200 W, and (E) and (F) 220 W.

As laser power increases, line energy increases, consequently leading to larger melt pool dimensions. Table 5-1 shows how the melt pool depths and widths increase at average rates of $16.4 \frac{\mu\text{m}}{W}$ and $54.59 \frac{\mu\text{m}}{W}$ with laser power in Figure 5-6. Conversely, as the laser speed increases, melt pool depths and widths decrease at average rates of $2.87 \frac{\mu\text{m}}{(\text{mm/s})}$ and $7.13 \frac{\mu\text{m}}{(\text{mm/s})}$, respectively. Therefore, the laser power has more significant effect on the melt pool size than laser speed. Current results are consistent with previous researchers (Fu and Guo 2014; Irwin and Michaleris 2016) who also reported a stronger influence of laser power on the melt pool geometry.

Table 5-1: Comparison of the melt pool depths and widths for the ED models and experiments with increasing laser speed and power.

	Laser Speed		Laser Power	
	Width ($\frac{\mu\text{m}}{(\text{mm/s})}$)	Depth ($\frac{\mu\text{m}}{(\text{mm/s})}$)	Width ($\frac{\mu\text{m}}{W}$)	Depth ($\frac{\mu\text{m}}{W}$)
Experimental	-7.13	-2.87	+54.59	+16.4
ED Model	-6.86	-3.24	+39.58	+21.25

The melt pool aspect ratio defined as melt pool depth divided by melt pool width shown in Figure 5-6 are plotted in Figure 5-7 (a) with respect to the line energy density. The melt pool aspect ratio increases with increasing line energy density. The heat transfer mode generally transitions from conduction to keyhole mode between an aspect ratio of 0.4–0.5 [116]–[118], above which melt pools are in keyhole mode. Since the aspect ratio falls below 0.2 for each case, all laser conditions evaluated in this study are in conduction mode. The absence of a bell-shaped melt pool for the highest line energy density in Figure 5-7 (b) confirms that the heat transfer mode is not keyhole. Additional studies would be required to validate the proposed HL model for laser heat sources operating in keyhole mode.

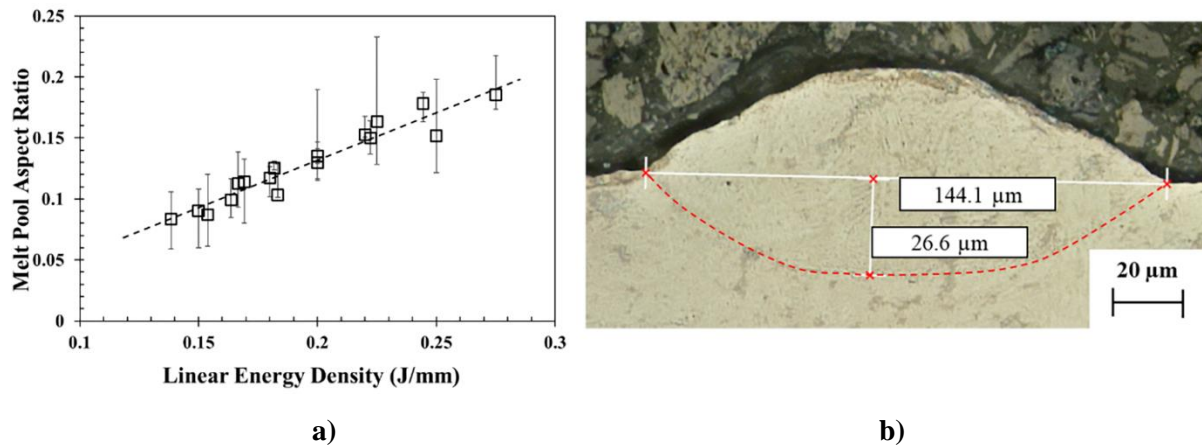


Figure 5-7: a) Effect of linear energy density (J/mm) on the experimental melt pool aspect ratio (depth over width). b) Melt pool cross-section obtained with a laser power of 220 W and laser speed of 800 mm/s. The red dashed line outlines the melt pool boundary.

5.4.2 ED Model Evaluation

The laser radius (r_l) and H coefficient correspond to the experimental laser beam radius (60 μm) and powder bed thickness (40 μm) as recommended in [100]. The absorption coefficient (η) for Ni-Based superalloys is 0.5 as per [105]. The ED heat input model is validated with the experimentally measured melt pool dimensions. The method used to measure the simulated melt pool geometry is shown in Figure 5-8. The grey region represents the area above the liquidus temperature, and only the grey portion within the substrate is considered for melt pool measurement. The difference between the simulated and measured melt pool depths and widths are shown in Figure 5-6. Trends on the effect of laser speeds and powers on the melt pool geometries predicted by the ED model match the experimental observations. The simulated melt pool depths and widths increase at average rates of $21.25 \frac{\mu\text{m}}{\text{W}}$ and $39.58 \frac{\mu\text{m}}{\text{W}}$, respectively, as the laser power increases and decreases at average rates of $3.24 \frac{\mu\text{m}}{(\text{mm/s})}$ and $6.86 \frac{\mu\text{m}}{(\text{mm/s})}$, respectively, when laser speed increases (see Table 5-1). The predicted melt pool depth and width are on average within 4.2 and 11.0 μm of the experimentally measured values. This lies within the experimental error range derived from melt pool measurement. Henceforth, it can be concluded that the ED model accurately predicts the melt pool geometry.

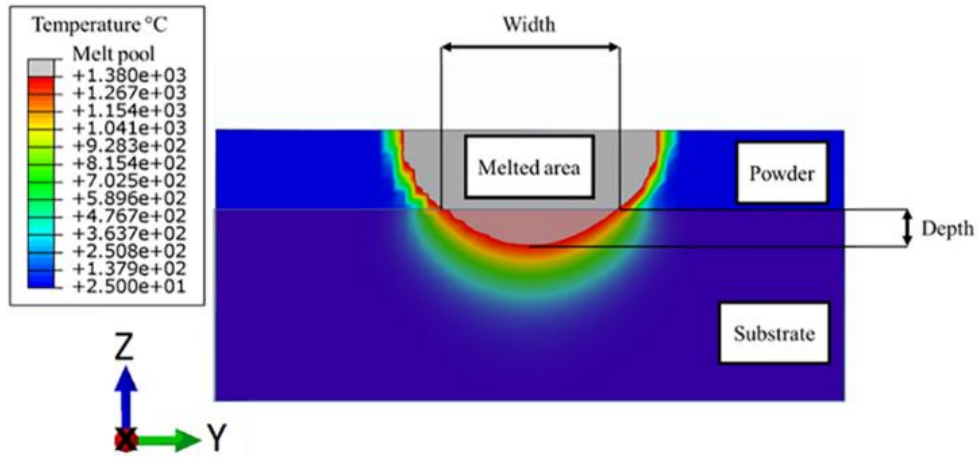


Figure 5-8: Temperature variation surrounding the melt pool for the ED heat input model with 200 W laser power and 1,000 mm/s laser speed. The melted zone is shown in grey, the melt pool in light red, the powder state in blue, and the substrate in dark blue.

5.4.3 HL Model Calibration

Following Irwin and Michaleris's methodology [19], the time increment (Δt (s)) of the HL model is normalized over the laser travel distance as follows:

$$\tau = \frac{v_s \Delta t}{r_l} \quad (5-10)$$

where v_s is laser speed (m/s) and r_l is beam radius (m). The parameter τ links the laser travel distance with r_l . The heat source length of the HL model is equal to the ED beam radius when $\tau = 1$. When $\tau > 1$, the heat source length is larger than the ED beam radius, reducing simulation time. The H , r_l , and η values are maintained from the ED model due to their dependency on the experimental set-up. As the ED model shows good agreement with experimental results, it is used as a reference to calibrate the coefficient C and validate the accuracy of the HL model in terms of temperature distribution and cooling rate. The coefficient C is determined by minimizing the difference in the nodal temperatures in regions surrounding the melt pools between the HL and ED models. A line energy of $200 \frac{J}{mm}$ is used for calibration and Figure 5-9 shows where the nodal temperatures are extracted. Cross-sections of the

simulation results along the laser track are taken at different times. The number of cross-sections considered in the calibration is varied between three and nine depending on the value of τ due to the fixed part length. The cross-sections are taken ahead of, inside of and following the laser beam heat source. For each cross-section, only the nodal temperatures outside the melt pool (outside the grey region in Figure 5-9), are considered for calibration. As the laser heat input is lumped into a line, changing the value of τ changes the peak temperature in the melt pool. Thus, the temperatures inside the melt pool cannot be used for calibration. The calibration coefficient (C) is set to 1.2 independently of the normalized increment time (τ).

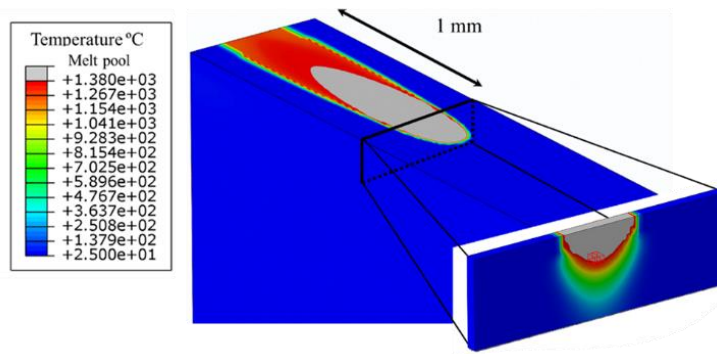


Figure 5-9: Example of an ED laser track simulation used for HL model calibration. The melt pool is shown in grey color. The nodal temperatures of the elements surrounding the melt pool are used for calibration of the HL model. The highlighted region (red cube) at the center of the cross section at the melt pool boundary is used to study the cooling rate in cooling rate.

5.4.4 Hybrid Line Model Evaluation

5.4.4.1 Computational efficiency

The time required to solve the model is dependent on the number of time increments and iterations for each increment. While the term τ has a linear relationship with the time increment size, the number of iterations required for convergence increases with a larger time increment. Figure 5-10 shows the ratio between the time required to solve the HL and ED models $\left(\frac{Time_{ED}}{Time_{HL}}\right)$. The HL model is 330–1,500 times faster than the ED model as τ increases from 5 to 20. Even though the ratio should be close to τ (based on Eq. (5-3) and Eq. (5-10)), it is significantly larger in Figure 5-10. This is because the heat capacity

relationship with temperature is simplified in the HL model and the latent heat is not considered as explained in Material properties. Consequently, the simulation requires a reduction of the time increment size by an average of $\Delta t = 7 \times 10^{-7}$ (for ED model) to overcome the convergence issue created by a sudden change in specific heat capacity shown in Figure 5-3 (a). The higher computational efficiency of the HL model over the ED model is thus due to simplified material properties and the integrated heat input equation.

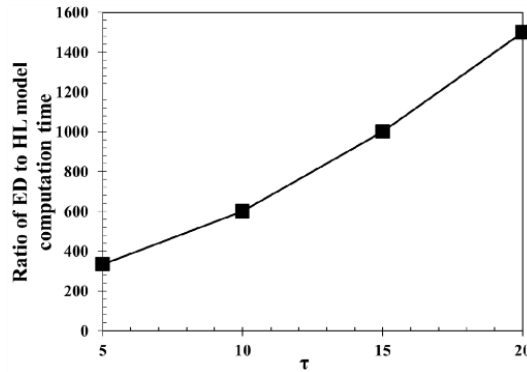


Figure 5-10: Comparison of $\left(\frac{Time_{ED}}{Time_{HL}}\right)$ as a function of τ showing the computational efficiency of the HL model compared to the ED model.

5.4.4.2 Melt Pool Geometry

The heat input energy in the HL model is simplified from the ED model resulting in inaccuracies in prediction of the melt pool geometry. Nevertheless, the HL model with small time integration step ($\tau = 5$) offers reasonably accurate results while being 330 times faster than the ED model. Figure 5-11 shows the predicted melt pool dimensions (depth and width) for the HL model with $\tau = 5$. The trends on the effect of laser speeds on the melt pool depths predicted by the HL model match the experimental observations. As the laser speed increases, the melt pool width and depth decrease by average rates of $8.29 \frac{\mu\text{m}}{(\text{mm/s})}$ and $3.54 \frac{\mu\text{m}}{(\text{mm/s})}$, respectively. The predicted melt pool depth and width are on average within 5.4 and 27.2 μm of the experimentally measured values. When the integration time step increases above $\tau = 5$, the simulated melt pool size decreases significantly due to the reduction in peak temperatures.

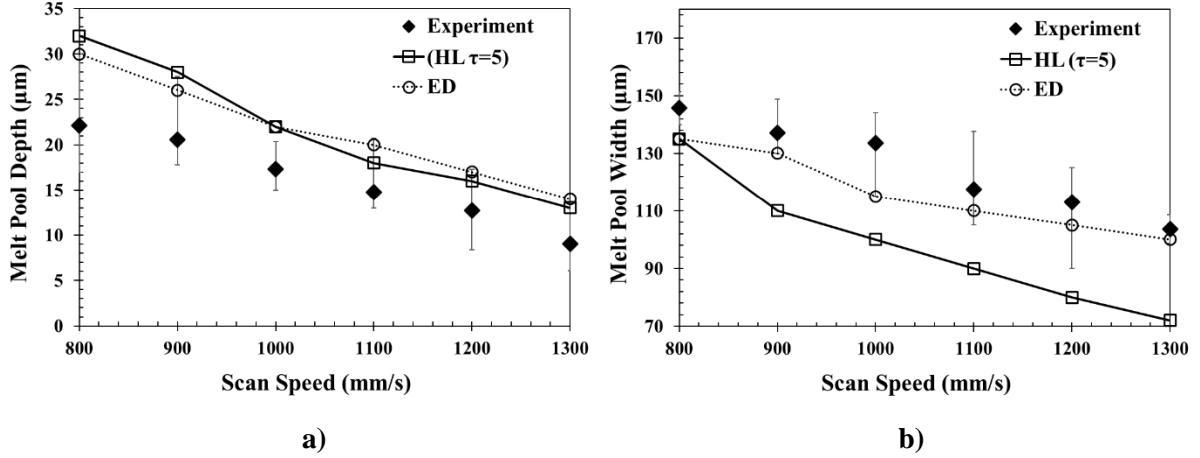


Figure 5-11: Comparison of the experimental and HL simulation ($\tau = 5$) melt pool a) depth and b) width for 200 W laser power.

5.4.4.3 Laser Track Temperature

Simulation of the laser track temperature is necessary to understand the microscopic material behaviour during LPBF since it has a strong influence on the formation of microstructural inhomogeneity in Ni-based superalloys. This includes formation of bimodal grain structures resulting in strong thermo-mechanical anisotropy of the as-produced specimens discussed in [119], [120]. Detrimental phases and micro-segregation can arise during the LPBF process, promoting micro-cracking and low part ductility [117], [121]. The nodal temperatures predicted by the ED and HL models are compared in Figure 5-12. The temperature distributions are taken on the top surface along the laser path, as shown by the red line in Figure 5-2 when the laser is located at 1.8 mm (90% of the simulation). The temperature distributions are predicted for three line energies, 275, 200, and 138 J/mm, in Figure 5-12 (a)–(c), respectively. Both models demonstrate increasing maximum temperature with increasing laser power, consistent with previous experimental observations in [119], [122]. However, the HL model fails to capture the maximum temperature under the laser beam location (at 1.8 mm) because the heat input is homogeneously distributed along the time increment. As the τ value increases, the time step increases, and the maximum temperature decreases when compared with the ED model. The HL model exhibits plateaus in the temperature profiles (see numbers 1, 2 and 3 in Figure 5-12 (a)). The length of each plateau is proportional to the τ value and thus to the time step used for integration along the laser path.

As the temperature decreases, the two models start converging in Figure 5-12 for all laser conditions. The errors in temperature predictions between the two models are given in Table 5-2 for various temperature ranges. Below 1,400°C, the temperature error varies between 1 and 15% for $\tau = 5$ and $\tau = 10$. Between 1,400°C and 1,300°C, the error is only 1.5% for $\tau = 10$. This is when material solidifies (liquidus = 1,381°C and solidus = 1,338°C). The error is approximately 12% within the solvus temperature range ($\sim 1,110^\circ\text{C}$ [123]). Both temperature ranges are critical to the LPBF of R65 since they are associated with the microcracking mechanism often observed in high γ' Ni-based superalloys [117], [121], [124] and the formation of carbides and gamma prime (γ') [123].

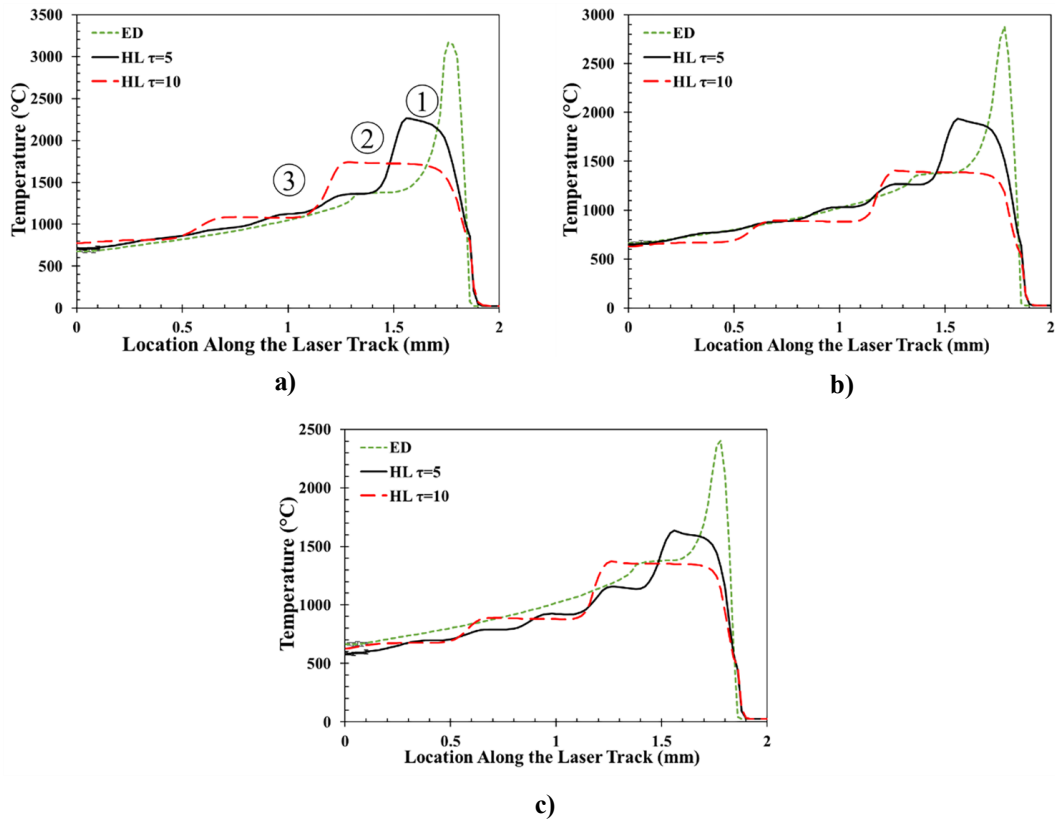


Figure 5-12: Nodal temperatures along laser paths in the ED model and the HL model for $\tau = 5$ and $\tau = 10$. The laser powers and speeds are a) 220 W–800 mm/s b) 200 W–1,000 mm/s and c) 180 W–1,300 mm/s.

Table 5-2: Error in temperature prediction between ED and HL models for different temperature domains. The laser power and speed are 200 W and 1000 mm/s, respectively (Figure 5-12 (b)).

Temperature range (C°)	1400-1300	1300-1200	1200-1100	1100-1000	1000-900
$\tau = 5$	14.5%	2.2%	4.1%	1.85%	1.7%
$\tau = 10$	1.5%	13%	11.7%	14%	6%

5.4.4.4 Cooling Rate

The cooling rate controls the thermal gradient causing thermal stresses and strains in the fabricated parts [122]. Therefore, the process-induced cooling rate must be captured accurately during the simulation. A comparison between the cooling rates obtained from the ED and HL models is shown in Figure 5-13. Three different laser conditions with line energies of 275, 200 and 138 J/mm are compared in Figure 5-13 (a) – (c), respectively. The cooling rates are evaluated at the melt pool boundary central to the laser track because it is a critical region for the formation of residual stresses. This is shown by the red cube element in the cross-section subset in Figure 5-9. As the melt pool depth depends on the energy input, the results are captured at locations of 40 μm , 22 μm , and 13 μm under the powder layer for line energies of 275, 200, and 138 J/mm, respectively. The maximum cooling rates obtained are on the order of 10^5 °C/s, one order of magnitude lower than values reported in literature ($\sim 10^6$ °C/s [125]). Lower cooling rates are attributed to the extraction of results as the laser reaches the end of the track (2 mm in Figure 5-2).

Figure 5-13 shows that the cooling rates decrease rapidly and reach steady state around 2°C/s, 1 s after the track is printed. The average errors between the ED and HL models are 5.98, 5.37, 6.86, and 8.2% for $\tau = 5, 10, 15,$ and 20 , respectively. Both simulations show that increasing the line energy increases the cooling rate as it increases the maximum nodal temperatures shown in Figure 5-12. At 1.2 ms, the cooling rate decreases from 2.4×10^5 °C/s to 1.1×10^5 °C/s when the laser power drops from 220 to 180 W.

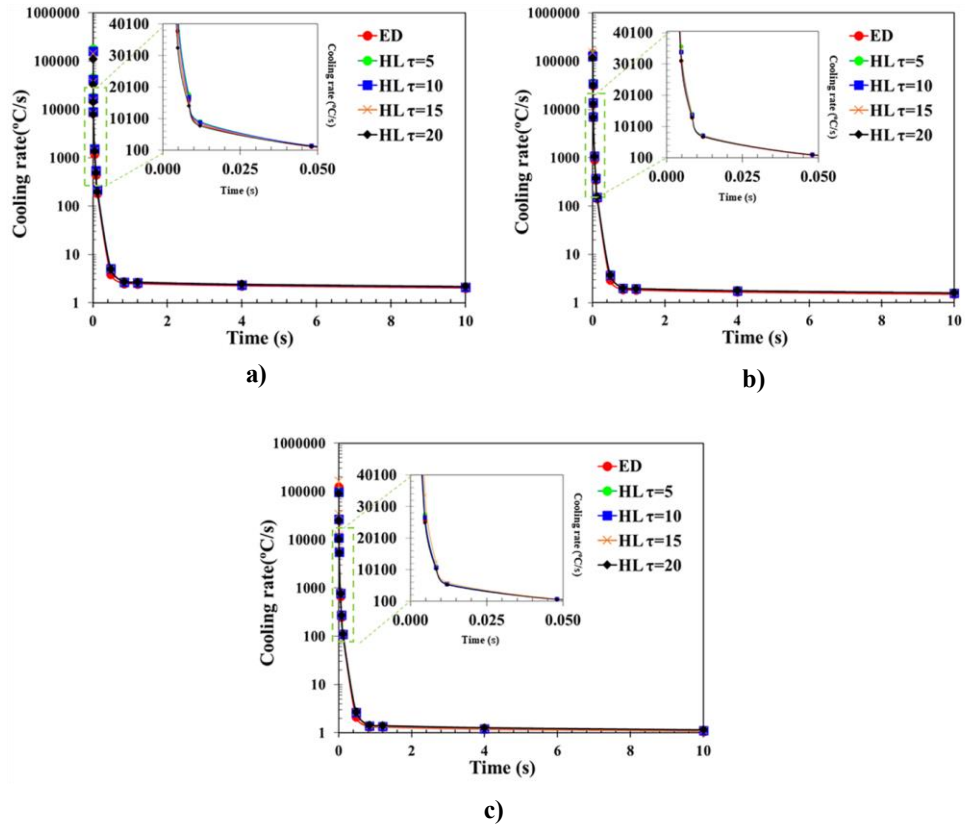


Figure 5-13: Cooling rate profiles for the following laser powers and speeds: a) 220 W–800 mm/s b) 200 W–1,000 mm/s, and c) 180 W–1,300 mm/s.

5.4.4.5 Temperature Distribution

The simulation of full-scale parts requires the temperature distribution to be accurately simulated. This entails accurate prediction of nodal temperatures, cooling rates, and the heat transfer between the different material states (liquid, solid and powder). Figure 5-14 (a), (b) show the temperature distributions in the ED and HL model with $\tau = 10$. The temperature distributions are taken 1.2 ms after track completion to minimize image contour level contrast due to peak temperatures. The nodal temperatures are higher at the end of the track since this is the last location of the laser heat source. The HL model temperature is higher at this position due to the length of its heat source. In both cases, the heat energy is mostly distributed within the solidified region and the substrate. The temperature gradients along the x, y, and z directions are similar for both models.

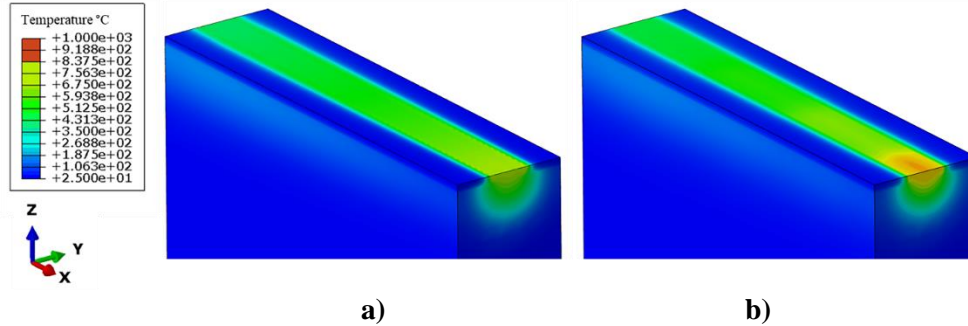


Figure 5-14: Temperature distributions captured 1.2 ms after the track simulation finishes for a) the ED beam scale and b) the HL track-scale model ($\tau = 10$).

5.5 Conclusion

In this study a new track-scale thermal model referred as the HL heat input model is developed to predict the temperature distribution during the LPBF process. The temperature dependent specific heat capacity and thermal conductivity are experimentally measured and accounted for in both the ED and HL models. The results of the HL model are evaluated by comparing the predicted temperature distribution, cooling rate and melt pool dimensions to a beam-scale (ED) model and a set of LPBF single track experiments.

The ED beam-scale model was first validated by comparing the predicted melt pool geometry with experimental observations. Results show that the ED model can capture the melt pool geometry within few microns and the trends of the effect of laser speeds on the melt pool geometry within 10% error.

The comparison between the ED and HL models shows that the new track-scale model is a versatile substitute for a beam-scale model. At low τ value, the model can predict the effect of laser parameters on the melt pool geometry. The predicted melt pool depth deviates by approximately 5 μm , while the width prediction is less accurate due to variation in the peak temperature. The temperature distribution inside the laser path is in good agreement with the beam-scale model. This is specifically true for temperatures below the solidus where the deviation from the ED model remains below 5%. The sub solidus temperature range has the strongest impact on the microstructure generated during LPBF of Ni-based superalloys. By increasing τ , some of the resolution is lost on the temperature profile resulting in increased error in peak temperature and melt pool geometry prediction. However, the cooling rate,

which controls micro- and macroscopic stresses remains below 10% error with respect to the beam scale model. This allows for significant computational gains. At $\tau = 5$, the HL model is 330 times faster than the ED model and can easily become more than 1,000 times faster by increasing the τ value. The presented model is beneficial for predicting the in-process temperature field and thermal history that influences the resulting microstructure and mechanical properties of the printed material.

Chapter 6

Developing a New Line Heat Input Model: Part 2-Mechanical Model

In this chapter, the mechanical model for previously developed thermal model is presented. The mechanical model once applied on a track then for an actual part. To enhance the computational time and mesh coarsening technique was implemented. The validation was conducted with both simulation and experimental results. For the simulation reference the results from the mechanical model of the conventional beam scale heat input model was used as a reference. For the experimental approach, 12 components were printed with different printing pattern and laser power then the residual stress was evaluated using XRD. The simulation results provide valuable information regarding the effect of laser power and printing patterns on generated residual stress. Finally, the impact of created residual stress on quality and LBH was studied.²

The chapter presents an accepted manuscript of an article published in the Journal of Frontiers in Materials.

Frontiers in Materials. 2021 Nov; 8:478. Doi: 10.3389/fmats.2021.753040

6.1 Introduction

Nickel-based (Ni-based) superalloys possess a combination of outstanding mechanical and physical properties at high temperatures, making them attractive for application in gas-turbine and jet-engine components [104], [126], [127]. In aeroengine and gas turbine power industries, there are numerous geometrically complex components made with intricate serpentine cooling paths and thin wall sections, including the combustor, diffuser, and nozzle. Laser powder bed fusion (LPBF) is a promising route for the construction of near net shape, high-tolerance components capable of withstanding extreme environment and loading conditions [119]. However, thin-wall Ni-based superalloys are susceptible to the formation of cracks and distortion during LPBF processing [10].

The defects in superalloy LPBF parts are due to the rapid cooling rates reported to be on the order of 10^6 K/s during LPBF [125]. These high cooling rates result in the formation of metastable microstructures with significant residual stresses [122], [128]. Controlling and predicting the residual stresses during LPBF is not trivial. Both the magnitudes and distribution of residual stresses in AM components are governed by several factors, including: material properties, volumetric change due to phase transformation or precipitation, geometry of components, the position of specimens, processing parameters, baseplate temperature, and laser scanning pattern [129]–[131].

Researchers often only consider the effect of residual stresses at the part scale. Different approaches have been developed to simulate the residual stress at the part-scale level [92], [132], [133]. The inherent strain method induces strain in a small region of a part and applies it to the entire part to exclude the thermal simulation [8], [87], [90]. The “lumped” approach combines multiple layers of a build and applies a uniform heat source over the entire layer [17], [18]. These methods allow prediction of part distortion with reasonable computation time, but lack resolution at the microscopic scale, which is required to study the effect of laser parameters and printing patterns on the LPBF process.

Residual stresses during LPBF are attributed to the large spatiotemporal thermal gradients from localized rapid heating and cooling [37]. To fully capture the effect of residual stresses, knowledge of the thermomechanical behavior of the material at different length scales: macro-stresses observed at the part scale level to micro-stresses at the grain dimension must be acquired [37]. However, beam-scale modeling is not feasible at the part scale due to the high computational costs, motivating the development of track-scale models [66], [72], [134], [135]. The first part of this series introduces a new

track-scale model to account for the thermal behavior at the microscopic scale. The new Hybrid Line (HL) heat input model is derived from the 3D exponentially decaying (ED) heat input model from [122]. The HL model accounts for the material state transition from powder to consolidated solid material and is calibrated for high gamma prime Ni-based superalloys by incorporating thermo-mechanical properties of the powder and fully dense material. The HL model increased the computational efficiency significantly (up to 1,500 times faster) compared to the ED beam-scale model. This track scale simulation allows thermal behavior at the microscale to be applied on the part scale, enabling high accuracy and fast simulation times.

This second part of this series is devoted to the thermomechanical simulation of the LPBF process. Coupling the HL thermal model, developed in part I of this series, as input to a mechanical model, enables prediction of the residual stresses at the track and part scales. Firstly, a single-track simulation is applied to compare the residual stresses in the HL track scale and ED beam-scale models. Secondly, part-scale simulations of thin-wall builds are completed using the HL track-scale models for comparison with experimentally measured residual stresses in LPBF parts. Specimens with different laser powers and printing patterns are used to evaluate the simulations. The computational efficiency of the thermomechanical model is further enhanced using a mesh coarsening technique in Abaqus.

6.2 Material and Experimental Methods

6.2.1 Material Composition

The material considered for LPBF is a gas-atomized high- γ' Ni-based superalloy RENÉ 65 (R65) powder produced by ATI Powder Metals, which predominantly consists of spherical particles ranging in size from 12 to 42 μm with a D50 size of 19 μm . The R65 chemical composition is 15% Cr, 13% Co, 4% W, 4% Mo, 3.5% Ti, 2.1% Al, 0.9% Fe, 0.7% Nb, 0.05% Zr, 0.04% Ta, 0.01% B, and the balance is Ni.

6.2.2 LPBF Procedure

Three Twelve part-scale specimens are printed using an Aconity MIDI LPBF machine in an Argon environment to validate the thermomechanical HL model. The printed size of each specimen is $5 \times 1.2 \times 0.5$ mm (length \times height \times width) based on simulation time and X-Ray Diffraction (XRD) residual

stress measurement considerations. Specimens are oriented at a 25° angle with respect to the recoater direction. Each component is spaced at least 10 mm apart to avoid negative impacts of adjacent laser processing. For this reason, the two nearest specimens were not printed subsequently. This eliminates concerns with the thermal effects of neighboring parts [136], [137].

The specimens are printed with a laser speed of 1,000 mm/s, layer thickness of $40\ \mu\text{m}$, laser radius of $60\ \mu\text{m}$ and hatch spacing of $90\ \mu\text{m}$. A series of three different laser powers and four different laser scan path patterns are studied. The three different laser powers are, 180, 200, and 220 W, respectively. The four laser scanning patterns, referred to as longitudinal, perpendicular, 90° and 45° rotations are shown in Figure 6-1 (a). Figure 6-1 (b) shows how the rotations are completed between the layers. Longitudinal and perpendicular scanning patterns have 0° rotations between the layers. This allows comparison of the vector length effect (longitudinal = 5 mm and perpendicular = 0.5 mm) on residual stresses. The effect of the rotation angle between layers on the residual stress is evaluated using the 90° and 45° rotation patterns.

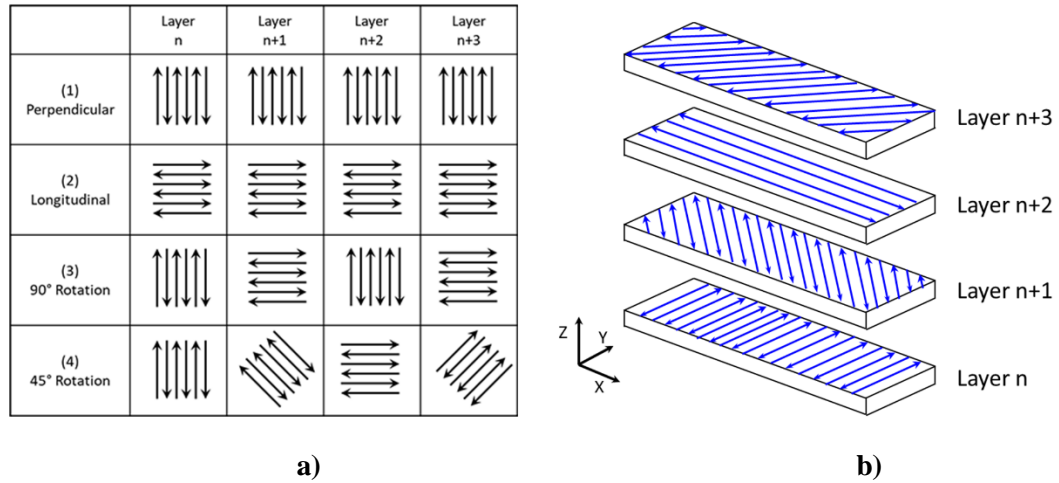


Figure 6-1: a) The four different printing patterns used to compare the HL models with experimental results. The perpendicular and longitudinal patterns have short (0.5 mm) and long (5 mm) vector lengths with zero rotation angle between the layers. The 90° and 45° rotations patterns have counterclockwise rotation of the laser direction after each layer. b) An example of the 45° rotation pattern is given for four layers.

6.2.3 Residual Stress Measurement

The residual stresses in the part-scale specimens are measured using a μ -X360s residual stress analyzer, manufactured by PULSTEC. The machine is equipped with a Cr K α source and a 0.3 mm collimator. The Young's Modulus and Poisson's Ratio are defined in the machine settings to calculate the residual stress from the measured strain. The $\cos \alpha$ method [138], [139] is used to measure the residual stress, where X-rays are 360°-omnidirectionally diffracted from the samples around the path of incident X-rays and are detected by two-dimensional detectors. The residual stresses were evaluated 3 times at the center of the specimen. The XRD scan time is about 10 min to allow approximately 500 measurements over the 360° debye ring.

Past studies have shown that surface roughness significantly affects the residual stress measurements [140]. Moreover, the residual stress of the final LPBF build layers is not essential as the free surface allows stress relaxation. It has also been found that the residual stresses are higher inside the LPBF parts [136]. For these reasons, the center section of the specimen is selected for residual stress measurement. Samples are mounted, ground, and polished using standard metallographic procedures. Approximately 0.6 mm (half of the sample height) is removed during sample preparation. To preserve the residual stresses, the samples are mounted while still attached to the base plate. The final polishing step is performed in a Beuhler Vibromet (TM) 2 Vibratory Polisher with 0.05-micron alumina solution (MasterPrep) for 72 h to ensure that the mechanical stresses induced by the mechanical polishing are minimized. While it is acknowledged that the removal of half the specimen affects the residual stress magnitudes, the differences in residual stresses between the different scanning patterns and laser powers are preserved.

6.3 Modeling

Two sequentially coupled thermo-mechanical models are implemented in Abaqus (a Dassault Systems finite element software) to evaluate the accuracy and computational time of the models. Firstly, a single-track model is implemented for comparison between HL and ED models introduced in Part I of this series [135]. The beam-scale (ED) model is a baseline for comparison due to its greater accuracy in replication of the heat input profile of the energy source [19], [141]. Secondly, a HL-based part-scale

model is developed for comparison with the experimental residual stress measurement described in Residual Stress Measurement.

The equations governing the thermal behavior of the ED and HL models has been previously described in Part I [135]. Standard equations governing the mechanical behavior have been used for both HL and ED models. Thermal gradients predicted by the thermal models are input into the mechanical models to predict the resulting stresses. The total strain increment $\Delta\varepsilon_{ij}$ is subdivided as per Eq. (6-1):

$$\Delta\varepsilon_{ij} = \Delta\varepsilon_{ij}^E + \Delta\varepsilon_{ij}^P + \Delta\varepsilon_{ij}^T + \Delta\varepsilon_{ij}^{\Delta V} + \Delta\varepsilon_{ij}^{Trp} \quad (6-1)$$

where $\Delta\varepsilon_{ij}^E$ is the elastic strain, $\Delta\varepsilon_{ij}^P$ represents the plastic strain, $\Delta\varepsilon_{ij}^T$ is the thermal strain, $\Delta\varepsilon_{ij}^{\Delta V}$ is volumetric strain due to phase transformation, and $\Delta\varepsilon_{ij}^{Trp}$ is transformation plasticity. In this study, $\Delta\varepsilon_{ij}^{\Delta V}$ and $\Delta\varepsilon_{ij}^{Trp}$ are assumed to be zero, consistent with previous studies [42]. The thermal strain increment $\Delta\varepsilon_{ij}^T$ is obtained from thermal expansion relation in Eq. (6-2) as follows:

$$\Delta\varepsilon_{ij}^T = \alpha\Delta T\delta_{ij} \quad (6-2)$$

Where α is the thermal expansion coefficient, ΔT is the temperature rise and δ_{ij} is the Kronecker delta function ($\delta_{ij} = 1$ if $i = j$, $\delta_{ij} = 0$ if $i \neq j$). The resulting stress increment is obtained from the elastic strain as follows:

$$\Delta\sigma_{ij}^E = D_{ijklm}\Delta\varepsilon_{lm}^E \quad (6-3)$$

Where D_{ijklm} is the fourth order isotropic elastic stiffness tensor calculated from Young's Modulus (E) and Poisson's Ratio (ν):

$$D_{ijklm} = \frac{E}{1+\nu} \left[\frac{1}{2}(\delta_{ij}\delta_{lm} + \delta_{il}\delta_{jm}) + \frac{\nu}{1-2\nu}\delta_{ij}\delta_{lm} \right] \quad (6-4)$$

The temperature-dependent material properties of R65, including density, specific heat, latent heat, thermal conductivity, incorporated in the simulations are given in Part I [135]. The HL model calibration coefficient ($C = 1.2$) is maintained from Part I of this series [135]. A summary of the temperature-dependent thermal material properties is provided in Table 6-1. The Young's Modulus, Poisson's Ratio, plasticity, and thermal expansion are taken from [142]. The Young's Modulus for the powder state of the material is assumed to be 1% of the fully dense value at room temperature,

accounting for the negligible powder stiffness. A linear temperature-dependent piecewise stress-strain relationship accounts for the elasto-plastic behavior as has been done for similar materials in [142].

Table 6-1: Temperature-dependent thermal material properties for RENÉ 65

Temperature (°C)	Thermal Conductivity (W/(m.K))	Heat Capacity (J/(kg.°C))	
		ED	HL
25	9.9	435	435
162.5	11.35	462	462
300	13.6	477	477
437.5	16.15	496	496
575	18.74	533	533
712.5	22.6	583	560
850	24.7	623	590
987.5	31.6	751	620
1125	24.95	597	640
1300	70	597	640

6.3.1 Single-Track Models

The model geometry for the single-track simulations (HL and ED) is shown in Figure 6-2. The substrate is 2 mm long, 0.96 mm high, and 0.5 mm wide. A 0.04 mm thick powder layer corresponding to the experimental setup is added on top of the substrate. The powder and substrate are divided with the dashed blue line in Figure 6-2. The substrate is fixed to its surroundings to constrain movement in all directions. The laser path direction is aligned with the x-direction in Figure 6-2. The single-track simulations are completed with a laser power of 200W and laser speed of 1,000 mm/s. The residual stresses are evaluated along the longitudinal and transverse directions, named lines 1 and 2 in Figure 6-2. Based on previous work [135], a value of $20 \left(\frac{W}{m^2 \cdot ^\circ C} \right)$ and 0.4 are used for the convection and

radiation heat loss, respectively. The ambient and initial temperatures for the substrate are both set to room temperature, 25°C. DC3D8, and C3D8 elements in Abaqus are implemented for the thermal and mechanical models, respectively.

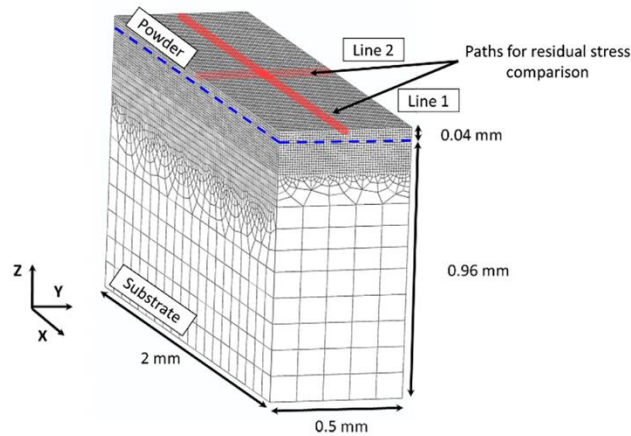


Figure 6-2: Track-scale model mesh showing the dimensions of the substrate and powder bed. The laser movement is parallel to the X-direction. The residual stresses are evaluated along the two lines highlighted in red.

To determine the minimum mesh size required for the thermal and mechanical models a mesh sensitivity study is conducted. The minimum required mesh size from the sensitivity study is maintained for both the thermal and mechanical models. The region over which the laser passes is meshed with elements whose dimensions are 10 μm for both y and z-directions, and 20 μm for the x-direction in the ED model. For the HL model, the laser-affected region is meshed with elements having dimensions of 20 μm in y and z, and 30 μm in the x-direction. In addition, coarser elements are employed for regions further from the laser heat source to decrease the computational time, as shown in Figure 6-2. The material state transition (solid, powder, and liquid) is incorporated within the model using the USDFLD subroutine described in Part I of this series [135].

6.3.2 HL Part Scale Model

A sequentially coupled part-scale thermo-mechanical model with 30 build layers is developed for comparison with experimental results. The part is 5 mm long, 1.2 mm tall, and 0.5 mm wide and is built

on a 4 mm thick substrate, as shown in Figure 6-3. A 0.04 mm thick powder layer corresponding to the experimental setup is applied during the simulation to mimic the printing process. The dashed blue line divides the printed part and the substrate in Figure 6-3. The substrate is constrained from moving in all directions while the part is printed.

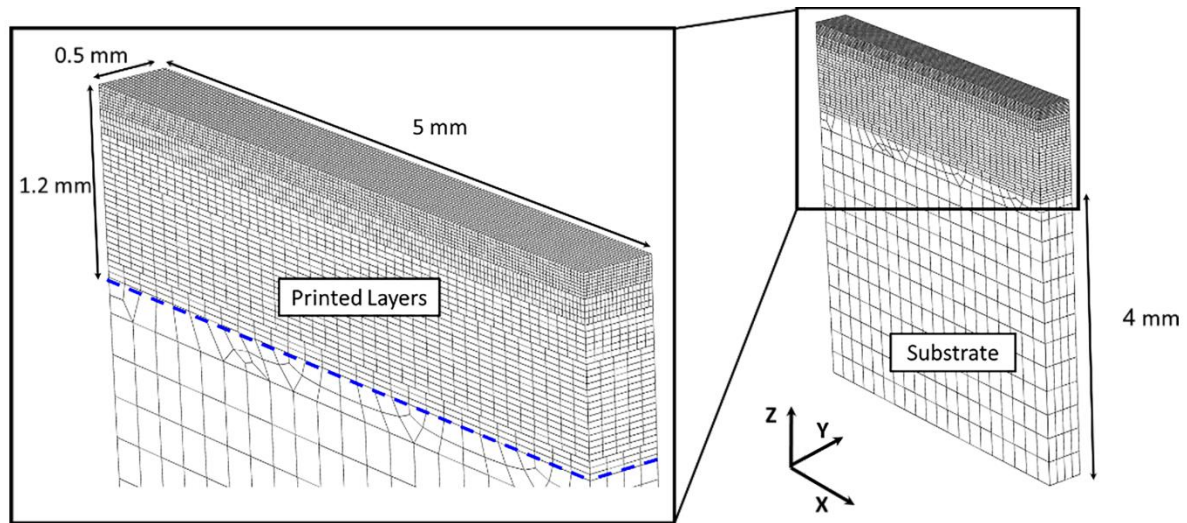


Figure 6-3: Part-scale meshed 30-layer model used to simulate the 12 different LPBF builds (3 powers and 4 scanning patterns shown in Figure 6-1). The dashed blue line shows the border between the printed layers and the substrate. The residual stresses are taken along the line shown in red.

Convective and radiative heat losses are defined for the free surfaces with the same coefficient values as the single-track model. The time between each layer addition is set to 10 s to reproduce the experimental settings for the recoater action. The simulation runs for 480 s after printing the last layer to allow the part to cool to room temperature. Following the build simulation, the boundary conditions are relaxed in the substrate to account for the stress relaxation when the part is removed from the printer.

The laser scan path is first generated within the Netfabb software and translated to a laser time-location database file using a custom Python script. The time-location file is then read by the UEXTERNALDB subroutine at the beginning of each increment in ABAQUS for the finite element simulation. The DFLUX subroutine uses this information to account for the position of the heat input during each time increment of the simulation.

A single τ value, representing the key control parameter for the HL model described in part I, cannot reproduce the different scanning patterns illustrated in Figure 6-1 due to differences in laser path lengths. As a baseline from Part I, a maximum τ value of 10 is selected for speed and accuracy. For shorter path lengths, experienced in the perpendicular pattern or in the corner of the 45° rotation patterns, smaller τ values are applied to match the path length.

An adaptive mesh-coarsening technique is implemented to reduce the model size as each new layer is added and allows the thermal and mechanical models to run nearly simultaneously. A custom framework developed by Achuthan and Jayanath [80] is implemented to coarsen the element size during simulation. The framework is incorporated with the element birth technique to simulate the layer deposition, and the phase transition is simulated with a user-defined subroutine. To facilitate the transfer of data from prior meshes, the stress strain data is transferred using the “mesh-to-mesh solution mapping” feature within Abaqus. A Python script is developed to map the displacement from prior meshes to the new mesh using interpolation with the “griddata” tool [80]. Linear interpolation is adequate to calculate the updated position of the nodes, as demonstrated in [80], [82]. A flowchart illustrating the computational framework is given in Figure 6-4.

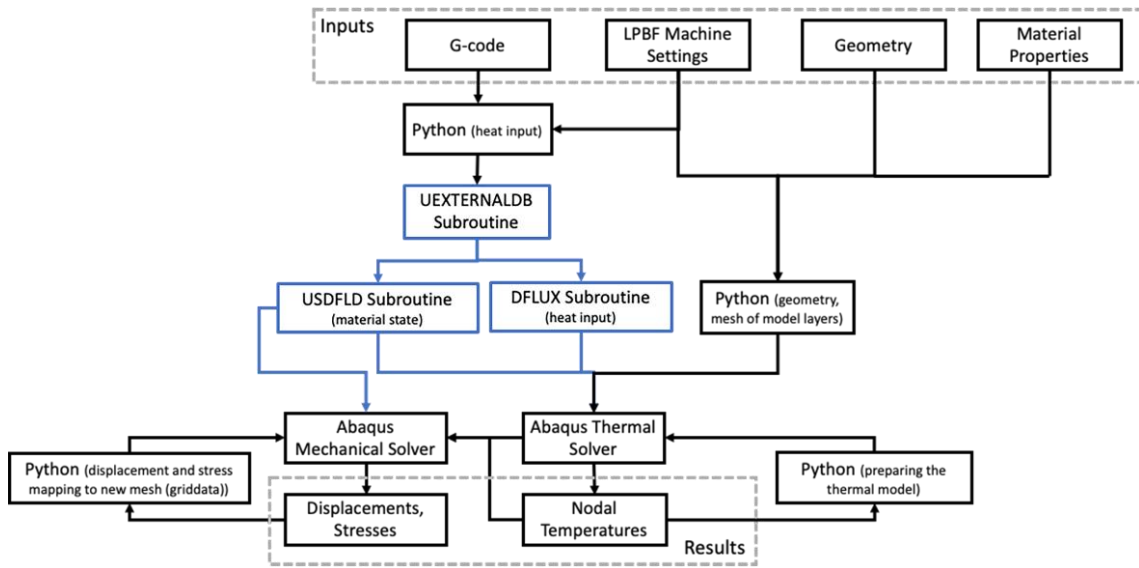


Figure 6-4: Flowchart of the computational framework including subroutines (blue) and interactions with customized Python programs.

Figure 6-5 shows the implementation of the framework to dynamically increase the element size during simulation. The build simulation begins with a single layer where the mesh is used to calculate the thermal results incorporated within the mechanical model. The nodal temperatures are used by the mechanical model to calculate the stresses and strains for each layer. Subsequent layers are meshed on top of the stack for further calculations using the results from the previous layers as initial conditions.

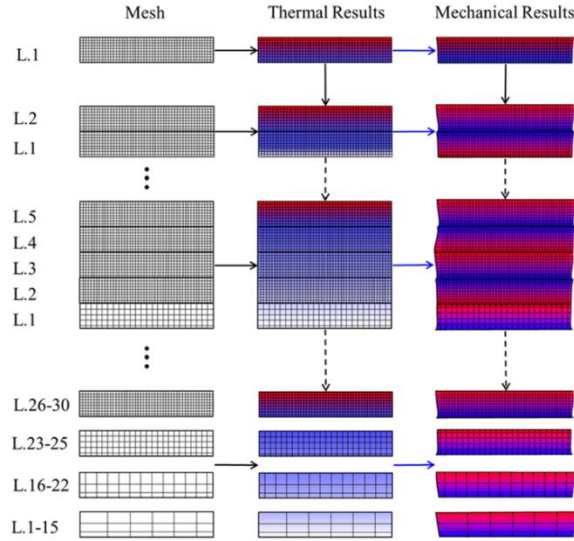


Figure 6-5: Mesh-coarsening algorithm showing mesh evolution with the number of layers. For each layer, a new model is created and the results from the previous model are mapped as initial conditions for the new model. A python code is used to transfer nodal displacements between models.

Table 6-2 indicates the mesh size changes as the number of layers is varied. This ensures high resolution close to the heat source and faster computation near the base plate. Figure 6-5 shows how mesh coarsening is implemented after 5 and 30 build layers. The mesh size of the first layer (L1 in Figure 6-5) is coarsened once the fifth layer (L5 in Figure 6-5) is deposited. As the build progresses, four different mesh sizes are incorporated, as detailed in Table 6-2. When the last layer is deposited, the layers L30 to L26 have the finest mesh size, while layers L1–L15 have the coarsest mesh size. The first 15 layers have 304 elements per layer and the last 5 layers have 4,175 elements per layer based on Table 6-2.

Table 6-2: Element size, in microns, for each meshed layer of the part-scale simulation.

Layer's number	Length (X)	Width (Y)	Height (Z)
1-15	132	62.5	40
16-22	90	55	40
23-25	36	30	40
26-30	30	20	20

6.4 Results and Discussion

6.4.1 Comparison Between HL and ED Single Track Models

The predicted residual stresses for the single-track model are examined to compare the HL and ED models. The results are evaluated 10 s (layer-wise cooling time) after the track is printed with the boundary conditions relaxed

6.4.1.1 Effect of Thermal Model on Stress Distribution

It was previously explained in Part I that the thermal distribution is crucial to accurately capture the stresses and strains generated during LPBF. This requires accurate prediction of nodal temperatures, cooling rates, and the heat transfer between the different material states (i.e., liquid, solid and powder states). The von Mises stress distributions are shown for the ED and HL models simulated with three different τ values in Figure 6-6. The stress is concentrated in the solidified regions (melted track and substrate). The powder bed has no stress (see the dark blue region in Figure 6-6) because it has negligible stiffness. Other researchers who have not considered the powder state have over-predicted stresses in the powder regions during LPBF [19]. This demonstrates the importance of considering the material state while simulating the LPBF process.

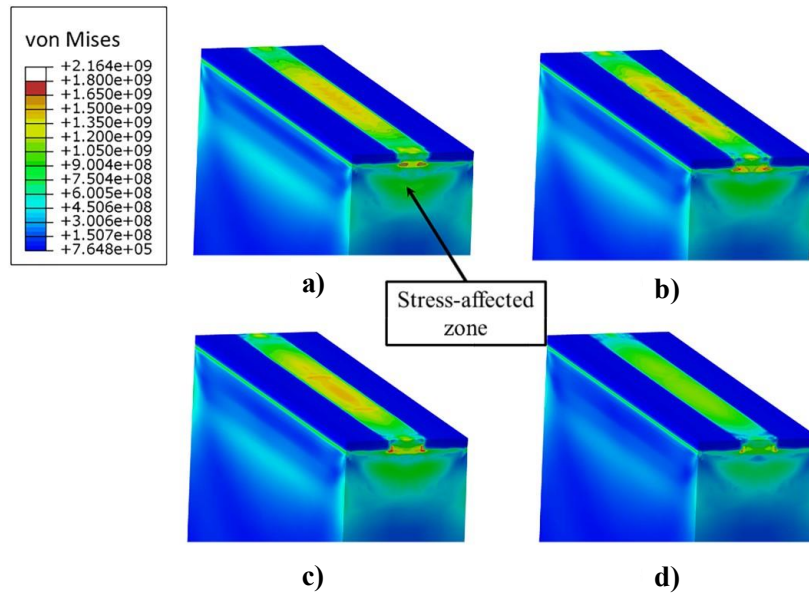


Figure 6-6: Von Mises stress (Pa) distributions for the a) ED and b) HL ($\tau = 5$), c) HL ($\tau = 10$), d) HL ($\tau = 20$) models after cooling (10 s) and relaxing the part constraints. The laser power is 200 W, and the speed is 1,000 mm/s for all four images.

The stress distributions are similar between HL $\tau = 5$ and the ED models. The stress-affected zones on the surface of the cross-sections have similar sizes and magnitudes. Both simulations have similar maximum stress amplitude situated at the center of the track. As τ increases, the stress-affected zone shrinks and the peak intensity decreases due to the heat source being integrated over a longer distance, resulting in reduced peak temperatures. This effect could be reduced by calibrating the HL coefficients for every τ value. The implemented heat transfer coefficients are calibrated in Part I [135] by minimizing the error for four τ values ($\tau = 5, 10, 15,$ and 20).

6.4.1.2 Effect of τ on Residual Stresses

The distribution of the residual stress components, along with the von Mises stress for ED and three different τ values in the HL model, are shown in Figure 6-7, Figure 6-8 for line 1 (longitudinal) and line 2 (transverse) in Figure 6-2, respectively. In general, the maximum stresses are observed at the center of the track, where the expansion and contraction of the material are the most constrained by surrounding material. The stresses decrease to nearly zero close to the edges where the solidified

material is free from constraints. The peak stresses are observed in the longitudinal direction (SXX in Figure 6-7, Figure 6-8). The stress magnitude is lowest in the build direction (SZZ) due to the free surface, consistent with previous LPBF single track simulations [143]. The primary contribution to the von Mises stress comes from the x-direction stress. Stresses are mostly tensile in the x- and z-directions, while they remain compressive in the y-direction. The negative peak stress values observed at the edges for the SYY and SXX in Figure 6-7 are due to edge effects.

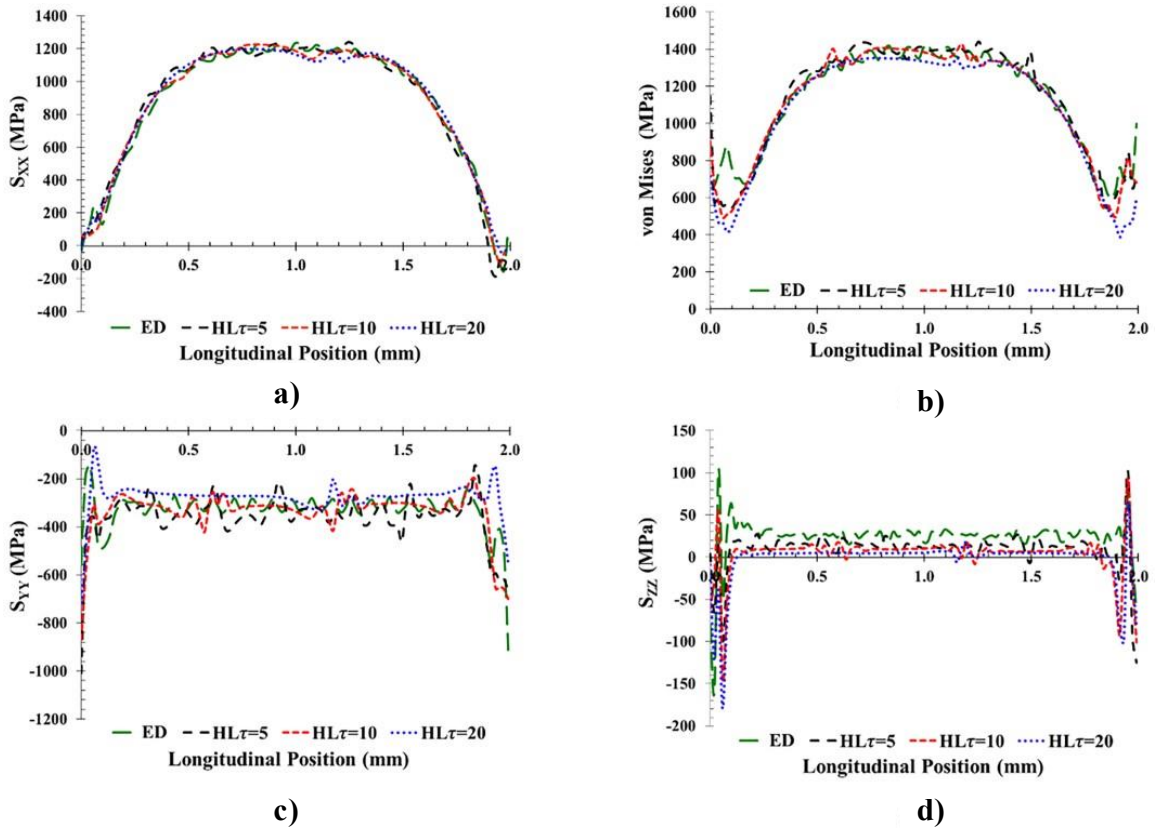


Figure 6-7: Single-track residual stress distributions along line 1 in Figure 6-2 for ED and HL models. a) von Mises b) SXX c) SYY d) SZZ stresses.

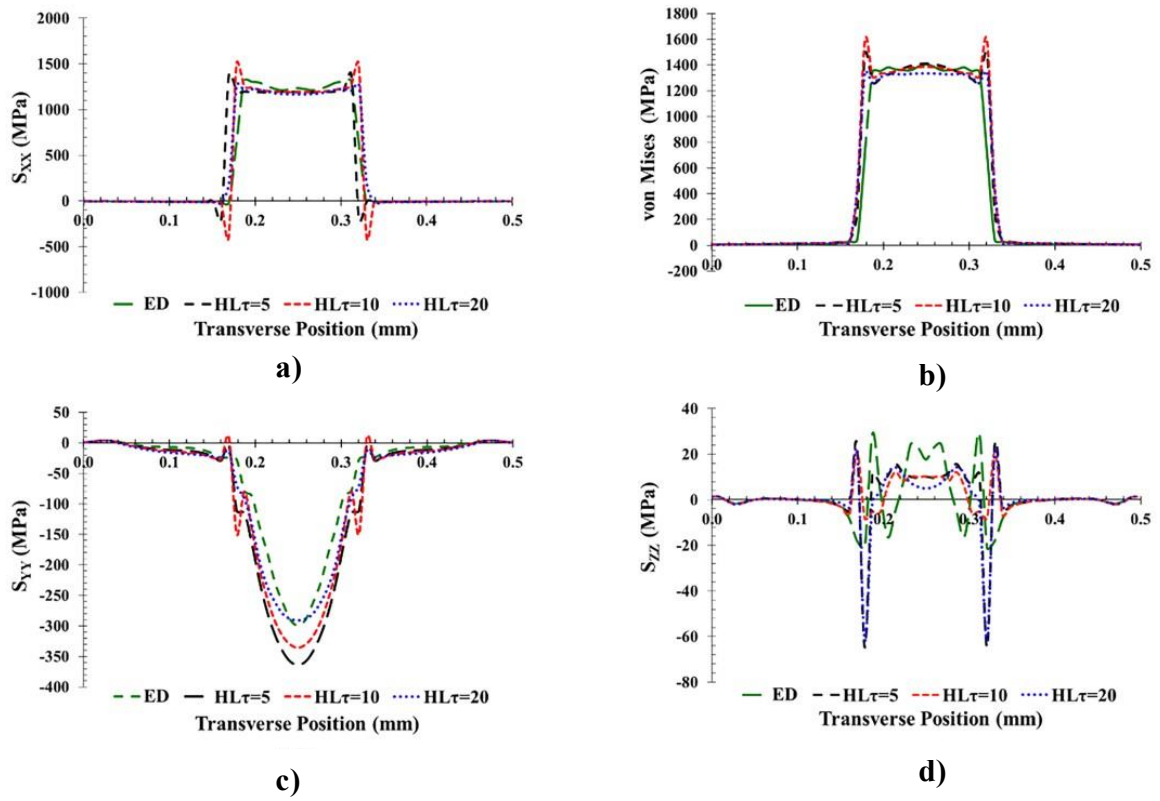


Figure 6-8: Single-track residual stress distributions along line 2 in Figure 6-2 for ED and HL models. a) von Mises b) SXX c) SYV d) SZZ stresses.

The HL model accurately reproduces the results of the ED model along the laser direction in Figure 6-7. The average variations between the ED and HL models are below 3% for all τ values in the SXX stresses. As the τ value increases, the stress oscillation is lengthened because the heat input is distributed over a longer region. This reduces the peak temperature as discussed in Part I [135]. Each stress oscillation represents one heat input step, and the larger the heat increment, the larger the variation in stress magnitude compared to the ED model. This is more noticeable in the y- (mean variation = 12%) and z- (mean variation 80%) directions when $\tau = 20$. Nevertheless, the y- and z-stresses have limited effect on the overall stress as shown by the accuracy in the von Mises stress (mean variation = 5%) distributions. Increasing the τ value has a similar effect on the variation of stress distribution calculated perpendicularly to the laser direction in Figure 6-8. On the contrary, the width

of the stress distribution decreases with increasing τ due to the difference in melt pool size described in Part I [135].

6.4.2 Model Computational Efficiency

The computational efficiency of the HL model in comparison to the ED beam scale models is attributed to two factors. Firstly, the time step increment size (τ) contributes to speeding up both the thermal and mechanical calculations by reducing the number of calculations in the track-scale model for the given laser paths. Secondly, the larger τ value enables use of a coarser mesh size, reducing the data size for mesh-to mesh mapping.

6.4.2.1 Effect of τ on the Computational Efficiency

Figure 6-9 shows the impact of τ on the computational efficiency of the mechanical model for the track-scale simulations using a consistent mesh. The HL model is over 6 times faster than the ED model when $\tau = 5$ and is over 30 times faster when $\tau = 20$. This shows that the time step increment has a bigger impact on the thermal model (1,500 times faster for $\tau = 20$ in [135]) compared to the mechanical model (30 times faster for $\tau = 20$), as the ED model requires more calculations for the thermal model. The time step increments thus have a smaller effect on the mechanical model. The total computational efficiency gain is the summation of the gain from the thermal and mechanical models for consistent meshes.

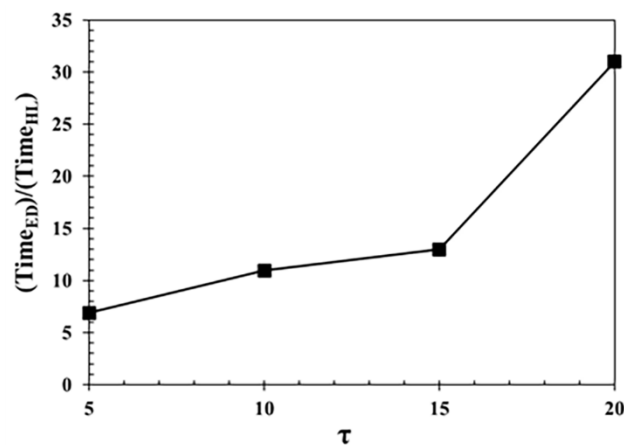


Figure 6-9: Comparison of $\frac{Time_{ED}}{Time_{HL}}$ as a function of τ for the single-track mechanical models.

6.4.2.2 Effect of Mesh Size on The Computational Efficacy

Element size is another important factor when considering the computational efficiency of the model. It is desirable to have a small mesh size in regions where the laser interacts with the powder bed to increase the resolution of the model. However, decreasing the element size decreases the time step. Therefore, it is desirable to use the maximum possible element size for part-scale simulations and motivates the use of dynamic remeshing.

Dynamic re-meshing is applied to the part-scale simulations as the printed layers are added. The ED model cannot be compared due to infeasible simulation time at the part scale. However, the estimated computational times for the ED model in addition to the HL model, with and without dynamic re-meshing, are compared in Table 6-3. The estimated times are calculated by comparing the processing times of the ED and HL single track models for the thermal and mechanical simulations. The ratio of computation time is multiplied by the HL part-scale simulation time to estimate the time required for the ED model applied at the part scale. Dynamic re-meshing decreases the thermal and mechanical models computational time by 3.3 times, allowing the thermal and mechanical models to be run in parallel. Since the mechanical model is 3.6 times slower than the thermal model, it controls the total run time.

Table 6-3: Computational time (hours) comparison between the ED beam-scale and HL ($\tau = 10$) part-scale models with and without the mesh coarsening technique.

		With mesh coarsening (hours)			Without mesh coarsening (hours)		
ED	Thermal Model (est.)	Mechanical Model (est.)	Total (est.)	Thermal Model (est.)	Mechanical Model (est.)	Total (est.)	
		11220	679	11898	37422	2266	39688
HL ($\tau = 10$)	Thermal Model	Mechanical Model	Total	Thermal Model	Mechanical Model	Total	
	17	62	62.5	56.7	207	264	

6.4.3 Part Scale Simulation of Residual Stresses

Twelve LPBF specimens with different laser processing conditions (3 different powers and 4 different scanning patterns shown in Figure 6-1 (a)) are produced to evaluate the accuracy of the HL model at the part scale. The residual stresses along the longitudinal direction (SXX) are measured at the center of the specimens as explained in Residual Stress Measurement. The simulated stresses (SXX) are also evaluated at the centers of the specimens and are compared with the experimental values in Figure 6-10. Specimen IDs are given along the abscissa where the first number refers to the laser power (180–220 W) and the second number represents the scanning pattern, following the naming convention in Figure 6-1. The experimental error bars for each specimen corresponds with the standard deviation in residual stress measurement.

For most LPBF conditions, the simulated stress falls within the measured standard deviation. The maximum and minimum variations between the experimental and simulated SXX stress components are 121 and 1 MPa, respectively. Most simulations overpredict the measured residual stresses. This is likely due to the stress relaxation associated with the metallographic preparation. The removal of materials has been shown in [11], [136] to relieve the residual stresses. The specimen 200 W-2 shows larger deviation compared to the simulation (268 MPa). It is unlikely that the measured residual stress varies between tension and compression. This error is attributed to the difficulty of aligning the X-ray beam over the small sample area (2.5 mm²). Acquiring residual stress measurements from multiple samples with the same printing conditions would provide additional statistical data and improve compatibility with the simulation results. Overall, the trends of increasing and decreasing the residual stresses with laser power and scanning patterns is well captured by the HL part-scale model.

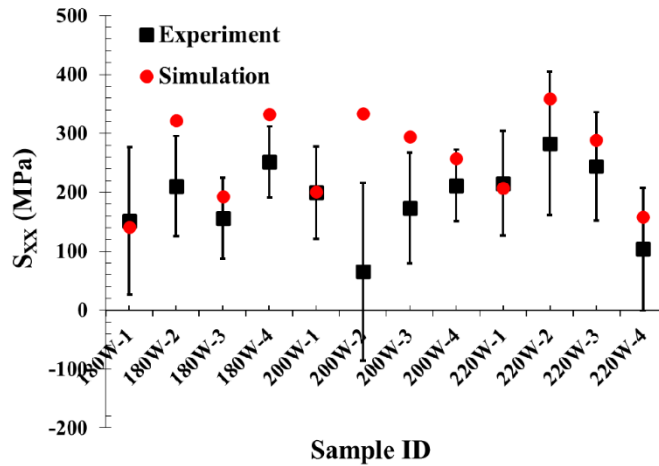


Figure 6-10: Comparison between the measured and predicted residual stresses in the x-direction (S_{xx}) evaluated at the center of the specimens. For each specimen ID, the first number refers to the laser power and the second number represents the scanning strategy given in Figure 6-1.

6.4.3.1 Effect Of Laser Power on Residual Stresses

Currently, there is no consensus on the effect of laser power on residual stress. Some researchers have shown that laser power has little effect on residual stress[144], while others have demonstrated both positive and negative correlation on residual stress [145]. In Part I of this series, it is shown that the laser power has a strong effect on the melt pool size but a limited effect on the cooling rate. Therefore, it is expected that the laser power will have a small impact on the simulated residual stresses.

The simulated residual stresses obtained with laser powers of 180 and 220W are shown in Figure 6-11. Only the perpendicular scanning patterns (see Figure 1) are shown here as the other scanning patterns exhibit similar results. The part-scale models are sectioned through the center to show the internal stresses. There is minute difference in the residual stress magnitudes and distributions for the different laser powers observed in Figure 6-11. It should be noted that the laser powers in these studies are limited to a small range. A larger laser power range could have a larger effect on the residual stresses.

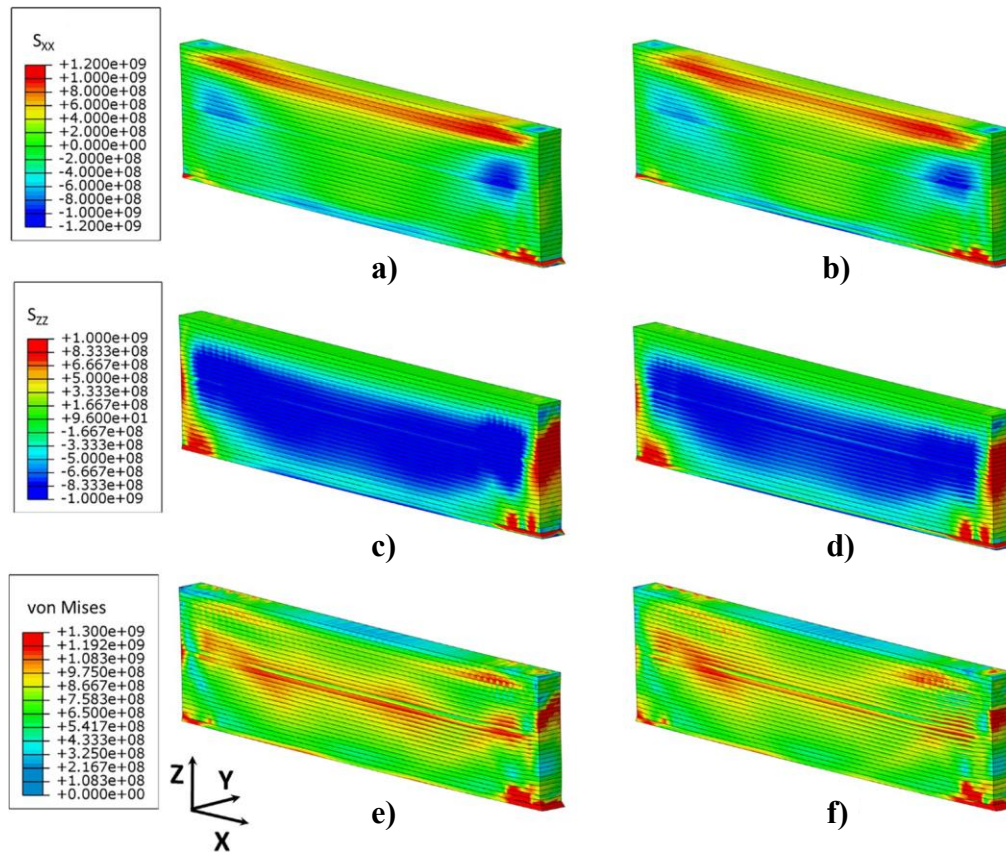


Figure 6-11: Residual stress (Pa) comparison between the three laser powers for the transverse scanning patterns in Figure 6-1. The residual stresses are shown along a centerline cross section of the part-scale simulations. Longitudinal stress (S_{xx}) for laser power a) 180 W and b) 220 W. Build direction stress (S_{zz}) for laser power c) 180 W and d) 220 W. Von Mises stress for laser power e) 180 W and f) 220 W.

The longitudinal stress component (S_{XX}) in Figure 6-11 (a)–(b) is highest close to the top of the build. However, the S_{ZZ} and the von Mises stress in Figure 6-11 (c)–(f) shows the largest stresses at the center of the part. The S_{ZZ} stress is near-zero at the top of the parts due to the free surface. The stress at the bottom of the part is reduced due to relaxation of the boundary conditions described in HL Part Scale Model. The S_{YY} stress is not presented because it does not change with laser scanning pattern and provides smaller contributions to the stress state. This is due to plate theory, which states that only limited load can be supported through the thickness direction in thin wall structures, as shown in[10].

Note that the inconsistency in the stress distribution around the center line is due to the mesh-to-mesh mapping, as shown in [82].

The distributions of the cooling rates (not shown here) are similar for the three laser powers considered in this study. The maximum in-process cooling rate is 5.3×10^6 K/s for 220W laser power and the cooling rate decreases to 4.3×10^6 K/s when the laser power is reduced to 180W. These cooling rates are consistent with values commonly reported for LPBF processing [125]. For such an infinitesimal variation in the cooling rate with laser power, the effect on residual stresses is expected to be minimal. This is consistent with Figure 6-11, which shows minimal effect of laser power on the residual stresses.

6.4.3.2 Effect Of Scanning Patterns on Residual Stresses

Laser printing patterns have been previously investigated by other researchers [132], [140], [146]. Generally, the scan strategy affects the final microstructure and part distortion more than the laser power [145]. Important parameters for investigating the effect of laser scanning strategy are the vector length (laser path length) and the laser path rotation angle between the layers. Kruth et al. [146] found that longer laser passes increase part distortion. Laser path rotation reduces the directionality of the residual stresses and creates a more homogenous quasi-isotropic stress state [132], [147]. However, these studies focused mainly on “island” scanning patterns for thick part components [53], [140]. To the authors knowledge, there have been no studies on the effect of scanning patterns on thin-wall structures.

This study focuses on thin-wall geometries where perpendicular and longitudinal scanning patterns have short and long vector lengths, respectively. Moreover, two rotation angles (90° and 45°) between the layers are investigated. The predicted residual stresses for the four different scanning strategies are shown in Figure 6-12, Figure 6-13, Figure 6-14 for the longitudinal (SXX), build (SZZ) and transverse (SYY) directions, respectively. For each case, limits are placed on the contour plots to eliminate numerical artifacts from stress concentrations at the edge of the parts or due to mesh-to-mesh mapping [82].

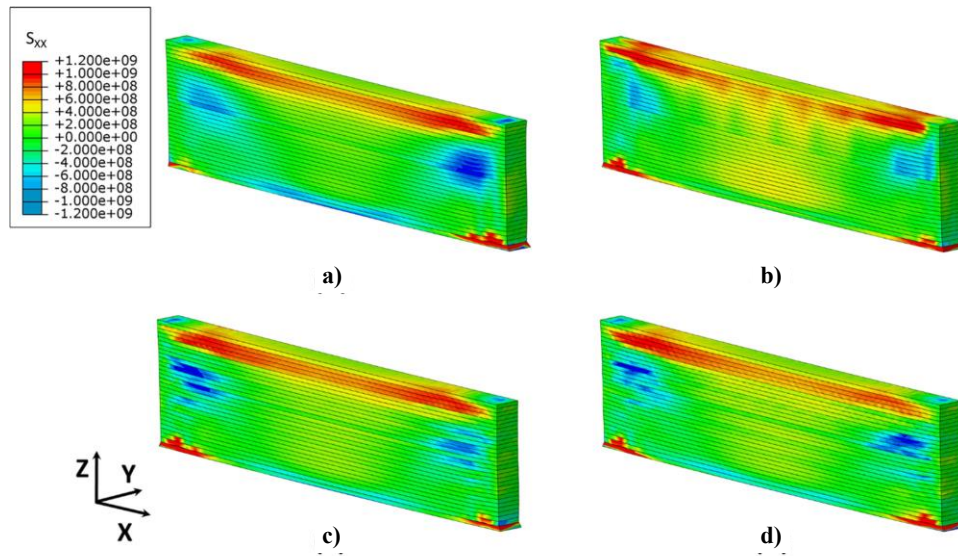


Figure 6-12: Longitudinal residual stress (S_{xx} (Pa)) comparison between the four scanning patterns described in Figure 6-1 a) Perpendicular, b) longitudinal, c) 90° rotation and d) 45° rotation. The residual stresses are shown along a centerline cross section of the part-scale simulations.

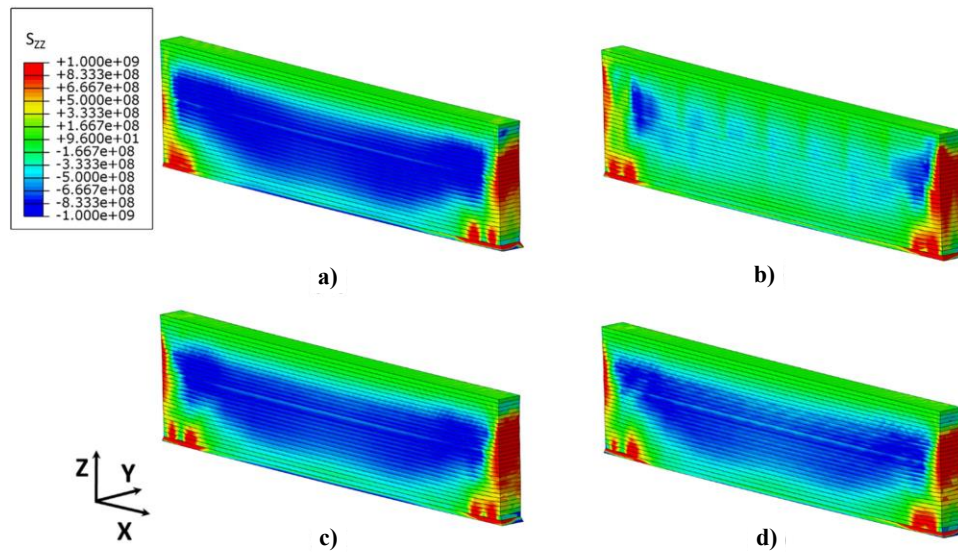


Figure 6-13: Build direction residual stress (S_{zz} (Pa)) comparison between the four scanning patterns described in Figure 6-1 a) Perpendicular, b) longitudinal, c) 90° rotation, and d) 45° rotation. The residual stresses are shown along a centerline cross section of the part-scale simulations.

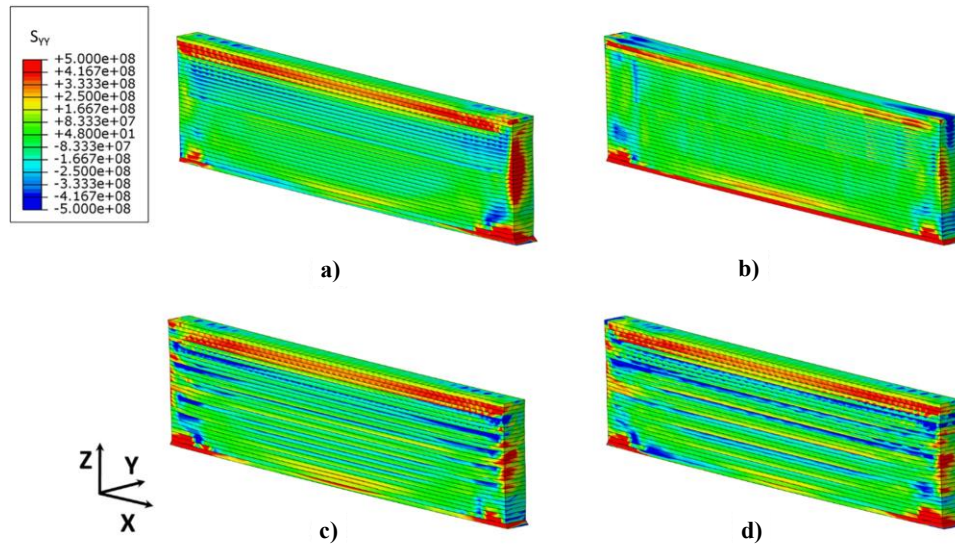


Figure 6-14: Transverse residual stress (S_{YY} (Pa)) comparison between the four scanning patterns described in Figure 6-1 a) Perpendicular, a) longitudinal, c) 90° rotation and d) 45° rotation. The residual stresses are shown along a centerline cross section of the part-scale simulations.

Maximum stresses are observed in the longitudinal direction (S_{xx}) for all scan strategies and have the same peak magnitude as the single-track simulations in Figure 6-7 a). In the single-track simulation, it is observed that the stress along the build direction (S_{ZZ}) is negligible. However, for the part-scale simulation, there is an accumulation of S_{ZZ} stress at the center of the part height. This indicates the importance of considering both build geometry and height to compare residual stresses in LPBF. The S_{YY} stress plots in Figure 6-14 shows layer-laminated structure for the 90° and 45° rotation patterns. This is due to the directional stresses and mismatches between the layers, resulting in a nonhomogenous stress distribution as discussed in (Kruth et al., 2012; Parry et al., 2016; Serrano-Munoz et al., 2021). The S_{YY} component is significantly lower (>2X lower than S_{xx}) than the other directions due to the thin wall builds, as explained in Effect of Laser Power on Residual Stresses.

There is increased residual stress along the laser travel direction. This is shown in Figure 6-12 (b), where the laser runs parallel to the part, and in Figure 6-14 (a), where the laser travels perpendicular to the part. The long vector length generates more tensile residual stress (average $S_{XX} = 505$ Mpa) along the part length (Figure 6-12 (b)), and the short vector length causes more residual stress (average S_{YY}

= 89.2 Mpa) in the through-thickness direction (Figure 6-14 (a)). The resulting residual stress is proportional to the path length, as seen by comparing the peak stresses in the perpendicular and longitudinal laser passes. Therefore, aligning the laser path with the thickness will reduce tensile residual stresses in thin-wall parts, as shown by comparing Figure 6-12 (a), (b).

The minimization of the tensile residual stress comes at the cost of increasing compressive residual stresses in the build direction, shown in Figure 6-13. The short vector length in Figure 6-13 (a) drastically increases the compressive residual stress in the build direction compared to the long vector length in Figure 6-13 (b). The difference is approximately 3 times higher for the short vector length. This increase in compressive residual stress will negatively impact the limiting build height in thin-wall components, as observed in [10].

The two rotation patterns shown in parts of Figure 6-12 (c), (d) Figure 6-13 (c), (d) Figure 6-14 (c), (d) have a layered quasi-isotropic residual stress distribution. This is consistent with previous studies showing more isotropic stress distribution when the laser path is rotated from layer to layer [147]. It is more apparent in Figure 6-12, Figure 6-14 where the longitudinal and transverse stresses are dominant due to the variation from layer to layer in the sectioned plane (z-x). The stress distribution for the rotation patterns is a combination of both perpendicular and longitudinal patterns, with the 45° rotation pattern exhibiting less variation between neighboring layers.

6.5 Conclusion

In the second part of this series, a new track-scale thermomechanical model is developed to predict the residual stress distribution during the LPBF process. The elasto-plastic properties of R65 are considered in the prediction of the residual stresses. The simulation results are first compared with a beam-scale (ED) simulation of a single laser track. There is good agreement between the track-scale (HL) and beam-scale models for residual stress prediction within 3 and 5% variation on the SXX and von Mises stresses.

The time step increment size of the mechanical model has a smaller effect on the computational time compared to the thermal model. The mechanical track-scale HL model is six times faster when $\tau = 5$ and 30 times faster when $\tau = 20$ relative to the beam-scale ED model. The dynamic mesh-coarsening

algorithm improves the computational time by a factor of 3.3 by reducing the time associated with solving each increment, allowing parallel computation of the thermal and mechanical solutions.

The accuracy of the HL model is also evaluated with part-scale specimens. X-ray diffractions are completed to measure the SXX stress components on specimens built with 3 different laser powers and 4 different scanning patterns. The measured stresses ranged between 282 and 65 MPa. The predicted stresses were within the standard deviation (average deviation of 54 MPa) of residual stresses for most cases. The simulation typically over-predicted the residual stresses due to the sample preparation procedure, however the trends match.

Laser powers between 180 and 220W have minimal effect, whereas the scanning pattern leads to more variation in residual stress distribution. While long vector lengths result in more tensile stresses along the longitudinal direction, short vector lengths cause less tensile stresses due to the part thickness. However, this leads to more compressive residual stresses in the build direction. Laser rotation patterns lead to a preferential combination of properties from both short and long vector lengths. This study shows that the model is capable of accurately predicting the residual stress variation due to laser parameters and scanning strategies at the part scale.

Chapter 7

Parametric Study on Interdependent Influences of The Laser Power and Printing Pattern on Residual Stress

In this chapter, the “Interdependent influences of the laser power and printing pattern on residual stresses in laser powder bed fusion additive manufacturing” is proposed. The results that were not presented on pervious chapter is used to evaluate the interdependent influence of the laser power and printing patterns. Two different laser powers and printing patterns are considered for this study the evaluation was conducted by simulation results. Furthermore, the details of required processing time for the developed mesh coarsening technique are presented. This evaluation emphases on required processing time to map the nodal displacement from the old mesh to the new one³.

³ The chapter presents an accepted manuscript of a conference paper published in 9th International Conference on Mechanics and Materials in Design
Proceedings M2D2021: 9th International Conference on Mechanics and Materials in Design.

7.1 Introduction

Laser powder bed fusion (LPBF) is an additive manufacturing process where a laser is used to locally consolidate powder into a desired geometry [10], [135], [148]. The LPBF process is of interest for high gamma prime nickel-based superalloy materials, which are good candidates for high-temperature environments in aerospace applications. However, there are many challenges during the building process due to the complex material-process relationship which need to be accounted for to successfully apply LPBF to superalloys [103], [104], [126], [127]. An optimum combination of laser scanning parameters, such as laser power, hatch spacing, and printing pattern, is required to construct high-quality near net shape parts. Each parameter can have direct or indirect effects, depending on the strength of the inter-parametric influences, on the final part quality [145]. A finite element (FE) model can be used to determine a set of laser parameters to reduce the number of defects and experimental iterations required for part design and fabrication [135], [149]. Cheng and Chou [53] discussed the interdependent influences of different printing parameters using simulations. In their evaluation, it was reported that higher laser power and lower scan speed increases the melt pool size. This necessitates using larger island scan sizes to obtain a stable melt pool size. A beam-scale model was used to simulate the process for a few tracks, which limited the analysis to a single layer [53]. Simulations of larger components require the development of larger heat input models to reduce the number of elements and solution increments [19]. Tangestani et. al [135], [148] performed process simulations to capture the thermal and mechanical results for a few layers. The model was developed using a line heat input model and mesh coarsening technique to improve computational efficiency. This approach is beneficial to evaluate the effect of laser power and printing pattern on residual stresses. While the direct impact of each parameter was reported, the inter-dependent influences of each parameter were not considered. In other words, increasing the value of one parameter could affect the contribution of another parameter to the residual stresses.

In this study, the LPBF process was simulated to evaluate the direct and interdependent influences of the laser power and printing pattern on residual stresses. A line heat input model and mesh-coarsening technique were used to achieve a feasible computational time. The printing parameters include two different laser powers and scan patterns, allowing the comparison of four different parametric combinations.

7.2 Model Description

The finite element software, Abaqus, was used to simulate the process for a 30-layer part made of high gamma superalloy RENÉ 65 (R65). The part domain is $5 \times 0.5 \times 1.2$ mm (length \times width \times depth) prism printed on a $5 \times 0.5 \times 4$ mm substrate as shown in Figure 7-1 (a). A series of two different laser powers and printing patterns are studied. The two laser powers are 180 W and 220 W, and the two printing patterns, at 90° and 45° rotation angles, are demonstrated in Figure 7-1 (b). Similar material properties as reported in Tangestani et al. [135], [148] were used in this study.

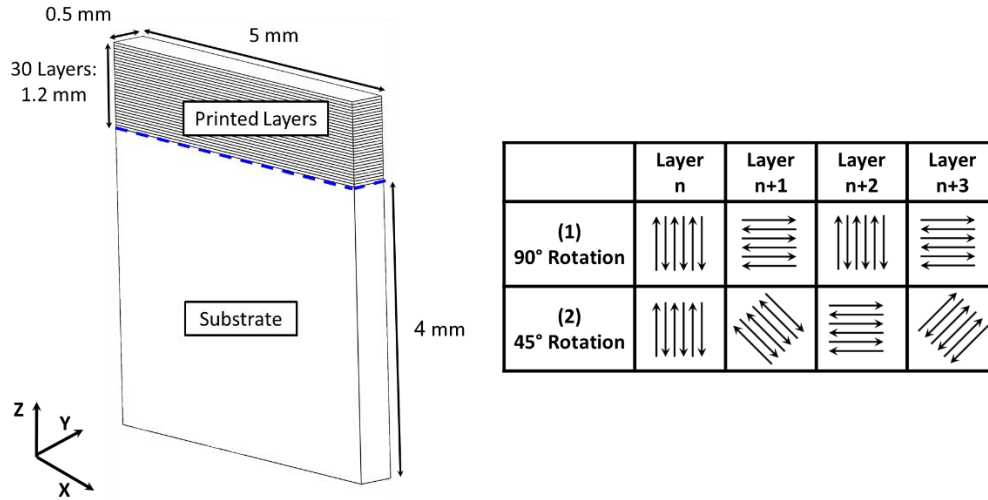


Figure 7-1: a) The 30-layer part was used to simulate the LPBF builds. The dashed blue line shows the border between the printed layers and the substrate. b) Two different printing patterns (90° and 45° rotation angles) were used to study the interdependent influences of laser power and printing pattern.

The parts were printed with a laser speed of 1000 mm/s, layer thickness of $40 \mu\text{m}$, beam radius of $60 \mu\text{m}$ and hatch spacing of $90 \mu\text{m}$. The cooling time between each layer scan is 10 s, and the simulation runs for 480 seconds after the last layer is printed to allow the part to cool down to room temperature (25°C). Following the process simulation, the boundary conditions are relaxed in the substrate to account for the stress relaxation when the part is removed from the printer. The convection and radiation heat losses were applied to all open surfaces with coefficients of $20 \left(\frac{W}{m^2 \cdot ^\circ\text{C}}\right)$ and 0.4, respectively. To reduce the number of necessary increments for the model a Hybrid Line (HL) heat input model is utilized as follows (Tangestani, Sabiston, Chakraborty, Yuan, et al. 2021):

$$\bar{Q} = C \frac{P\eta}{\sqrt{2\pi}\Delta t v_s H r_l} e^{\left(-\left|\frac{z}{H}\right| - 2\left(\frac{y}{r_l}\right)^2\right)} \left(\operatorname{erf}\left(\frac{\sqrt{2}(x_{end} - x)}{r_l}\right) - \operatorname{erf}\left(\frac{\sqrt{2}(x_{start} - x)}{r_l}\right) \right) \quad (7-1)$$

Where P is laser power, r_l is beam radius, and local coordinate are shown by x , y , and z . The function erf is the error function, and the heat input model start and end points are x_{start} and x_{end} . The end points for a heat input increment are defined by the laser speed (v_s) and time increment (Δt). The parameter η is the absorption factor obtained from [105] and the C is the calibration coefficient which is 1.2 as studied in Tangestani et al. [135].

A mesh-coarsening technique is used to reduce computation time and improve efficiency while maintaining model [135]. The framework interrupts the simulation after printing each layer and increases the element size according to the distance from the top (printed) layer then executes the new model with the larger mesh [135]. This method involves mapping the solution from the old model to the new one with the larger mesh size. Using the "`*MAP SOLUTION`" keyword in Abaqus, the mechanical results such as stresses and plastic strain, except for deformation, are transferred. To replicate the mapping process for deformation the algorithm shown in Figure 7-2 is developed. The first step is to generate the `*.INP` and `*.RPT` files using Abaqus CAE and the `*.ODB` file. Following this, they are used to extract mesh coordinates (for both the fine element and new coarse element models) and deformations. The extracted portions of each file are shown inside the blue rectangles (see Figure 7-2).

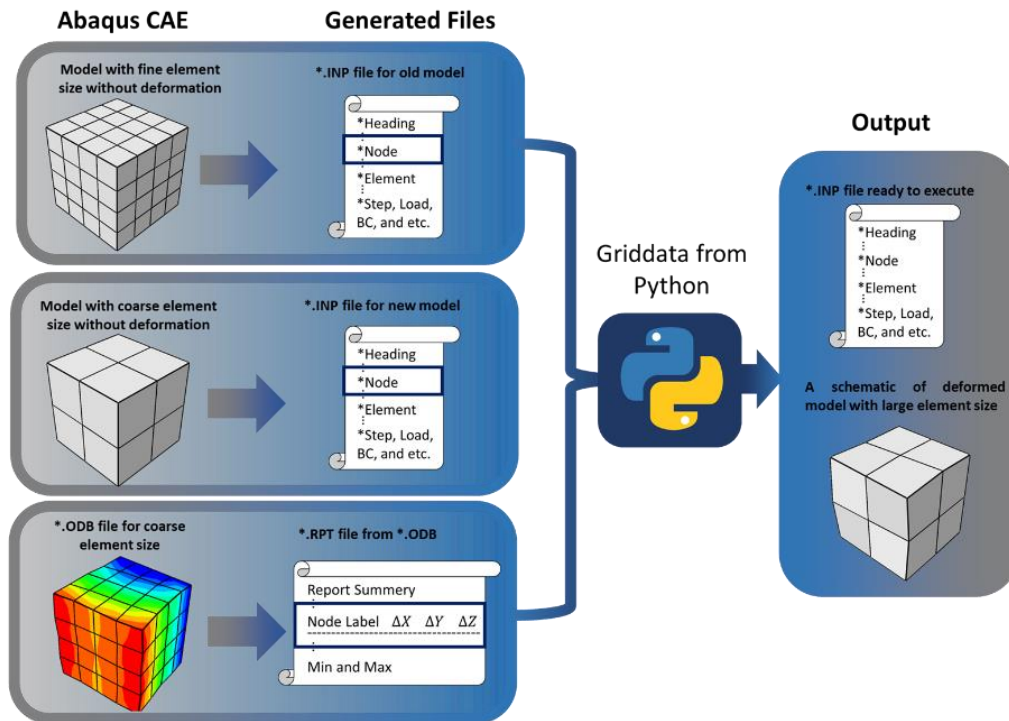


Figure 7-2: The algorithm for preparing and mapping the deformation to an updated model with coarser elements. Blue rectangles indicate the extracted section from each file

With this information and utilizing the griddata tool in Python, the nodes (in the updated model) are repositioned to reflect the deformation from the old model. Ultimately, this data is written to a new file in the *.INP format, which is compatible with the Abaqus solver. The remaining details such as increasing rates between the simulated layers are maintained from the previous study [135].

7.3 Results and Discussion

7.3.1 Computational Time

The model is capable of predicting the residual stress within a feasible processing time. The simulation was conducted on dual CPU Xeon Gold 6240 @ 2.6GHz. The thermal and mechanical models are processed in 17 hours and 62 hours, respectively. The two models are being processed in parallel, which limits the total processing time to the time it takes to process the mechanical model and the first thermal layer, which is nearly 63 hours. It has been shown in the literature that mesh coarsening could reduce

computation time by 30% compared with conventional approaches. The main limiting factor is the time required to pre-process each layer's results and map them to the new model. Pre-processing involves Python mapping for deformation and Abaqus mapping for the rest of the solutions (such as stress, temperature, etc.). Abaqus's mapping relies only on the total number of elements and increments, which is not of interest for this study. Python processing time can take between 5 and 15 minutes, depending on the number of elements in layers. Figure 6-3(a), shows the time required by Python to read, prepare, and write the *.INP file for the Abaqus solver. According to the plot, there is a minimum amount of time required for processing and there is a linear connection between elements and processing time. Figure 6-3 (b) shows the time needed for Python to relocate the nodes within one layer using the griddata tool. To change the mesh for the whole model, this process is repeated for every simulated layer and the substrate. Contrary to the first plot, the number of elements dramatically lengthens the processing, indicating the importance of mesh density.

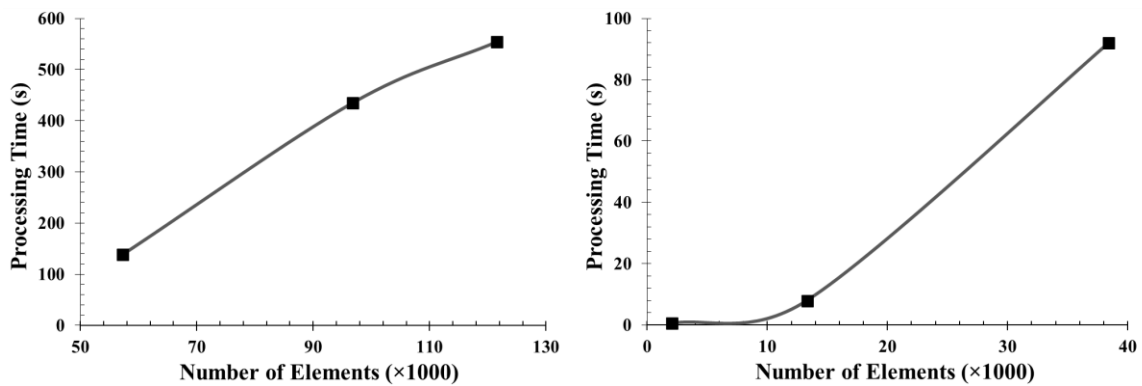


Figure 7-3: a) The required time to read, prepare, and write the *.INP file. b) The processing time to map the deformation using griddata tool for each layer with respect to the number of elements in the fine layer

By splitting the model into more sections, the preprocessing time increases, however the time required to solve each section is shorter. Furthermore, to maintain the model's accuracy, element sizes need to be increased gradually. For further reduction in computational time, a parametric study on mesh size dependence is recommended.

7.3.2 Interdependent Influences of the Laser Power and Printing Pattern

Figure 7-4 shows the von Mises stresses in the cross-sectioned parts for different laser powers and printing patterns. The von Mises stress is higher on the surface compared to the center of the part due to higher tensile stress in the longitudinal direction as reported in Tangestani et al. [135], [148]. This negatively impacts the final part quality as the longitudinal tensile stresses at the surface increase the part's susceptibility to fatigue failure. The stress magnitude is lower close to the top of the print as the normal stress is near zero in the last layers. The substrate constrains the part from moving in all directions, hence reducing the stress in the lower layers. The direct effect of printing patterns on the residual stresses is stronger than that of laser power, which agrees well with a previous study [148]. As reported by Tangestani et al., the longitudinal and normal stresses, controlled by the laser printing pattern, play a major role in the resultant von Mises stresses [10], [148]. Accordingly, the rotation angle helps homogenize the residual stresses created within the part [146]. While both laser power and printing pattern have direct impacts on the generated residual stresses [140], they have interdependent influences as well. For instance, for a constant laser power of 180 W (Figure 7-4 (a) and c)), changing the printing pattern from 90° (Figure 7-4 (a)) to 45° (Figure 7-4 (c)) does not directly affect the residual stresses. However, as the laser power is increased to 220 W (Figure 7-4 (b) and d)), the effect of printing pattern on the residual stresses is more pronounced, as shown in Figure 7-4 (b) (90°) and (d) (45°). This is highlighted by comparing the residual stress distributions for the 90° (Figure 7-4 (b)) and 45° (Figure 7-4 (d)) cases (black circles) For the 90° case, the residual stresses are more inhomogeneous compared to the 45° case. Therefore, increasing the laser power leads to more induced energy through the printed layers and enhances the effect of printing pattern on residual stress.

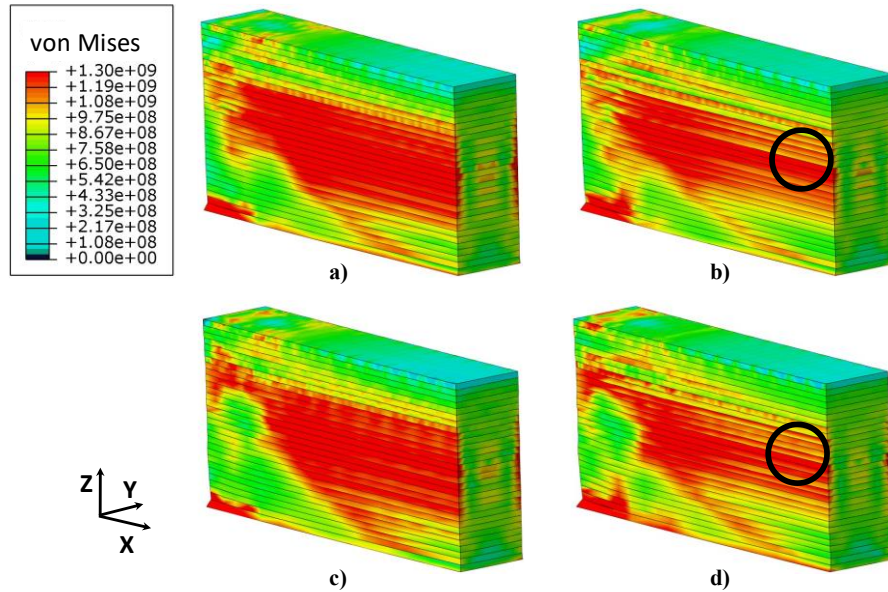


Figure 7-4: The residual stress following the completion of simulation. The parts are sectioned at the center along the X-direction and the laser powers and rotation angles used are a) 180W-90°, b) 220W-45°, c) 180W-90°, d) 220W-45°, respectively. The black circles highlight the regions demonstrating the effect of printing patterns on residual stress magnitude.

7.4 Conclusion

In this study, the interdependent influences of the printing pattern and laser power on residual stresses were examined using finite element simulation. It is demonstrated that the interdependent effect is higher compared to the direct effect of laser power on residual stresses. Increasing the laser power induces more energy through the printed layers and enhances the influence of printing patterns on residual stresses. Thus, it is proposed that the selection of optimum printing patterns is more significant with higher laser power.

Chapter 8

Developing Lumped HL Model to Simulate the Laser Powder Bed Fusion Process for Large Scale Components

The previously developed model is improved in this chapter in order to reduce the computational time. Several part-scale techniques are applied to the mesoscale model, and the framework is improved so that it can execute multiple simulations. A DOE was created with 33 components to examine simulation accuracy and analyze how part geometry and printing pattern affect LBH. Following this, the created residual stress calculated from the simulation is evaluated to determine the relationship between part failure and microcracking. Additionally, buckling simulation was conducted to determine the part's susceptibility to buckling. Based on the results, the thickness of the part has the greatest impact on residual stress and therefore should be considered when designing the manufacturing process.⁴

⁴ This chapter presents a manuscript of an article being prepared for journal submission.

8.1 Introduction

Superalloys are excellent materials for application in aerospace and power industries due to superior mechanical properties at elevated temperatures [104], [126], [127], [150], [151]. Turbine blades and fuel nozzles are examples of complex structures commonly used in these industries [102], [152]. Additive manufacturing processes such as binder jet [153]–[155] and laser powder bed fusion (LPBF) [20] offer near-net-shape construction of such features. The LPBF technology offers several advantages such as high density [156], good mechanical strength [157], and high dimensional accuracy [98]. However, build defects such as surface roughness[158], micro-cracking[149], and part distortion [10], [159] diminish the final part quality.

Internal micro-cracking and in-process part failure are especially important for thin-wall part processability due to the steep temperature gradients and high thermally-induced stresses inherent to the LPBF process [147]. Micro-cracking is strongly dependent on the processing strategies [160] and wall thickness [10]. According to Carter et al. [119], high laser powers and scan speeds result in high micro-cracking propensities. Chakraborty et al.[10] showed that internal micro-cracking does not cause thin-wall part failure. According to the authors, distortion plays a major role in part failure and limits LPBF processability. The limiting build height (LBH) phenomenon was introduced to describe the process limitation with respect to thin-wall part construction [10]. The LBH is defined as the maximum achievable part height, affected by the residual stress, distortion, and buckling. The created residual stresses are especially important for thin-wall part failure as they cause buckling and excessive part deformation, suppressing layer deposition during processing. The residual stress is affected by the printing pattern, part geometry, phase transformation, and material properties[42]. In order to minimize costs, the finite element method (FEM) is used to calculate the thermal histories and resulting mechanical behaviour (such as stress and strain) during the manufacturing process.

Many researchers suggest the layer (flash) heating technique for part-scale simulation and residual stress prediction [15], [92]. This approach uses uniform heat application over the layer, with one or more layers simulated in each step. Layer heating eliminates the effect of printing pattern on stress directionality, essential to study the buckling phenomenon. To resolve the induced stress anisotropy, the laser movement must be modelled at the laser beam scale [53]. However, LPBF process simulation using the beam-scale heat input could take thousands of hours (due to the significant size difference

between the beam and the part) and is not practical for large-scale simulations [7]. To enhance the simulation time, it is common practice to use the line heat input model [19]. Tangestani et. al. [135] used the line heating approach to simulate the LPBF process for a thin-wall part. The authors developed a hybrid line (HL) heat input model with the exponential decaying (ED) heat source. Thin-wall components, with identical sizes of $5 \times 1.2 \times 0.5$ mm (length \times height \times thickness), were simulated within 63 hours using the hybrid line (HL) heat input model. However, the model size was too small to simulate the actual in-process part failure.

To achieve feasible processing time and accelerate computation, the lumped modelling approach, combining the heat input and layers, is widely used [134]. Bayat et. al. [161] conducted a parametric study on the impact of the number of lumped tracks and layers on model resolution. The model simulated tracks with a single increment neglecting the effect of laser movement along the laser track. A HL model study conducted by Tangestani et al. [148] showed the importance of laser track segmentation on the simulation of anisotropic stress distribution in thin-wall parts. Accordingly, in this study, a new model is developed by applying the lumping approach to the HL model. This allows improved computational efficiency and prediction of the stress directionality generated by the laser tracks. Furthermore, the lumped modelling and layer heating methods are combined to offer versatility.

The new model is used to understand how the scanning strategy and thin-wall part geometry contribute to the in-process part failure observed previously in high gamma-prime (γ') Ni-based superalloys [10]. A large design of experiment (DOE), consisting of thirty-four parts with five different lengths and eight different printing patterns with and without inter-layer scan rotations, is investigated through experiments and finite element simulations. The simulated results are compared with experimental measurements to determine the accuracy of the model for LBH prediction. The predicted residual stresses are used to evaluate the effect of the part geometry and printing patterns on the LBH phenomenon. The findings are beneficial to obtain optimal processing conditions for printing thin-wall parts using LPBF.

8.2 Material and Experimental Methods

8.2.1 Feed Stock Material

The high- γ' Ni-based superalloy RENÉ 108 (R108) powder was used as feedstock for the LPBF process. The powder was gas-atomized by Powder Alloy Corporation (PAC). The majority of the powder consisted of spherical particles with the average size of 19 μm (D50) and a size distribution of 12-40 μm (D10-D90). The chemical composition was 8.64 Cr, 10 Co, 10.03 W, 0.53 Mo, 0.75 Ti, 5.36 Al, 0.87 Hf, 0.01 Zr, 0.01 C, 3.02 Ta, 0.01 B and balance Ni (all in wt. %). The alloy contained 6.11 wt% Al + Ti and γ' volume fraction of 63% [162], identified as a hard-to-weld material in literature [160], [163]. This implies that the material poses challenges for 3D printing applications due to in-process failures and microcracks in the as-built parts.

8.2.2 LPBF Procedure

An Aconity MIDI LPBF machine was used to print 34 thin-wall parts under an argon environment. The laser speed was set to 1000 mm/s, power 200 W, layer thickness 40 μm , laser radius 60 μm , and hatch spacing 90 μm . These process parameters were identical for all the fabricated parts. Figure 8-1 shows an overview of the design of experiment (DOE) and orientation of the printed parts with respect to the build plate. The components were placed at an angle of 75 degrees with respect to the recoater travel direction, as shown in Figure 8-1 (a). The distances between individual and groups of parts were set to 5 mm and 10 mm, respectively. All parts were set to 0.5 mm thickness and 30 mm height, as shown in Figure 8-1 (b).

The DOE was constructed to evaluate the influence of part length and scanning strategy on the LBH and part distortion. Four different part lengths (30 mm, 40 mm, 50 mm, and 60 mm) were studied, as illustrated with different colors in Figure 8-1 (b). Each part is labeled (1, 2, 3, 4, 5, etc..) according to its printing pattern. Table 8-1 lists the vector and rotation angles for 8 different printing patterns investigated here. A schematic showing the printing pattern and vector angle on a part layer is presented in Figure 2. Printing patterns include scans with or without rotation between successive layers and cover a wide range of track lengths (vector lengths). For example, a scan angle of 90° generates a scanning pattern with the shortest vector length, defined as extra short (“ES”), while a scan angle of 0° creates a scanning pattern with the longest track length, defined as extra long (“EL”). Intermediate angles of 15°

and 75° refer to short (“S”) and long (“L”), respectively. A 90° scan rotation between layers for the “ES” or “EL” printing patterns generates alternating shortest and the longest vector lengths, called extra long - extra short (“EL-ES”). A 150° scan rotation between layers for the “S” or “L” printing patterns generates unchanged vector lengths represented as short-short (“S-S”) and long-long (“L-L”), respectively. A 67° continuous scan rotation between layers, defined as the random (“R”) printing pattern, produces varying vector lengths in subsequent layers along the part height. The type and magnitude of the residual stresses are highly dependent on the vector angle, vector length [148] and part dimensions [164].

For model validation purposes, two additional components with identical dimensions of $10 \times 20 \times 1$ mm (length \times height \times thickness) were fabricated using the extra-long (“EL”) and extra-short (“ES”) printing patterns. These printing patterns showed the largest stress discrepancy in a previous study [148]. Tracks in the “EL” printing patterns include vector lengths equal to the part length (0° scan angle), while tracks in the “ES” printing pattern consist of vector lengths equal to the part thickness (90° scan angle). The part thickness was maximized to achieve the design height and to enable measurements of the deformed shape using a 3D scanner.

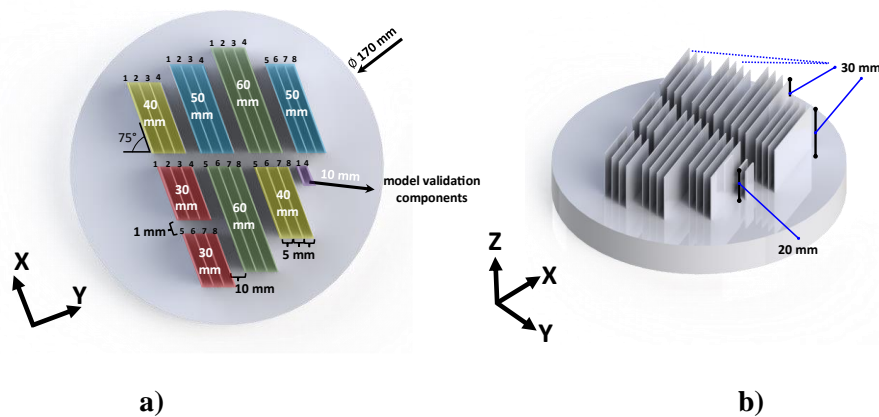


Figure 8-1: The DOE and configuration of the thin-wall components on the build plate shown in a) top 2D view and b) 3D view. All components, except the two used for validation, have identical thicknesses and heights, but varying lengths and printing patterns. Parts with identical lengths are grouped and

labelled using color codes. Annotations are added to describe printing patterns (1, 2, 3, etc.,) detailed in **Table 8-1**.

Table 8-1: The printing patterns used to manufacture the thin-wall components. The scan angles for the first 5+n layers are included under the column group labelled track angle. Each printing pattern corresponds to the label presented under the "Named as" column. The following nomenclature system is used: "EL" – extra-long; "L" – long; "S" – short; "ES" – extra-short; "EL-ES" – extra-long-extra-short; "L-L" – long-long; "S-S" – short-short; and R – random. "EL", "L", "S" and "ES" represent printing patterns without inter-layer rotations, while "El-ES", "L-L", "S-S" and "R" represent printing patterns with scan rotations between layers.

Printing Pattern Label	Named as	Track Angle (°)					
		1	2	3	4	5	n
1	ES	90	90	90	90	90	90
2	S	75	75	75	75	75	75
3	L	15	15	15	15	15	15
4	EL	0	0	0	0	0	0
5	EL-ES	90	0	90	0	90	0,90
6	S-S	75	115	75	115	75	75,115
7	L-L	15	165	15	165	15	15,165
8	R	67	134	201	268	335	R67

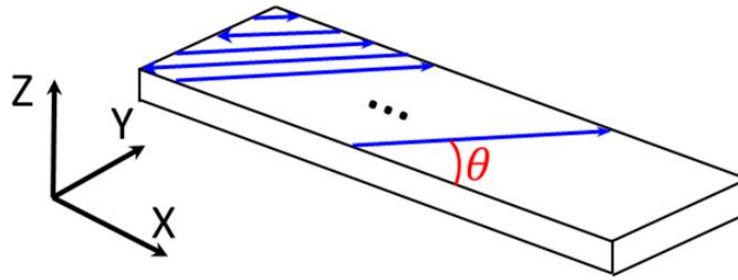


Figure 8-2: Schematic of the track angle and printing pattern rotation. Small scanning angles result in long vector lengths and large vector angles produce short vector lengths. For example, a track angle (θ) of 90° corresponds to a vector length aligned with the part thickness.

8.2.3 Evaluating the Printed Part Deformations

Accurate measurement of residual stresses in the additively manufactured component is costly and time-consuming [122]. To solve this challenge, the part distortion level is commonly used to predict the residual stresses. Accordingly, in this study, the model was validated by the measurement of part distortion using a 3D scanner. Thicker components (1 mm) were added to the DOE for model validation because the 3D scanner cannot accurately measure the shape of the thin-wall parts. The printed parts were extracted from the build plate using wire electrical discharge machining (EDM). The build plate was kept noticeably larger than the printed parts to prevent part distortion during removal. A SmartScan 3D scanner provided by AICON was used to measure the part deformation. The scanner is capable of measuring deformations with a precision of $10\ \mu\text{m}$ with its S - 150 mm lens (Hexagon, n.d.). The final 3D geometry was constructed by merging 30 individual scans taken with a 12° increment. To verify the simulation results, the measured and predicted distortions were compared.

8.2.4 Limiting Build Height Measurement

In this work, the limiting build height (LBH) is defined as the distance from the top surface of the build plate to the highest point of the as-built components. The LBH represents the first sign of partial or complete failure, as demonstrated in Figure 8-3. Partial LBH failure is considered for components showing preliminary signs of part failure, as shown in Figure 8-3 (a). Complete LBH failure is

considered for parts with clean failure at the summit, as shown in Figure 8-3 (b). All LBH measurements were conducted using a digital caliper.



Figure 8-3:LBH measurement criteria for a) partial and b) complete part failure. The red lines indicate the end positions of the LBH measurements.

8.3 Modeling

Dassault System's finite element software, Abaqus, was used to model the LPBF process. A description of the AM model, including its ability to predict stress and deformation during and after the process, is provided in this section. The in-process results provide insights into the contribution of part geometry and printing pattern to the final part distortion and LBH.

8.3.1 Simulation of LPBF Process

Firstly, a thermal model was developed to calculate the nodal temperature using the traditional heat transfer equation:

$$\rho C_p \frac{\partial T}{\partial t} = \frac{\partial}{\partial x} \left(k \frac{\partial T}{\partial x} \right) + \frac{\partial}{\partial y} \left(k \frac{\partial T}{\partial y} \right) + \frac{\partial}{\partial z} \left(k \frac{\partial T}{\partial z} \right) + Q_v, \quad (8-1)$$

Where, ρ is density, C_p is specific heat capacity, T is nodal temperature, k is material conduction, and Q_v is laser heat input. The heat loss from the open surfaces is simulated for conductive, convection and radiative heat transfer as follows:

$$k \frac{\partial T}{\partial x} = h(T - T_\infty) + \varepsilon \sigma_{SB} (T^4 - T_\infty^4), \quad (8-2)$$

where h is the convection coefficient set at $20 \left(\frac{W}{m^2 \circ C} \right)$, as recommended for superalloy thin-wall parts with wall thicknesses smaller than 1 mm [16], ε is the emissivity set at 0.4 as done in the previous study [135], and σ_{SB} is the Stephan-Boltzmann constant. By solving the derivative Eq. 1 and using Eq. 2 as

boundary conditions (heat loss equation) the nodal temperatures were computed. Next, a mechanical model was used to calculate the incremental strain $\Delta \varepsilon_{ij}^T$ due to thermal expansion:

$$\Delta \varepsilon_{ij}^T = \alpha \Delta T \delta_{ij}, \quad (8-3)$$

where ΔT is the incremental temperature rise and δ_{ij} is the Kronecker delta function ($\delta_{ij} = 1$ if $i = j$, $\delta_{ij} = 0$ if $i \neq j$). The total strain increment $\Delta \varepsilon_{ij}$ acting in the material was calculated as follows:

$$\Delta \varepsilon_{ij} = \Delta \varepsilon_{ij}^{E+P} + \Delta \varepsilon_{ij}^T + \Delta \varepsilon_{ij}^{\Delta V} + \Delta \varepsilon_{ij}^{Trp}, \quad (8-4)$$

where $\Delta \varepsilon_{ij}^{E+P}$ is the combination of the elastic and plastic strain, $\Delta \varepsilon_{ij}^{\Delta V}$ is the volumetric strain resulting from phase transformation, and $\Delta \varepsilon_{ij}^{Trp}$ is the transformation plasticity. In this study, the volumetric and transformation strains were assumed to have negligible effect on the total strain and set to zero [42], [161]. For elastic deformation, the following equation was used to predict the stress.

$$\Delta \sigma_{ij}^{mech} = D_{ijklm} \cdot \Delta \varepsilon_{lm}^E, \quad (8-5)$$

where D_{ijklm} is the fourth order isotropic elastic stiffness tensor calculated from Young's modulus (E) and Poisson's ratio (ν) as:

$$D_{ijklm} = \frac{E}{1+\nu} \left[\frac{1}{2} (\delta_{ij} \delta_{lm} + \delta_{il} \delta_{jm}) - \frac{\nu}{1-2\nu} \delta_{ij} \delta_{lm} \right], \quad (8-6)$$

The convex cutting plane algorithm was used to calculate stresses in the plastic region for isotropic hardening using the standard plasticity model in Abaqus, as explained by (Simo and Hughes 2006).

8.3.1.1 The AM FEM Model

A Python script was written to automate the simulation of a large number of components, and speed model setup and run times. In previous work done by [148], a detailed description of the framework, used to create and execute the simulation, was explained as illustrated in Figure 8-4. The inputs included printing patterns (in G-code format) generated from AUTOCAD Netfabb and machine settings (such as laser power and speed). Using these inputs, the Python script generated the geometry, mesh, and boundary conditions. Since phase transformation does not affect the results obtained from part-scale calculations, the solid-state temperature-dependent material properties of R108 were adopted as provided in [165]–[167] due to similar material properties (shown in ref [19]). The simulation started with the baseplate fixed from displacement in all directions at an initial temperature of 25 °C. The

Abaqus “*Model Change” feature was used to simulate the material deposition, then heat was applied to the layer to replicate the heating process [168], [169]. A ten-second cooling period was included on completion of each layer scan to replicate the recoater action during the LPBF process. The simulated geometries are classified into the following three categories:

1. Two components for validation: In order to verify the accuracy of the simulation, the model validation component was simulated, as shown in Figure 8-1.
2. The simulated components from the DOE: Simulations of all 34 experimental components were performed to study the effects of part length and printing pattern on generated residual stresses.
3. Two thick components from literature: The effect of wall thickness on residual stress and LBH was examined using two components with identical sizes of 50×50×1 mm and scanned using the “ES” and “EL” printing patterns.

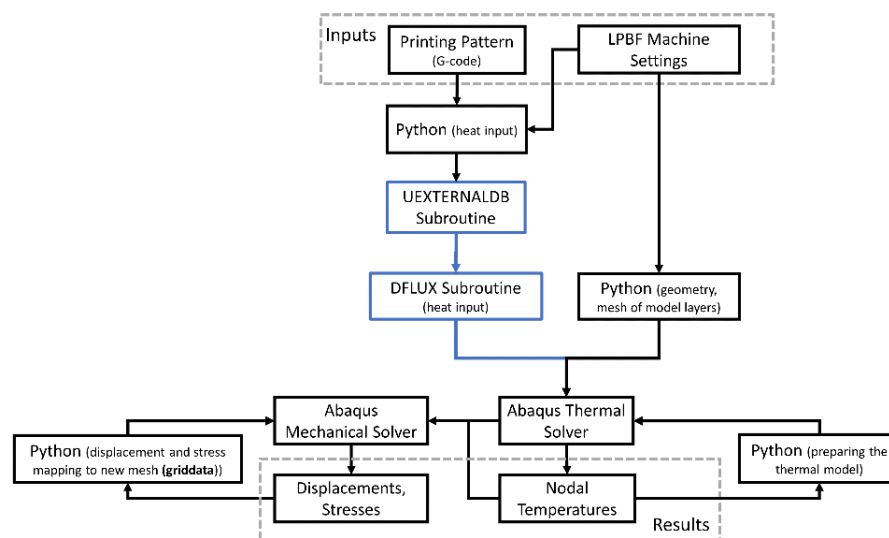


Figure 8-4: Flowchart of the computational framework including subroutines (blue) and interactions with customized Python programs

8.3.1.2 The heat source model

Simulation of the entire LPBF process at the beam scale is computationally expensive due to the small laser size and layer thickness. Typical beam-scale AM simulations require over one million time steps

and elements making them inefficient for part-scale simulations [19]. Researchers overcome this problem by simulating the laser process with a much larger heat input than the actual laser size. Commonly used methods to model the heat input include the lumped heat input and layer heating (flash heating) techniques. This study combines the two heat input models to enhance the computational time. Each heat input is explained as follows:

I. Lumped Hybrid Line (LHL) Model

The small beam diameter limits the step time and increases the processing time. To overcome this problem, the hybrid line (HL) heat input model (Figure 8-5 (a)) was applied. The HL heat input model was parameterized using the time step, which make it beneficial to decrease the number of step times:

$$Q = \frac{P\eta}{\sqrt{2\pi}\Delta t v H r_l} e^{\left(-\left|\frac{z}{H}\right| - 2\left(\frac{y}{r_l}\right)^2\right)} \left(\operatorname{erf}\left(\frac{\sqrt{2}(x_{end}-x)}{r_l}\right) - \operatorname{erf}\left(\frac{\sqrt{2}(x_{start}-x)}{r_l}\right) \right), \quad (8-7)$$

where P is the laser power and the parameter η is the absorption factor obtained from (Keller et al. 2017). The function erf is the error function, while x_{start} and x_{end} are the spatial start and endpoints of the heat input model. These two variables are defined by the beam radius r_l , laser speed (v) and time step (Δt). For ease of reference, the normalized value of τ , which is the ratio of the laser travel ($v\Delta t$) over the beam radius (r_l), was used as follows:

$$\tau = \frac{v\Delta t}{r_l}, \quad (8-8)$$

For the “EL” printing pattern, the maximum value of τ was set to 60 as it is limited by the wall thickness. Part manufacturing using LPBF typically involves printing thousands of tracks. To reduce the computational time, layers and tracks are grouped together using the lumping technique. Lumping the line heat input models yields a substantial reduction in computational time essential for part-scale simulations. In this study, the lumped HL approach is referred to as LHL. Figure 8-5 (b) and Figure 8-5 (c) shows schematic representations of layer and track lumping, respectively. For example, lumping 3 layers consisting of 3 tracks each (Figure 8-5 (d)) reduces the computational time by 9X compared to a single track (Figure 8-5 (a)). According to Bayat et. al. [161], [170] and An et. al. [15], lumping up to 20 layers with 20 tracks each produces accurate results. In this study, up to 10 layers with 2 to 16 tracks each were lumped to ensure the model's accuracy. The number of lumped sets was determined by the total number of tracks within a layer. Implementation in Abaqus requires the UEXTERNALDB

subroutine, which reads the G-code file and calculates the laser position with multiple CPUs. Next, the calculated data is sent to DFLUX subroutine to compute the heat input magnitude on the material (see blue boxes in Figure 8-4). The calculated heat input is sent to the solver to predict the temperature, strain, and stress for the designated increment. Cyclic repetition of the simulation process along with the mesh coarsening algorithm (explained in section 8.3.1.3) generates the in-process data for the whole process.

II. Layer Heating (LH) Model

To simulate the material deposition process in a single time step, an entire layer is typically activated and heated at once [90], [170]. In order to further reduce computation time, the layers can be grouped and simulated at one time. This technique is called the layer heating (LH) approach and the volumetric heat input is given by:

$$Q = \frac{P\eta}{w \times H \times D}, \quad (8-9)$$

where, w is the melt pool width, H is the lumped layer thickness, and D is the beam diameter taken from. [135] To maintain the model accuracy and decrease the processing time, only the first 50 layers were simulated using the LH model, as shown in [171].

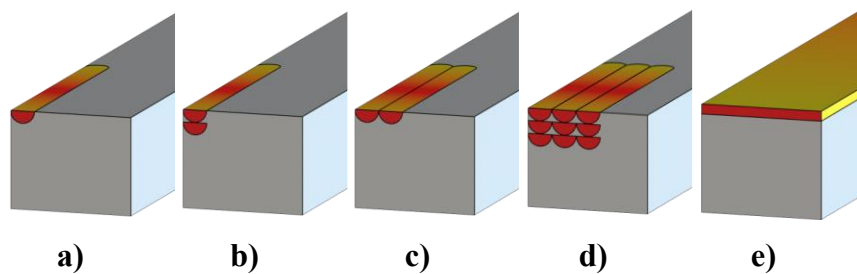


Figure 8-5: Schematic showing a) single HL, b) layer lumping, c) laser track lumping, d) three-layer-three-track lumping, e) layer heating modelling techniques.

8.3.1.3 Meshing Algorithm

Coarser element sizes help to speed up computations and finer elements are necessary to capture deformation in materials with inhomogeneous temperature fields and high nodal temperatures. The elements have a smaller size for the top layers due to the interaction with the laser, but they are more flexible for the outer layers because of the lower nodal temperature and more uniformity. During the process, layers may become more distant from the top layer and can be modelled with coarser elements. This highlights the importance of using dynamic meshes to increase the element size, as the simulation progresses and reduces computation time while preserving accuracy. To implement dynamic mesh, a mesh coarsening technique was implemented with Abaqus “mesh-to-mesh solution mapping” technique [80], [82]. The developed framework increases the element size during the process and allows the thermal and mechanical models to run almost simultaneously. Details of that implementation are illustrated in Figure 8-4 and can be found in [148]. The element types are DC3D8 and C3D8 for the thermal and mechanical simulations. The element size and coarsening rate presented in ref [80] increase the element sizes every four layers. To ensure model accuracy, a more conservative element size and coarsening rate (every 50 simulated layers) were adopted compared to the literature [80], as shown in Table 8-2 and Figure 6. Due to laser interaction, rapid heating, and rapid cooling, the first 50 layers have the finest element sizes [82]. From layer 50 to 150, the element size is increased in all directions to enhance computational efficiency. From layer 150 to the end of the component, the element size in the Z direction was kept constant to ensure model accuracy, based on previous recommendations [148].

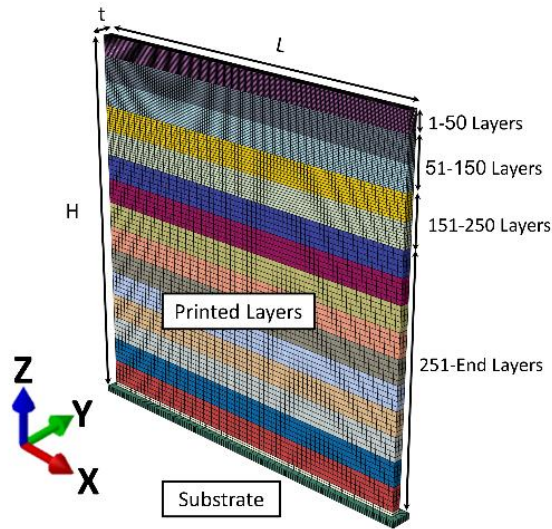


Figure 8-6: Part-scale meshed model to simulate the process for different LPBF parameters. Sections are colored to distinguish element sizes in **Table 8-2**.

Table 8-2: Element size in micron for each meshed layer of the part-scale simulation.

Layer's number	Length (X)	Width (Y)	Height (Z)
1-50	200	100	80
51-150	300	150	160
151-250	400	200	160
251-End	600	300	160

8.4 Model Evaluation

8.4.1 Computational Time

The processing time required for the model presented in this study is shown in Figure 8-7. Simulation times for 16 mm tall parts including two thicknesses (0.5 mm and 1 mm) and four different lengths (30 mm, 40 mm, 50 mm, 60 mm) are compared. The error bars represent the variation in processing times for the 8 different printing patterns presented in Table 8-1. This is because the vector length affects the

number of time steps required for the HL model. For this study, the τ value in Eq. (8-8) was optimized for EL scanning strategy and for 30 mm part lengths.

There is a direct correlation between simulation time and the number of elements. For a given part thickness, the number of elements and computational time increase linearly with increasing part length, as shown in Figure 8-7. The effect of element number on simulation time is investigated in detail by Tangestani et al.[172].

The simulation time is also affected by the number of laser tracks required for each printed layer. For example, for a part length of 30 mm, the process time increases by 8X when the part thickness increases from 0.5 mm to 1 mm. This is because the LHL lumping parameters are optimized for the 0.5 mm part thickness. The processing time for the 1 mm parts can be reduced by lumping more tracks, but conditions are kept constant here for comparison purposes.

The simulation time can be reduced significantly by using the layer heating (LH) approach alone. For instance, considering a 60 mm \times 0.5 mm \times 16 mm (length \times thickness \times height) part, simulation using LH takes less than 20 hours as opposed to 374 hours using the LHL approach shown in Figure 8-7. However, this would eliminate the effect of printing pattern on the residual stress [92], the main topic of this study. Note that the presented code can simultaneously handle the LHL and LH heat input models. This means that the model could utilize the LHL input models for areas with high stress gradients and the LH input model for areas with uniform stress distributions. Therefore, the computation efficiency of the combined LH-LHL model presented here can be improved with better evaluation of the heat input for each part dimension.

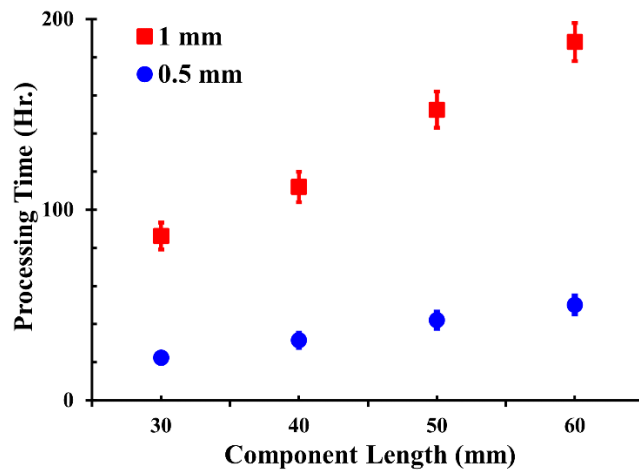


Figure 8-7: Computational time associated with part thickness and length for the eight printing patterns investigated here. The part height is kept constant at 16 mm. The error bars show the variation between the required time to simulate different printing patterns.

8.4.2 Model Accuracy

The comparison between printed and simulated part distortion for two different printing patterns (“EL” and “ES”) are shown in Figure 8-8. All printed parts were 1 mm thick, 10 mm long and 20 mm high, as described in section 8.2.2 A MATLAB code was generated to record and plot the predicted deformation.

For the experimental part, the 3D scanner captured the deformation of the component and the PolyWorks software was used to calculate the deviation from the designed CAD file. The predicted and measured deformations are labeled on both components. The large deviation between the simulations and experimental measurements observed on the top layer was artificially created by a misalignment between the scanning results and the CAD file containing the reference parts. Otherwise, the simulation predicted the part distortion with less than 10% error for the two components considered in Figure 8-8. The largest deformation (~100 μm) is situated along the part sides and most of the error comes from the front face of the components due to the layer activation approach employed in the model. The “*Model Change” tool activates elements with initial strain from the previous layer, which results in

the elimination of small deformations at the surface and smoothens the results. Note that this problem does not have significant impact on the residual strain or stress created by large-scale simulations and "*Model Change" is commonly used by researchers [161], [169]. Therefore, the modeling approach can accurately predict the effect of scanning strategy on part distortion and residual stresses induced by the LPBF process.

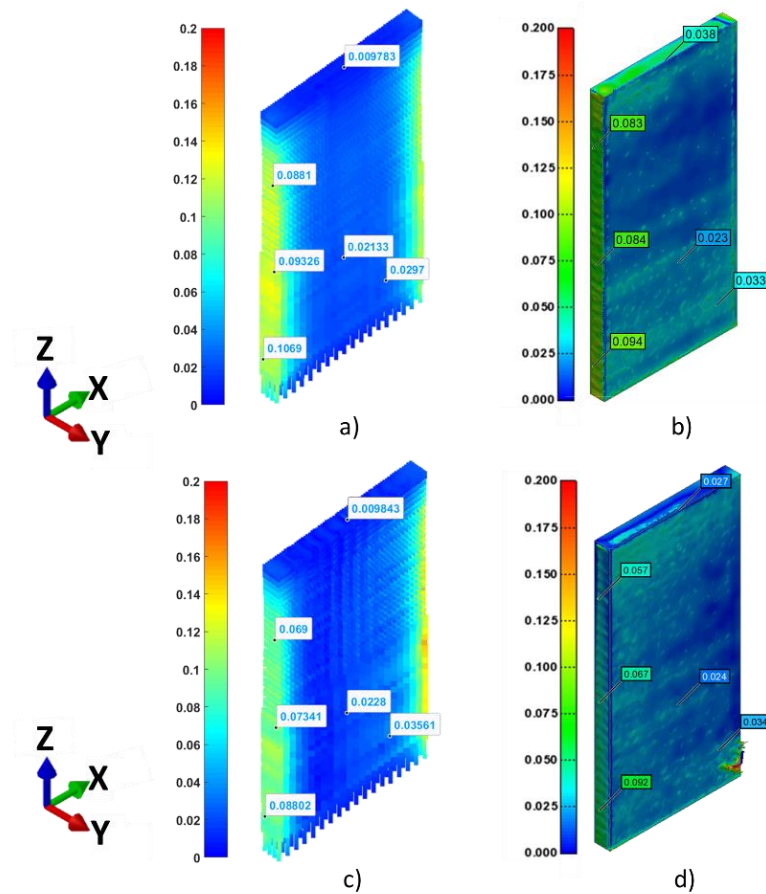


Figure 8-8: A comparison between simulation and experimental measurement of part distortion. Two different scanning strategies are compared. The deformations created by the “EL” scanning strategy, obtained from a) simulation and b) experimental measurement, and by the “ES” scanning strategy, obtained from c) simulation and d) experimental measurement, are demonstrated.

8.5 Results

8.5.1 Experimental Observations of LBH in Printed Thin-Wall Components

Figure 8-9 shows the measured LBH values of the 0.5 mm thick components (white, blue, red, and black columns) obtained from the DOE and the 1 mm components (green columns) obtained from (Chakraborty et al. 2021). The results include non-rotational (Figure 8-9 (a)) and rotational (Figure 8-9 (b)) printing patterns. The label above each chart shows the 2 types of failure explained in section 8.5.2. “N/A” was reported for 0.5 mm thick components with: a) 40 mm length, “S” pattern b) 50 mm length, “R” pattern, and c) 50 mm length “L-L” pattern. These components were affected by deviation of the neighboring components. The 0.5 mm thick components that reached the designed build height (30 mm) did not exhibit LBH behavior under the present processing conditions.

8.5.1.1 Effect of Printing Patterns on Thin-Wall LBH

8.5.1.1.1 Printing patterns without scanning angle rotations between the layers

A comparison of the scanning strategies in Figure 8-9 (a) shows that components with long vector lengths (e.g., “L” and “EL”) are associated with a greater LBH than those with short vector lengths (e.g., “S” and “ES”). For example, a 0.5 mm thick component with “S” printing pattern exhibits a LBH between 18 mm and 22 mm (depending on the part length), whereas a part with “L” printing pattern has a LBH between 23 mm and 30 mm. The LBH of a component with 30 mm length increases by 50.3% when the printing pattern changes from “ES” to “EL”. For 1 mm thick components, the increase in LBH from “ES” to “EL” is 60%, indicating that thicker components are more sensitive to changes in vector length during processing.

8.5.1.1.2 Printing patterns With Scanning Angle Rotations Between the Layers

Figure 8-9 (b) shows the effect of vector length (VL) on LBH when vector rotation is introduced between successive layers. The “S-S” parts have LBH values ranging between 19 mm and 22 mm, while two of the three “L-L” parts reached the desired height (30 mm). Introducing vector rotation between the layers increases the LBH. Comparing Figure 8-9 (a) and (b) reveals that “L” and “S” patterns (Figure 8-9 (a)) with no scan rotations have systematically lower LBH (up to 16%) than their counterparts with inter-layer rotations (“L-L” and “S-S” in Figure 8-9 (b)). The LBH values of the

continuously rotating printing patterns (“EL-ES” and “R”) are similar and lie between the LBH values obtained using the short (“S-S”) and long (“L-L”) VL patterns. This is because the continuous rotation printing patterns create alternating layers with short and long vectors.

8.5.1.2 Effect Of Part Dimensions on Thin Wall LBH

Increasing the part length improves the LBH for both rotational and non-rotational scanning patterns in Figure 8-9. For example, at a constant wall thickness of 0.5 mm and “ES” printing pattern, increasing the length from 30 mm to 60 mm raises the LBH by 4.5 mm (20% enhancement). This effect is thus significantly smaller than the VL presented in the previous section. However, enlarging the part thickness generates a more pronounced increase in the LBH. For example, at a constant part length of 30 mm and “ES” printing pattern, the LBH increases by 72% when the wall thickness increases from 0.5 mm to 1 mm in Figure 8-9 (a). According to Chakraborty et al. 2021), thicker parts exhibit higher LBH due to lower susceptibility to buckling during LPBF.

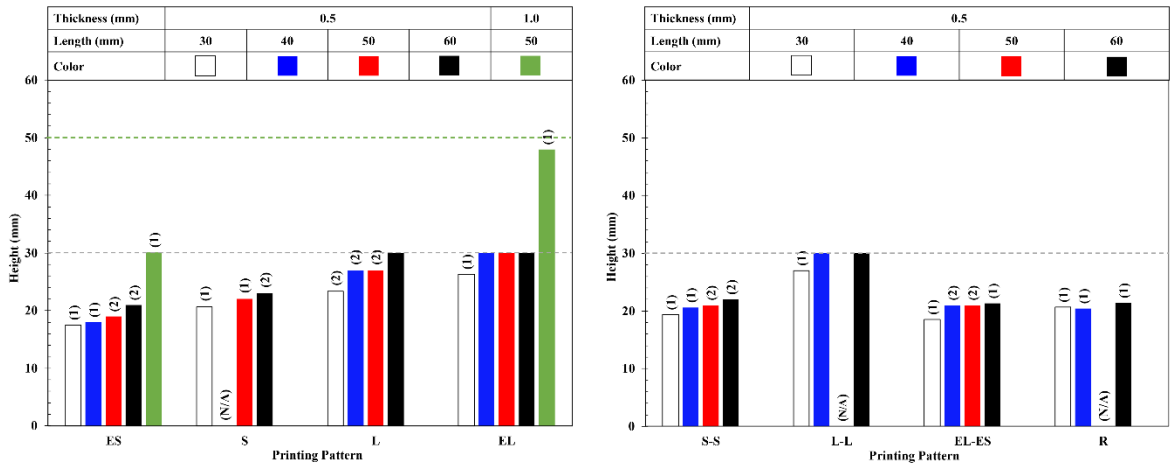


Figure 8-9: LBH of the as-built thin-wall parts processed under the conditions described in Table 8-1. The LBH values for components scanned with the a) printing patterns without inter-layer scan rotations, and b) printing patterns with inter-layer scan rotations are shown. Data for the 1 mm thick components (green) is derived from literature (Chakraborty et al. 2021). The gray and green dotted lines denote the target heights for 0.5 mm and 1 mm part thicknesses, respectively.

8.5.2 Part Failure Mechanism Causing LBH

The two types of part failure morphology causing LBH (illustrated in Figure 8-10) are summarized in the following sections. Note that failure did not initiate from any internal cracking mechanisms. This has been discussed in detail elsewhere [10].

8.5.2.1 Failure Type One (Complete Top):

The component is completely detached at the top layer, as shown in Figure 8-10 (a). A similar type of failure was previously reported and attributed to buckling in the X-Z (rotation along the X-axis) plane [10]. Figure 8-10 (b) illustrates the side view of the component after failure. The printed part is deviated (shown with green line) from the centerline (shown with dash blue line). The deviation leads to part failure during the process as the laser deposits the subsequent layer on empty space. According to [10], thinner parts are more susceptible to buckling, while thicker parts improve the LBH by providing additional space for the next layer to be placed.

8.5.2.2 Failure Type Two (Incomplete Top):

Figure 8-9 shows that the failure morphology changes when the part length increases. Failure becomes localized at the part corners, as shown in Figure 8-10 (c). Buckling in the Y-Z plane (see the red line in Figure 8-10 (d)) now occurs in addition to the previously observed buckling in the X-Z plane (green line in Figure 8-10 (d)). This type of defect is caused by accumulated localized deformations at the corner of the component. The process continues and deposits few more layers on a portion of the component, ultimately resulting in part failure resembling failure type one.

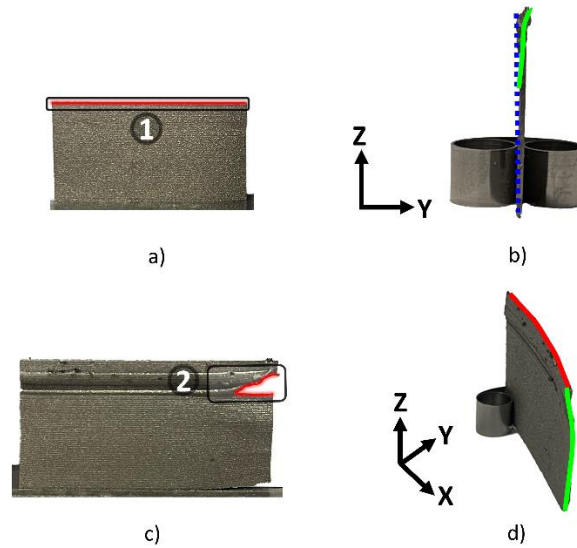


Figure 8-10: The two types of failure observed causing the LBH during LPBF process reported in Figure 8-9. Type one a) front and b) side views show a clear rupture along the centerline due to buckling in the X-Z plane. Type two c) front and d) side views show failure localized at part corners due to a combination of buckling in the X-Z (rotation along the X axis) and Y-Z planes (rotation along the Z axis).

8.5.3 Simulation of Part Distortion and LBH

The part distortion and LBH were simulated using the modeling approach described in section 8.3. A representative subset of 6 parts built with different printing patterns and part lengths was compared with the simulations in Figure 8-11. All parts are equally thick (0.5 mm), and the printing pattern and wall length are provided above each simulation figure.

The model successfully captures the general trends in part distortions for all the printing patterns and part dimensions evaluated in this study. For example, the “ES-30 mm” part shown in Figure 8-11 (a) exhibits a type one failure. The simulation results show excessive part displacement near the top of the part. This results in misplacement of the following with respect to the centerline (X-axis) due to buckling in the X-Z plane. Accordingly, the tip of the part in Figure 8-11(a) shows material accumulation offset from the bottom section. The R-30 mm built and simulated parts (Figure 8-11 (b)) exhibit less distortion compared to the “ES-30 mm” part in Figure 8-11 (a). Continuous vector rotation

is well known for reducing the amount of residual stresses and strains in LPBF parts [136]. The effect of vector rotation on distortion is also well captured in the “R-60 mm” part in Figure 8-11 (c). The model predicts lower distortions compared to the “ES-60 mm” part in Figure 8-11 (d). The latter simulation and experimental part both show curvature along the Z-axis and localized distortion along the X-axis close to the tip. This confirms the model’s capability to capture the effect of scanning strategy on part distortion.

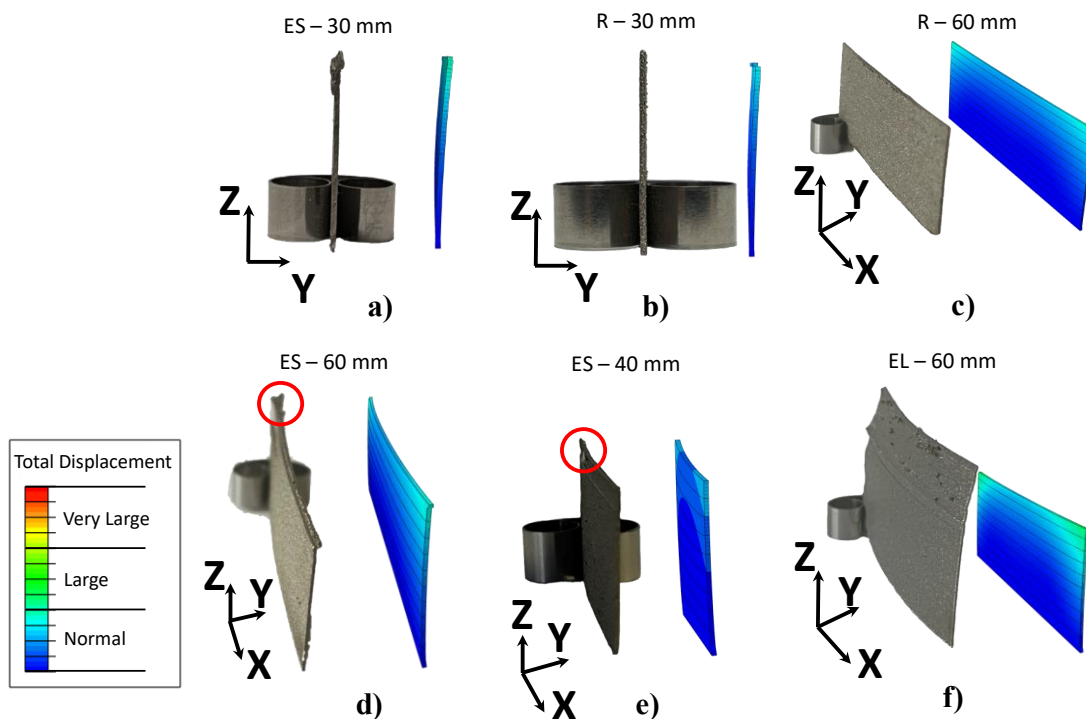


Figure 8-11: Comparison between simulation and experimental distortion for 6 components with various dimensions fabricated using different printing patterns. The printing pattern and wall length are given above each figure. All thin-wall components are equally thick (0.5 mm).

The model can also accurately capture the effect of part length on the buckling behavior. Buckling essentially occurs in the X-Z plane of the “ES - 30 mm” part in Figure 8-11 (a). The model shows that the displacement is localized at the tip of the part and evenly distributed along the X-axis (not shown in Figure 8-11 (a)). Figure 8-11 (d) and (e) show that increasing the part length promotes more buckling

in the Y-Z plane and strain localization at the part corners in both experimental (see red circles regions) and simulated parts. This agrees well with the failure modes reported in Figure 8-9.

Overall, the LBH is well captured for all conditions (except the longer vector length components in Figure 8-11 (f)) presented in Figure 8-11. The effect of VL on LBH simulations is better illustrated in Figure 8-12 where experimental and simulated LBH are compared for extra-short “ES” and extra-long “EL” printing patterns. The simulation captures the LBH for printing pattern "ES" for all thin-wall parts with varying thicknesses and lengths, as shown in Figure 8-12 (a). The simulation error is less than 10 % compared to experimental results. On the contrary, Figure 8-12 (b) shows a large difference (approximately 33 %) between the predicted and experimental LBH when longer vector length is used. These results indicate that the model fails to reproduce the impact of the VL on LBH even though a directional heat source is used

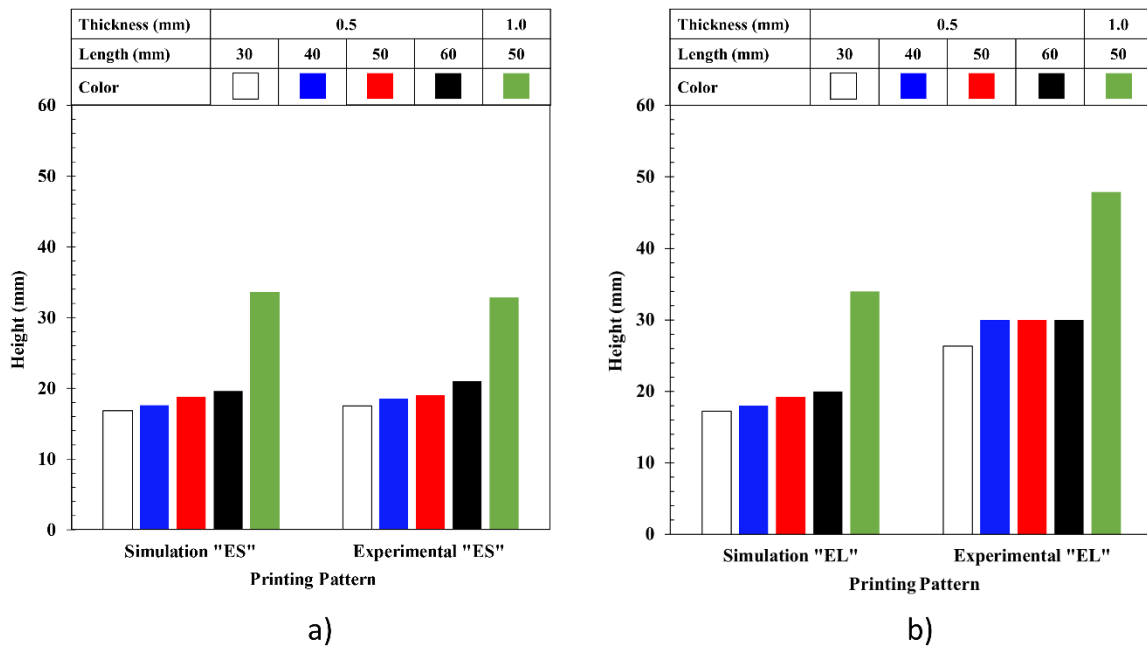


Figure 8-12: Comparison between observed and simulated LBH for a) “ES” and b) “EL” printing patterns.

8.6 Discussion

The discrepancy between the model and experimental LBH is explained by two reasons. Firstly, the simulation terminates when results diverge due to excessive local distortion. This occurs when a large gap forms between the new layer and previously deposited layers causing the distortion of elements, as highlighted in yellow in Figure 8-13. The distorted elements contain large local strains that exceed the software threshold halting the simulation. However, in the LPBF process, a critical strain threshold does not exist, and the simulation will continue if the following layer can be built over a solid section, as shown in Figure 8-11 (a). This is also discussed in more details elsewhere [10]. Secondly, failure analysis summarized in section 8.5.2 reveals that buckling plays a major role in the LBH. When buckling occurs, the LPBF process continues depositing more layers and the deviation from centerline, becomes larger. After a certain height, the created gap is enough to suppress subsequent layer deposition. Note that the amount of strain in buckling is too high to be managed by the model. This causes divergence and the model aborts on the first sign of buckling. Hence, the simulation generates a conservative LBH value, where the model systematically predicts smaller LBH compared to the actual process. This is observed for the short vector length and becomes more apparent for the long vector length in Figure 8-12.

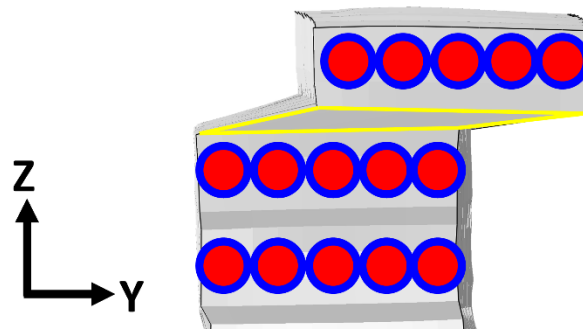


Figure 8-13: A schematic of the simulated laser track and the newly deposited layer illustrated with the distorted element (yellow color) causing model termination.

The presented model accurately captures part distortion, despite the limitation of LBH prediction. To shed further light on the effect of vector length and part length on the failure modes, the residual stresses are evaluated in the following sections.

According to [148], the maximum stress along the wall thickness (Y) is 30 and 24 times smaller than along the build direction (Z) and part length (X), respectively. This can be explained by the plane strain theory as the printed wall thickness is significantly smaller than its length and height. Therefore, only the longitudinal stress (SXX) and stress in build direction (SZZ) are discussed in the following sections. The models are sectioned through the center to show the internal stresses.

8.6.1 The Effect of Printing Pattern on Residual Stresses

Figure 8-14 and Figure 8-15 compare the residual stresses between eight different printing patterns (see Table 1) in the build (SZZ) and longitudinal (SXX) directions, respectively. For a fair comparison between the printing patterns, the model dimensions are kept constant (30 mm long, 0.5 mm thick and 17 mm high). The internal stresses are mostly compressive along the build direction for all 8 printing patterns. This explains the highest propensity for buckling in the X-Z planes, as shown in Figure 8-10 (a) and (b). Interestingly, the compressive stress intensity regions (highlighted by the black boxes) in Figure 8-14 grows when the vector length decreases from “EL” to “ES”. For shorter VLs, buckling is thus expected to occur at a lower height. As the VL increases, compressive stresses along the BD become smaller enabling further layer deposition before buckling occurs. Accordingly, Figure 8-9 (a) shows that the LBH increases with the VL.

The current results suggest that buckling appears more suddenly when shorter VLs are employed. For instance, considering the ES printing strategy, the model abortion height is similar to the experimental part height, as demonstrated in Figure 8-12 (a). The part has lesser time to accumulate strain before the critical height for buckling is met, thus the model predicts LBH more accurately. Figure 8-11 shows how excessive local distortion causes premature abortion of the model. Conversely, when longer VLs are used, more displacement occurs before reaching the LBH. This is shown in Figure 8-11, where the experimental “EL-60 mm” part accumulates dramatically higher distortion than the “ES-60 mm” part before reaching LBH. In this case, the model divergence due to accumulated distortion occurs before the real LBH. This explains LBH underestimation when the VL increases in Figure 8-12.

The VL is also important when vector rotation is introduced between successive layers. Figure 8-14 clearly shows how the high compressive stress intensity areas (black box) decrease when the VL increases (see difference between “S-S” and “L-L”). The “EL-ES” and “R” printing patterns produce

combinations of short and long VLS causing intermediate residual compressive stress intensities. This is in good agreement with the LBHs demonstrated in Figure 8-9, where “S-S” and “L-L” printing patterns produce smaller and larger LBHs, respectively, while “EL-ES” and “R” produce intermediate LBH values.

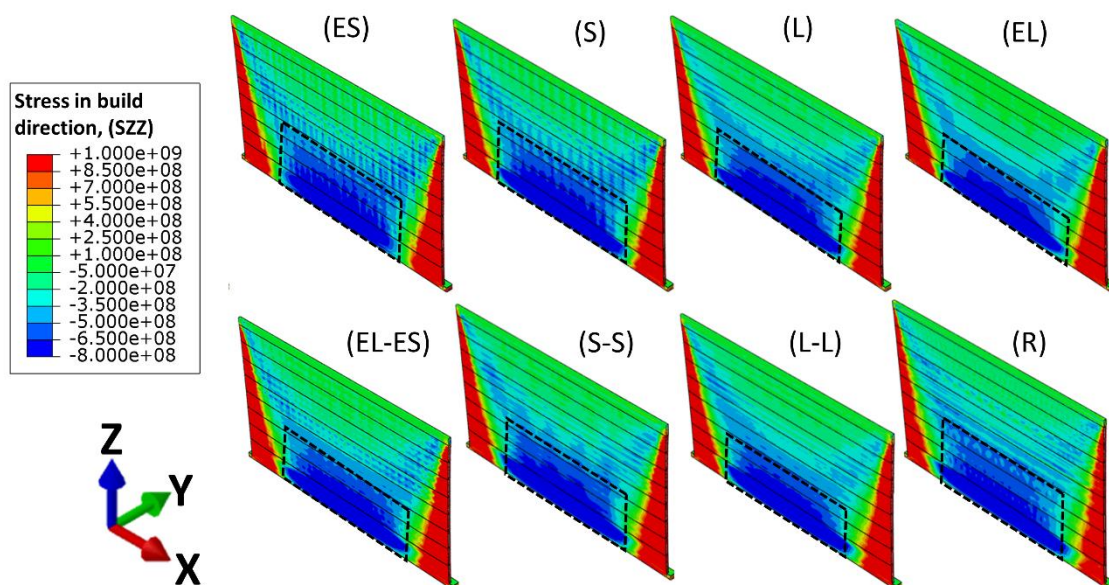


Figure 8-14: Stress along the build direction (SZZ) for the 8 different printing patterns investigated. The parts’ thickness, length and height are 0.5 mm, 30 mm and 17 mm, respectively. The printing patterns are labelled on top of each component according to labelling described in Table 8-1. The residual stresses are shown along a centerline cross section of the parts.

Figure 8-15 illustrates significantly different stress characteristics along the longitudinal direction (SXX). Most parts are under tensile stress with the stress concentrated at the top of the components. Interestingly, the components with longer vectors are subjected to greater compressive stresses at the top corners. The EL-60mm experimental part in Figure 8-11 (f) shows how this compressive stress promotes excessive curling of the corners as the bottom is constrained and the top is free to bend.

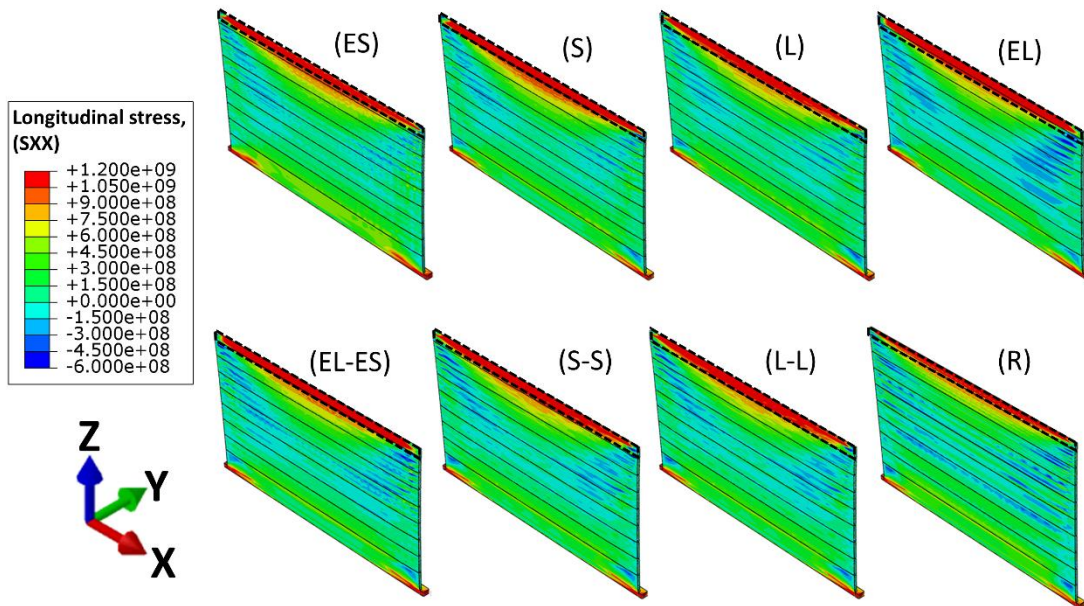


Figure 8-15: Longitudinal stress for the 8 different printing patterns investigated. The common part thickness, length and height are 0.5 mm, 30 mm and 17 mm, respectively. The printing patterns are labelled on top of each component as shown in Table 8-1. The residual stresses are shown along a centerline cross section of the parts.

8.6.2 The Effect of Part Length on Residual Stresses

The effect of part length on the residual stresses is shown in Figure 8-16. The compressive stress in the build direction causing buckling in the X-Z plane decreases significantly with part length, as demonstrated by comparing the blue areas in the 40 mm and 60 mm long parts in Figure 8-16 (a). This explains why type one failure, caused by excessive buckling in the X-Z plane, is limited to shorter parts in Figure 8-9.

Figure 8-16 (b) shows that the compressive stress magnitude along the corner in the SXX direction, contributing to buckling in the Y-Z plane, remains constant with part length. According to the plate theory [173], [174], buckling susceptibility in the Y-Z plane increases with the part length. Accordingly, type two failure localized along the part corners are observed more frequently in longer parts, as shown in Figure 8-9. On the other hand, buckling in the X-Z plane is not affected by the part length. In

summary, as the part length increases, buckling along the Y-Z plane increases due to geometric factors. On the contrary, buckling in the X-Z plane decreases due to reduced compressive stresses in the build direction.

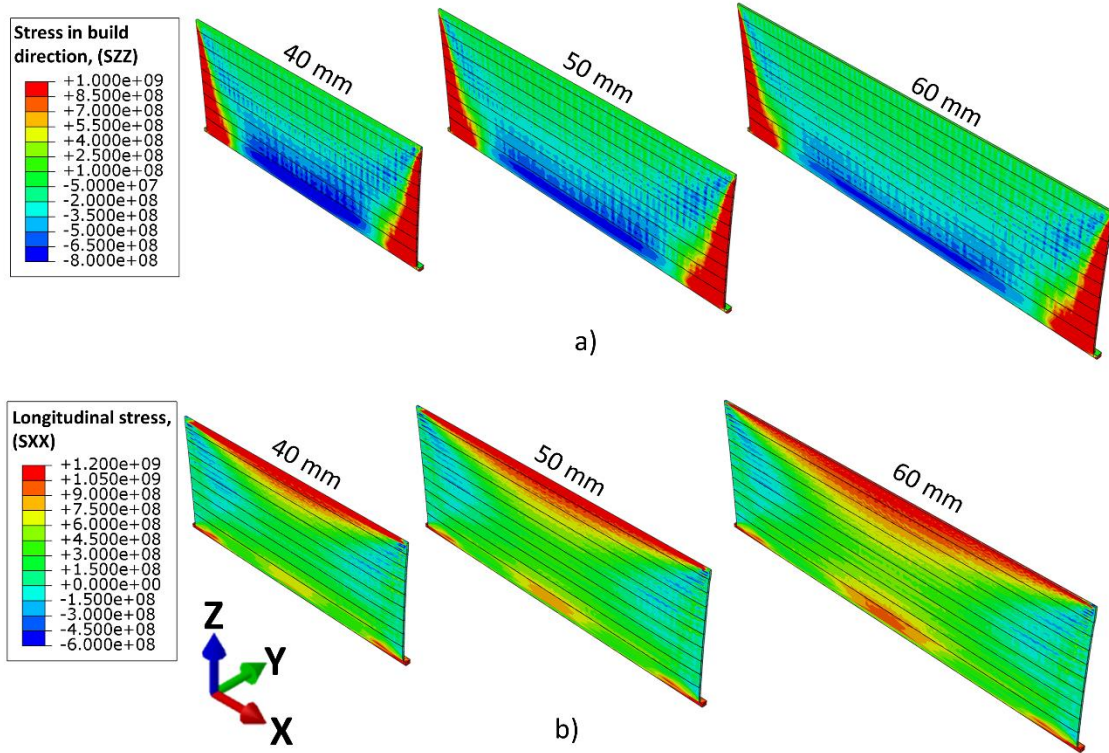


Figure 8-16: Comparison between a) build direction (SZZ) and b) longitudinal (SXX) residual stresses for three different part lengths. The part lengths are labelled above each component. The printing pattern is “ES”, the part height is 17 mm, and the wall thickness is 0.5 mm. The residual stresses are shown along a centerline cross-section of the parts.

8.7 Conclusion

A novel framework is developed to simulate actual-scale components without compromising the directionality of the stress components generated by the laser tracks. The hybrid line model, where the laser beam heat source is integrated along the track directions, is coupled with a lumping approach, which allows several laser tracks to be combined for higher computational efficiency. Furthermore, a layer lumping approach is incorporated to accelerate the simulation of component sections of low

interest and a mesh coarsening technique is used to simultaneously execute the thermal- and mechanical simulations to minimize the computation time.

The model can predict thin-wall part distortion accurately within 10% of the experimental error in reasonable time using low processing power. Each simulation only requires 12 cores of dual Intel Xeon gold 6240 processor allowing the simulation of different parts simultaneously. This makes the model especially suitable for LPBF parametric studies. On the other hand, the model cannot replicate the deformation occurred after buckling as it requires dynamic simulation leading to increase in processing time. Furthermore, the buckling simulation requires detailed model definitions therefore it is not possible to use the assumptions used in this study leading to increase in computational processing time.

The distortion and underlying causes for premature part failure frequently encountered during the LPBF of high gamma-prime Ni-based superalloys thin-wall parts are studied. The DOE includes 34 thin-wall components fabricated by LPBF. Emphasis is placed on the effect of printing patterns and part length on the distortion and LBH of the printed parts. In total, 8 different printing patterns with different vector lengths and interlayer rotations for 5 different part lengths are studied. The LBH phenomenon is shown to stem from the buckling of components during printing. The buckling modes are found to be sensitive to part dimensions, while the printing pattern influences the intensity of residual stress that causes buckling.

The directional heat source model used in this study can accurately predict the effect of scanning strategy and part dimensions on part distortion. For a fixed part length, a strong effect of the VL on the LBH is observed where the LBH increases by 50%-60% with increasing VL (by decreasing scan angle). The model shows decreasing compressive residual stress along the build direction that reduces buckling. When the part length is small, buckling is more homogenous and promotes clean part failure along the part length. For a fixed scan angle, the part length has smaller significance on the LBH. The part height increases only by 20% when the part length increases. Localization of the compressive stresses along the part length direction at the upper part corners causes a shift in the buckling mode when the part length increases. Accordingly, part failure becomes less homogenous and more localized along this region. Finally, interlayer laser vector rotation reduces the part distortion and increases the LBH as the internal stresses become more homogeneously distributed.

This parametric study shows strong correlation between the printing pattern and LPBF part quality. Inter layer vector rotation is necessary to reduce the residual stresses and final part distortion. The optimum printing conditions to minimize part distortion and maximize LBH are achieved by maximizing the number of long vector lengths through interlayer scan rotations.

Chapter 9

Conclusions and Recommendations

9.1 Major Conclusions

This thesis presents two computationally efficient models to simulate the LPBF process for thin-wall components made of Ni-based superalloys. The model calibration involves large physical and mechanical datasets based on RENÉ 108 and RENÉ 65. The models are validated using several different methods, including melt pool geometry measurement, XRD residual stress measurement, and LPBF part distortion using a 3D scanner. A series of simulations are performed to analyze and optimize the printing parameters for the fabrication of thin-wall parts made of Ni-based superalloys. The key points of this research are as follows:

9.1.1 The Hybrid Line (HL) Model

The HL model is developed as an integrated form of the ED heat input model for the LPBF process. The calibration of the heat input is based on the mechanical and physical properties of high gamma prime superalloys. In addition to capturing phase transformations, the model is computationally efficient. The HL model accuracy and processing time are determined by the step time size (τ). Utilizing smaller τ allows for higher accuracy in predicting the results, while the larger step time results in better processing efficiency. This way, the model can be adjusted for greater computational efficiency and accuracy.

- The HL model is compared with large experimental DOEs and beam-scale (ED) models to determine the precision of the predicted thermal and mechanical results:
 - o The HL heat input model predicts nodal temperatures and cooling rates within 15% error of ED for τ between 5 and 20. The nodal temperature and cooling rate play a crucial role in residual stress calculation since they are inputs for mechanical simulation.
 - o In a single-track evaluation, the HL model captures the stress directionality within a 5% error of the ED model (for τ ranging from 5 to 20). This results in accurate

prediction of the experimental results for twelve components printed with different laser powers and printing patterns with only 54 MPa error. This is less than 4% of the RENÉ 65 yield stress at room temperature.

- The HL model demonstrates better processing time performance than the beam-scale heat input model (ED in this study).
 - o Simulations are divided into thermal and mechanical analyses. In the thermal simulation, the HL model is 300-1600 times faster than the ED heat input model for τ ranging from 5 to 20. For mechanical analyses and similar conditions, the HL model is between 5 and 30 times faster than the ED heat input model. This makes the HL thermo-mechanical simulation of actual components about 150 times faster than the ED heat input model.
 - o The mesh coarsening method is optimized to reduce the simulation processing time by more than three times regardless of the HL step time (τ). With the framework, thermal and mechanical models are executed simultaneously with fewer elements.

A parametric study is conducted on printing parameters using the HL model. This evaluation is broken down into two categories, melt pool and residual stress:

- For the first time, the effect of the laser power and speed on the melt pool size is studied for high gamma prime superalloys (RENÉ 65). Both the simulation and experimental results show the laser power has an 8x stronger counter-impact on the melt pool size compared to the laser speed.
- Residual stress is studied with a DOE of twelve components with three laser powers and four printing patterns. The findings of this study are as follows:
 - o Due to plane stress theory, the stress in the thickness direction is smaller than in the build and longitudinal directions. Previous studies are not able to assess the effect of the printing pattern on directional stresses in thin-wall parts.
 - o The laser power has a stronger interdependent impact on residual stresses than the direct effect. It impels, as the laser power increases the effect of the printing pattern on the residual stresses is enhanced. Thus, the selection of optimal printing patterns

becomes more important with higher laser power. It facilitates the selection of machine settings with a greater degree of flexibility.

- o Printing patterns with longer vector lengths tend to create larger residual stresses in the length direction and smaller compressive stresses in the build direction. Printing patterns with interlayer rotation angles are effective for homogeneous creation of residual stress in components. Hence, selecting a suitable printing pattern improves part quality, as longitudinal stress and stress in the build direction affect microcracking and in-process part failure, respectively.

9.1.2 The Lumped Hybrid Line (LHL) Model

Due to its restriction to simulate LPBF processes for small components, the HL model has limited application. This leads to the development of a lumped HL (LHL) heat input model for larger components. In addition to being computationally efficient, the model is highly accurate in predicting directional stresses. As a result, the model is capable of studying in-process failure mechanisms in relation to the part geometry and printing patterns.

- LHL model accuracy is validated by performing experiments, and the results are as follows:
 - o LHL's model is able to accurately predict the deformation of printed components within 10% error compared to measurements made with 3D scanning. As a result, the model is an acceptable tool to predict the deformation and residual stress associated with the LPBF process.
 - o Based on a comparison between predicted deformation and experimental results, the model is able to capture stress directionality and generate deformations for eight different printing patterns.
 - o Using the model, it is possible to predict the minimum LBH for components with different geometries. It indicates that the LBH is conservatively predicted, thereby ensuring part quality.

- The simulation of full-scale components is highly efficient with this model. This makes the LHL model well suited for parametric study for large-scale components. Here are the details of the achieved processing time:
 - o Simulating a component with dimensions of 0.5 mm × 17 mm (thickness × height) and length of 30-60 mm takes between 22 and 50 hours. For similar length, height, and thickness of 1 mm, the processing time ranges from 86 to 188 hours. Better optimization would reduce the time further for components with 1 mm thickness.
 - o The framework can switch the heat input to the layer heating technique during the simulation. This makes the simulation up to 19 times faster than using only the LHL heat input model. The goal is to gain computational efficiency and accuracy depending on demand.
 - o To simplify the framework, it is designed with the least number of inputs possible. In addition, it does not require much computation power to run the simulation. Due to these capabilities, the framework is suitable to execute multiple parallel simulations, which is essential for parametric studies.

A LPBF parametric study is performed to evaluate the effect of part geometry and printing pattern on part failure during the process. Here are the results of this evaluation:

- The experiment includes a DOE of 36 components with eight printing patterns, six part lengths, and two part thicknesses. As part of this evaluation, the parameter "limiting build height" (LBH) is proposed to determine the effect of each parameter on the susceptibility of part failure.
 - o During the process, thin-wall parts are prone to buckling, which is a leading cause of failure. Buckling deforms and deviates the thin-wall part from its original location, allowing the new layer to be deposited in an empty area, resulting in part failure.
 - o According to the result, buckling is caused by a correlation between the part geometry and stress in the build direction. In other words, as layers are deposited, the stress increases in the build direction until it exceeds the thin-wall threshold and buckles the wall.
 - o According to experimental and simulation results, thicker components are more resistant to in-process part failure. It was explained by the fact that thicker components

provide a larger surface area for material deposition. Moreover, thicker components have smaller slenderness ratios making them less prone to buckling.

- o As the part length increases, the compressive stresses are localized in the upper part corners, and the failures become less homogeneous and more localized. As a result, the buckling mode changes with the part geometry.

Based on the modelling and experimental results, the optimum LPBF processing parameter is determined. The preferred scanning strategy to increase limiting build height involves printing patterns with maximum vector length including interlayer rotation. It is shown that the vector length increases the LBH by 65% and rotation by 60%. In fact, using larger vector lengths minimizes residual stress in the build direction, and the interlayer rotation helps homogenize the residual stress.

9.2 Recommendations and Future Work

The experimental and simulation results, along with the results from literature, suggest using a rotational printing pattern with a short vector length for thicker components to increase the final part quality. Suggestions and future studies are provided below:

- The consideration of anisotropic thermo-mechanical material properties for the simulations.
- Developing a framework that covers different geometries.
- Conducting a parametric study to increase the computational processing speed.
- Studying the effects of laser power, scan speed, printing pattern on residual stress and evaluating their contributions towards LBH.

References

- [1] A. J. Favaloro, B. Brenken, E. Barocio, and R. B. Pipes, “Simulation of polymeric composites additive manufacturing using Abaqus,” *Sci. Age Exp.*, pp. 103–114, 2017.
- [2] R. C. Reed, “The physical metallurgy of nickel and its alloys,” *Superalloys-Fundamentals Appl.*, pp. 33–120, 2006.
- [3] P. Rochus, J.-Y. Plessier, M. Van Elsen, J.-P. Kruth, R. Carrus, and T. Dormal, “New applications of rapid prototyping and rapid manufacturing (RP/RM) technologies for space instrumentation,” *Acta Astronaut.*, vol. 61, no. 1–6, pp. 352–359, 2007.
- [4] A. T. Clare, P. R. Chalker, S. Davies, C. J. Sutcliffe, and S. Tsopanos, “Selective laser melting of high aspect ratio 3D nickel–titanium structures two way trained for MEMS applications,” *Int. J. Mech. Mater. Des.*, vol. 4, no. 2, pp. 181–187, 2008.
- [5] B. Vandenbroucke and J. Kruth, “Selective laser melting of biocompatible metals for rapid manufacturing of medical parts,” *Rapid Prototyp. J.*, 2007.
- [6] M. Wong, S. Tsopanos, C. J. Sutcliffe, and I. Owen, “Selective laser melting of heat transfer devices,” *Rapid Prototyp. J.*, 2007.
- [7] C. Li, C. H. Fu, Y. B. Guo, and F. Z. Fang, “A multiscale modeling approach for fast prediction of part distortion in selective laser melting,” *J. Mater. Process. Technol.*, vol. 229, pp. 703–712, 2016.
- [8] Q. Chen *et al.*, “An inherent strain based multiscale modeling framework for simulating part-scale residual deformation for direct metal laser sintering,” *Addit. Manuf.*, vol. 28, pp. 406–418, 2019.
- [9] A. Chakraborty, R. Tangestani, K. Esmati, T. Sabiston, L. Yuan, and É. Martin, “Mitigating Inherent Micro-Cracking in Laser Additively Manufactured René 108 Thin-Wall Components,” *Available SSRN 4150319*.
- [10] A. Chakraborty *et al.*, “In-process failure analysis of thin-wall structures made by laser powder bed fusion additive manufacturing,” *J. Mater. Sci. Technol.*, 2021.
- [11] J. Ding, “Thermo-mechanical analysis of wire and arc additive manufacturing process. School of Applied Science, Cranfield University.” Ph. D. thesis, 2012.
- [12] P. Rangaswamy *et al.*, “Residual stresses in LENS® components using neutron diffraction and contour method,” *Mater. Sci. Eng. A*, vol. 399, no. 1, pp. 72–83, 2005, doi: <https://doi.org/10.1016/j.msea.2005.02.019>.

- [13] F. Liu, X. Lin, G. Yang, M. Song, J. Chen, and W. Huang, "Microstructure and residual stress of laser rapid formed Inconel 718 nickel-base superalloy," *Opt. Laser Technol.*, vol. 43, no. 1, pp. 208–213, 2011, doi: <https://doi.org/10.1016/j.optlastec.2010.06.015>.
- [14] L. M. Sochalski-Kolbus *et al.*, "Comparison of residual stresses in Inconel 718 simple parts made by electron beam melting and direct laser metal sintering," *Metall. Mater. Trans. A*, vol. 46, no. 3, pp. 1419–1432, 2015.
- [15] K. An, L. Yuan, L. Dial, I. Spinelli, A. D. Stoica, and Y. Gao, "Neutron residual stress measurement and numerical modeling in a curved thin-walled structure by laser powder bed fusion additive manufacturing," *Mater. Des.*, vol. 135, pp. 122–132, 2017.
- [16] C. Li, M. F. Gouge, E. R. Denlinger, J. E. Irwin, and P. Michaleris, "Estimation of part-to-powder heat losses as surface convection in laser powder bed fusion," *Addit. Manuf.*, vol. 26, pp. 258–269, 2019.
- [17] Y. Yang, F. van Keulen, and C. Ayas, "A computationally efficient thermal model for selective laser melting," *Addit. Manuf.*, p. 100955, 2019.
- [18] N. E. Hodge, R. M. Ferencz, and R. M. Vignes, "Experimental comparison of residual stresses for a thermomechanical model for the simulation of selective laser melting," *Addit. Manuf.*, vol. 12, pp. 159–168, 2016.
- [19] J. Irwin and P. Michaleris, "A line heat input model for additive manufacturing," *J. Manuf. Sci. Eng.*, vol. 138, no. 11, p. 111004, 2016.
- [20] H. Bikas, P. Stavropoulos, and G. Chryssolouris, "Additive manufacturing methods and modelling approaches: a critical review," *Int. J. Adv. Manuf. Technol.*, vol. 83, no. 1–4, pp. 389–405, 2016.
- [21] I. Gibson, D. W. Rosen, and B. Stucker, *Additive manufacturing technologies*, vol. 17. Springer, 2014.
- [22] R. C. Reed and C. M. F. Rae, "Physical metallurgy of the nickel-based superalloys," in *Physical metallurgy*, Elsevier, 2014, pp. 2215–2290.
- [23] J. Ding, "Thermo-mechanical analysis of wire and arc additive manufacturing process," 2012.
- [24] T. Mukherjee, W. Zhang, and T. DebRoy, "An improved prediction of residual stresses and distortion in additive manufacturing," *Comput. Mater. Sci.*, vol. 126, pp. 360–372, 2017.
- [25] C. T. Sims and W. C. Hagel, *The Superalloys-vital high temperature gas turbine materials for aerospace and industrial power*, no. BOOK. John Wiley & Sons, 1972.
- [26] V. A. Popovich, E. V. Borisov, A. A. Popovich, V. S. Sufiiarov, D. V. Masaylo, and L. Alzina,

- “Functionally graded Inconel 718 processed by additive manufacturing: Crystallographic texture, anisotropy of microstructure and mechanical properties,” *Mater. Des.*, vol. 114, pp. 441–449, 2017.
- [27] E. L. Stevens, J. Toman, A. C. To, and M. Chmielus, “Variation of hardness, microstructure, and Laves phase distribution in direct laser deposited alloy 718 cuboids,” *Mater. Des.*, vol. 119, pp. 188–198, 2017.
- [28] B. Geddes, H. Leon, and X. Huang, *Superalloys: alloying and performance*. Asm International, 2010.
- [29] W. E. Frazier, “Metal Additive Manufacturing: A Review,” *J. Mater. Eng. Perform.*, vol. 23, no. 6, pp. 1917–1928, 2014, doi: 10.1007/s11665-014-0958-z.
- [30] B. Zheng, Y. Zhou, J. E. Smugeresky, J. M. Schoenung, and E. J. Lavernia, “Thermal behavior and microstructural evolution during laser deposition with laser-engineered net shaping: Part I. Numerical calculations,” *Metall. Mater. Trans. A*, vol. 39, no. 9, pp. 2228–2236, 2008.
- [31] D. T. Pham and S. S. Dimov, “Rapid prototyping processes,” in *Rapid Manufacturing*, Springer, 2001, pp. 19–42.
- [32] D. D. Gu, W. Meiners, K. Wissenbach, and R. Poprawe, “Laser additive manufacturing of metallic components: materials, processes and mechanisms,” *Int. Mater. Rev.*, vol. 57, no. 3, pp. 133–164, 2012.
- [33] A. du Plessis *et al.*, “Beautiful and functional: a review of biomimetic design in additive manufacturing,” *Addit. Manuf.*, 2019.
- [34] N. El-Bagoury and N. B. Superalloys, “Casting Technology, Metallurgy, Development, Properties and Applications,” *Int. J. Eng. Sci. Res. Technol.*, vol. 5, pp. 108–152, 2016.
- [35] L. N. Carter, C. Martin, P. J. Withers, and M. M. Attallah, “The influence of the laser scan strategy on grain structure and cracking behaviour in SLM powder-bed fabricated nickel superalloy,” *J. Alloys Compd.*, vol. 615, pp. 338–347, 2014.
- [36] L. L. Parimi, G. A. Ravi, D. Clark, and M. M. Attallah, “Microstructural and texture development in direct laser fabricated IN718,” *Mater. Charact.*, vol. 89, pp. 102–111, 2014.
- [37] M. M. Attallah, R. Jennings, X. Wang, and L. N. Carter, “Additive manufacturing of Ni-based superalloys: The outstanding issues,” *MRS Bull.*, vol. 41, no. 10, pp. 758–764, 2016.
- [38] A. Ahmed, A. Majeed, Z. Atta, and G. Jia, “Dimensional quality and distortion analysis of thin-walled alloy parts of AlSi10Mg manufactured by selective laser melting,” *J. Manuf. Mater. Process.*, vol. 3, no. 2, p. 51, 2019.

- [39] R. Tangestani, “Investigation of the effective parameters and procedures to reduce residual stress of parts produced by wire arc additive manufacturing (WAAM),” Sharif University, 2017.
- [40] L. E. Criales, Y. M. Arisoy, and T. Özel, “Sensitivity analysis of material and process parameters in finite element modeling of selective laser melting of Inconel 625,” *Int. J. Adv. Manuf. Technol.*, vol. 86, no. 9–12, pp. 2653–2666, 2016.
- [41] V. Abaqus, “6.14 Documentation,” *Dassault Syst. Simulia Corp.*, vol. 651, pp. 2–6, 2014.
- [42] S. M. Tawfik, M. N. A. Nasr, and H. A. El Gamal, “Finite element modelling for part distortion calculation in selective laser melting,” *Alexandria Eng. J.*, vol. 58, no. 1, pp. 67–74, 2019.
- [43] M. Gouge and P. Michaleris, *Thermo-mechanical modeling of additive manufacturing*. Butterworth-Heinemann, 2017.
- [44] Y. Bao and T. Wierzbicki, “On the cut-off value of negative triaxiality for fracture,” *Eng. Fract. Mech.*, vol. 72, no. 7, pp. 1049–1069, 2005.
- [45] K. Danas and P. P. Castañeda, “Influence of the Lode parameter and the stress triaxiality on the failure of elasto-plastic porous materials,” *Int. J. Solids Struct.*, vol. 49, no. 11–12, pp. 1325–1342, 2012.
- [46] M. Dunand and D. Mohr, “On the predictive capabilities of the shear modified Gurson and the modified Mohr–Coulomb fracture models over a wide range of stress triaxialities and Lode angles,” *J. Mech. Phys. Solids*, vol. 59, no. 7, pp. 1374–1394, 2011.
- [47] I. Barsoum and J. Faleskog, “Micromechanical analysis on the influence of the Lode parameter on void growth and coalescence,” *Int. J. Solids Struct.*, vol. 48, no. 6, pp. 925–938, 2011.
- [48] J. C. Lippold, S. D. Kiser, and J. N. DuPont, *Welding metallurgy and weldability of nickel-base alloys*. John Wiley & Sons, 2011.
- [49] J. H. Robinson, I. R. T. Ashton, E. Jones, P. Fox, and C. Sutcliffe, “The effect of hatch angle rotation on parts manufactured using selective laser melting,” *Rapid Prototyp. J.*, vol. 25, no. 2, pp. 289–298, 2019.
- [50] M. Bayat *et al.*, “Keyhole-induced porosities in Laser-based Powder Bed Fusion (L-PBF) of Ti6Al4V: High-fidelity modelling and experimental validation,” *Addit. Manuf.*, vol. 30, p. 100835, 2019.
- [51] N. Shen and K. Chou, “Thermal modeling of electron beam additive manufacturing process: powder sintering effects,” in *ASME 2012 International Manufacturing Science and Engineering Conference collocated with the 40th North American Manufacturing Research Conference and in participation with the International Conference on Tribology Materials and Processing*, 2012, pp. 287–295.

- [52] J. A. Van Den Avyle, J. A. Brooks, and A. C. Powell, "Reducing defects in remelting processes for high-performance alloys," *Jom*, vol. 50, no. 3, pp. 22–25, 1998.
- [53] B. Cheng and K. Chou, "Melt pool evolution study in selective laser melting," in *26th Annual International Solid Freeform Fabrication Symposium-An Additive Manufacturing Conference, Austin, TX, USA*, 2015, pp. 1182–1194.
- [54] D. Rosenthal, "Etude théorique du régime thermique pendant la soudure à l'arc," *Congrès Natl. des Sci. Comptes Rendus Bruxelles*, vol. 2, p. 1277, 1935.
- [55] J. Goldak, A. Chakravarti, and M. Bibby, "A new finite element model for welding heat sources," *Metall. Trans. B*, vol. 15, no. 2, pp. 299–305, 1984.
- [56] C. S. Wu, H. G. Wang, and Y. M. Zhang, "A new heat source model for keyhole plasma arc welding in FEM analysis of the temperature profile," *Weld. JOURNAL-NEW YORK-*, vol. 85, no. 12, p. 284, 2006.
- [57] Z. Zhang *et al.*, "3-Dimensional heat transfer modeling for laser powder-bed fusion additive manufacturing with volumetric heat sources based on varied thermal conductivity and absorptivity," *Opt. Laser Technol.*, vol. 109, pp. 297–312, 2019.
- [58] A. V. Gusarov, I. Yadroitsev, P. Bertrand, and I. Smurov, "Model of radiation and heat transfer in laser-powder interaction zone at selective laser melting," *J. Heat Transfer*, vol. 131, no. 7, 2009.
- [59] L. Ladani, J. Romano, W. Brindley, and S. Burlatsky, "Effective liquid conductivity for improved simulation of thermal transport in laser beam melting powder bed technology," *Addit. Manuf.*, vol. 14, pp. 13–23, 2017.
- [60] S. Liu, H. Zhu, G. Peng, J. Yin, and X. Zeng, "Microstructure prediction of selective laser melting AlSi10Mg using finite element analysis," *Mater. Des.*, vol. 142, pp. 319–328, 2018.
- [61] D. Rosenthal, "The theory of moving sources of heat and its application of metal treatments," *Trans. ASME*, vol. 68, pp. 849–866, 1946.
- [62] L. Zhang, E. W. Reutzel, and P. Michaleris, "Finite element modeling discretization requirements for the laser forming process," *Int. J. Mech. Sci.*, vol. 46, no. 4, pp. 623–637, 2004.
- [63] V. Buljak and G. Maier, "Identification of residual stresses by instrumented elliptical indentation and inverse analysis," *Mech. Res. Commun.*, vol. 41, pp. 21–29, 2012.
- [64] A. Hussein, L. Hao, C. Yan, and R. Everson, "Finite element simulation of the temperature and stress fields in single layers built without-support in selective laser melting," *Mater. Des.*, vol. 52, pp. 638–647, 2013.

- [65] L.-E. Loh *et al.*, “Numerical investigation and an effective modelling on the Selective Laser Melting (SLM) process with aluminium alloy 6061,” *Int. J. Heat Mass Transf.*, vol. 80, pp. 288–300, 2015.
- [66] Z. Luo and Y. Zhao, “A survey of finite element analysis of temperature and thermal stress fields in powder bed fusion Additive Manufacturing,” *Addit. Manuf.*, vol. 21, pp. 318–332, 2018.
- [67] I. A. Roberts, C. J. Wang, R. Esterlein, M. Stanford, and D. J. Mynors, “A three-dimensional finite element analysis of the temperature field during laser melting of metal powders in additive layer manufacturing,” *Int. J. Mach. Tools Manuf.*, vol. 49, no. 12–13, pp. 916–923, 2009.
- [68] J. Zhang and R. F. Singer, “Effect of grain-boundary characteristics on castability of nickel-base superalloys,” *Metall. Mater. Trans. A*, vol. 35, no. 3, pp. 939–946, 2004.
- [69] G. W. Krutz and L. J. Segerlind, “Finite element analysis of welded structures,” SAE Technical Paper, 1976.
- [70] Y. Li, K. Zhou, P. Tan, S. B. Tor, C. K. Chua, and K. F. Leong, “Modeling temperature and residual stress fields in selective laser melting,” *Int. J. Mech. Sci.*, vol. 136, pp. 24–35, 2018.
- [71] V. A. Vinokurov, “Welding stresses and distortion,” *Br. Libr. Board*, 1977.
- [72] M. Labudovic, D. Hu, and R. Kovacevic, “A three dimensional model for direct laser metal powder deposition and rapid prototyping,” *J. Mater. Sci.*, vol. 38, no. 1, pp. 35–49, 2003, doi: 10.1023/A:1021153513925.
- [73] H. Liu, “Numerical analysis of thermal stress and deformation in multi-layer laser metal deposition process,” 2014.
- [74] M. Galati, A. Snis, and L. Iuliano, “Powder bed properties modelling and 3D thermo-mechanical simulation of the additive manufacturing Electron Beam Melting process,” *Addit. Manuf.*, p. 100897, 2019.
- [75] S. A. David and T. DebRoy, “Current issues and problems in welding science,” *Science (80-.)*, vol. 257, no. 5069, pp. 497–502, 1992.
- [76] A. Raghavan, H. L. Wei, T. A. Palmer, and T. DebRoy, “Heat transfer and fluid flow in additive manufacturing,” *J. Laser Appl.*, vol. 25, no. 5, p. 52006, 2013.
- [77] K. Shah, I. U. Haq, S. A. Shah, F. U. Khan, M. T. Khan, and S. Khan, “Experimental study of direct laser deposition of Ti-6Al-4V and Inconel 718 by using pulsed parameters,” *Sci. World J.*, vol. 2014, 2014.
- [78] Y. Li and D. Gu, “Thermal behavior during selective laser melting of commercially pure

- titanium powder: Numerical simulation and experimental study,” *Addit. Manuf.*, vol. 1, pp. 99–109, 2014.
- [79] D. Q. Zhang, Q. Z. Cai, J. H. Liu, L. Zhang, and R. D. Li, “Select laser melting of W–Ni–Fe powders: simulation and experimental study,” *Int. J. Adv. Manuf. Technol.*, vol. 51, no. 5–8, pp. 649–658, 2010.
- [80] S. Jayanath and A. Achuthan, “A computationally efficient finite element framework to simulate additive manufacturing processes,” *J. Manuf. Sci. Eng.*, vol. 140, no. 4, p. 41009, 2018.
- [81] Hibbett, Karlsson, and Sorensen, *ABAQUS/standard: User’s Manual*, vol. 1. Hibbett, Karlsson & Sorensen, 1998.
- [82] F. Hajjalizadeh and A. Ince, “Finite element–based numerical modeling framework for additive manufacturing process,” *Mater. Des. Process. Commun.*, vol. 1, no. 1, p. e28, 2019.
- [83] S. Kolossov, E. Boillat, R. Glardon, P. Fischer, and M. Locher, “3D FE simulation for temperature evolution in the selective laser sintering process,” *Int. J. Mach. Tools Manuf.*, vol. 44, no. 2–3, pp. 117–123, 2004.
- [84] J. Yin, H. Zhu, L. Ke, W. Lei, C. Dai, and D. Zuo, “Simulation of temperature distribution in single metallic powder layer for laser micro-sintering,” *Comput. Mater. Sci.*, vol. 53, no. 1, pp. 333–339, 2012.
- [85] S. Paul, I. Gupta, and R. K. Singh, “Characterization and modeling of microscale preplaced powder cladding via fiber laser,” *J. Manuf. Sci. Eng.*, vol. 137, no. 3, 2015.
- [86] P. Michaleris, L. Zhang, S. R. Bhide, and P. Marugabandhu, “Evaluation of 2D, 3D and applied plastic strain methods for predicting buckling welding distortion and residual stress,” *Sci. Technol. Weld. Join.*, vol. 11, no. 6, pp. 707–716, 2006.
- [87] H. Huang, J. Wang, L. Li, and N. Ma, “Prediction of laser welding induced deformation in thin sheets by efficient numerical modeling,” *J. Mater. Process. Technol.*, vol. 227, pp. 117–128, 2016.
- [88] N. Keller and V. Ploshikhin, “New method for fast predictions of residual stress and distortion of AM parts,” in *Solid freeform fabrication symposium*, 2014, vol. 25.
- [89] S. McFadden, J. P. Quinn, and A. Harley, “A REVIEW OF THERMAL MODELLING FOR METAL ADDITIVE MANUFACTURING PROCESSES: BASIC ANALYTICAL MODELS TO STATE-OF-THE-ART SOFTWARE PACKAGES.” 2018.
- [90] M. Bugatti and Q. Semeraro, “Limitations of the inherent strain method in simulating powder bed fusion processes,” *Addit. Manuf.*, vol. 23, pp. 329–346, 2018.

- [91] M. F. Zaeh and G. Branner, “Investigations on residual stresses and deformations in selective laser melting,” *Prod. Eng.*, vol. 4, no. 1, pp. 35–45, 2010.
- [92] M. Gouge, E. Denlinger, J. Irwin, C. Li, and P. Michaleris, “Experimental Validation of Thermo-mechanical Part-Scale Modeling for Laser Powder Bed Fusion Processes,” *Addit. Manuf.*, 2019.
- [93] D. Pal, N. Patil, K. Zeng, and B. Stucker, “An integrated approach to additive manufacturing simulations using physics based, coupled multiscale process modeling,” *J. Manuf. Sci. Eng.*, vol. 136, no. 6, 2014.
- [94] M. M. Francois *et al.*, “Modeling of additive manufacturing processes for metals: Challenges and opportunities,” *Curr. Opin. Solid State Mater. Sci.*, vol. 21, no. LA-UR-16-24513; SAND-2017-6832J, 2017.
- [95] X. Liang, L. Cheng, Q. Chen, Q. Yang, and A. C. To, “A modified method for estimating inherent strains from detailed process simulation for fast residual distortion prediction of single-walled structures fabricated by directed energy deposition,” *Addit. Manuf.*, vol. 23, pp. 471–486, 2018.
- [96] R. Tangestani, G. H. Farrahi, M. Shishegar, B. P. Aghchekandi, S. Ganguly, and A. Mehmanparast, “Effects of Vertical and Pinch Rolling on Residual Stress Distributions in Wire and Arc Additively Manufactured Components,” *J. Mater. Eng. Perform.*, pp. 1–12, 2020.
- [97] Y. P. Yang, M. Jamshidinia, P. Boulware, and S. M. Kelly, “Prediction of microstructure, residual stress, and deformation in laser powder bed fusion process,” *Comput. Mech.*, vol. 61, no. 5, pp. 599–615, 2018.
- [98] W. E. King *et al.*, “Laser powder bed fusion additive manufacturing of metals; physics, computational, and materials challenges,” *Appl. Phys. Rev.*, vol. 2, no. 4, p. 41304, 2015.
- [99] P. S. Cook and A. B. Murphy, “Simulation of Melt Pool Behaviour during Additive Manufacturing: Underlying Physics and Progress,” *Addit. Manuf.*, p. 100909, 2019.
- [100] L. Zhu, Z. F. Xu, P. Liu, and Y. F. Gu, “Effect of processing parameters on microstructure of laser solid forming Inconel 718 superalloy,” *Opt. Laser Technol.*, vol. 98, pp. 409–415, 2018.
- [101] S. S. Sih and J. W. Barlow, “Measurement and prediction of the thermal conductivity of powders at high temperatures,” *Solid Free. Fabr.*, vol. 321, 1994.
- [102] A. Thatte, A. Loghin, E. Martin, V. Dheeradhada, Y. Shin, and B. Ananthasayanam, “Multi-Scale Coupled Physics Models and Experiments for Performance and Life Prediction of Supercritical CO₂ Turbomachinery Components,” 2016.
- [103] A. Thatte, E. Martin, and T. Hanlon, “A Novel Experimental Method for LCF Measurement of

Nickel Base Super Alloys in High Pressure High Temperature Supercritical CO₂,” in *Turbo Expo: Power for Land, Sea, and Air*, 2017, vol. 50961, p. V009T38A030.

- [104] J. C. Stinville *et al.*, “Fatigue deformation in a polycrystalline nickel base superalloy at intermediate and high temperature: Competing failure modes,” *Acta Mater.*, vol. 152, pp. 16–33, 2018.
- [105] T. Keller *et al.*, “Application of finite element, phase-field, and CALPHAD-based methods to additive manufacturing of Ni-based superalloys,” *Acta Mater.*, vol. 139, pp. 244–253, 2017.
- [106] P. Kieruj, D. Przystacki, and T. Chwalczuk, “Determination of emissivity coefficient of heat-resistant super alloys and cemented carbide,” *Arch. Mech. Technol. Mater.*, vol. 36, 2016.
- [107] Y. S. Touloukian, “Thermal conductivity-metallic elements and alloys,” *Thermophys. Prop. matter*, vol. 1, 1970.
- [108] Y. S. Touloukian and E. H. Buyco, *Specific heat: metallic elements and alloys*. New York: IFI/Plenum, 1970.
- [109] P. Promoppatum and A. D. Rollett, “Influence of material constitutive models on thermomechanical behaviors in the laser powder bed fusion of Ti-6Al-4V,” *Addit. Manuf.*, vol. 37, p. 101680, 2021.
- [110] C. Baykasoglu, O. Akyildiz, D. Candemir, Q. Yang, and A. C. To, “Predicting microstructure evolution during directed energy deposition additive manufacturing of Ti-6Al-4V,” *J. Manuf. Sci. Eng.*, vol. 140, no. 5, 2018.
- [111] A. Olleak and Z. Xi, “Finite element modeling of the selective laser melting process for Ti-6Al-4V,” *Solid Free. Fabr. 2018 Proc. 29th Annu. Int.*, pp. 1710–1720, 2018.
- [112] A. Anca, V. D. Fachinotti, G. Escobar-Palafox, and A. Cardona, “Computational modelling of shaped metal deposition,” *Int. J. Numer. Methods Eng.*, vol. 85, no. 1, pp. 84–106, 2011.
- [113] M. S. Rahman, P. J. Schilling, P. D. Herrington, and U. K. Chakravarty, “Thermofluid Properties of Ti-6Al-4V Melt Pool in Powder-Bed Electron Beam Additive Manufacturing,” *J. Eng. Mater. Technol.*, vol. 141, no. 4, 2019.
- [114] E. Kundakcıođlu, I. Lazoglu, Ö. Poyraz, E. Yasa, and N. Ciziciođlu, “Thermal and molten pool model in selective laser melting process of Inconel 625,” *Int. J. Adv. Manuf. Technol.*, vol. 95, no. 9, pp. 3977–3984, 2018.
- [115] L. Cao and X. Yuan, “Study on the Numerical Simulation of the SLM Molten Pool Dynamic Behavior of a Nickel-Based Superalloy on the Workpiece Scale,” *Materials (Basel)*, vol. 12, no. 14, p. 2272, 2019.

- [116] S. Ghosh *et al.*, “Single-track melt-pool measurements and microstructures in Inconel 625,” *Jom*, vol. 70, no. 6, pp. 1011–1016, 2018.
- [117] M. Cloots, P. J. Uggowitzer, and K. Wegener, “Investigations on the microstructure and crack formation of IN738LC samples processed by selective laser melting using Gaussian and doughnut profiles,” *Mater. Des.*, vol. 89, pp. 770–784, 2016.
- [118] S. A. Khairallah, A. T. Anderson, A. Rubenchik, and W. E. King, “Laser powder-bed fusion additive manufacturing: Physics of complex melt flow and formation mechanisms of pores, spatter, and denudation zones,” *Acta Mater.*, vol. 108, pp. 36–45, 2016.
- [119] L. N. Carter, M. M. Attallah, and R. C. Reed, “Laser powder bed fabrication of nickel-base superalloys: influence of parameters; characterisation, quantification and mitigation of cracking,” *Superalloys*, vol. 2012, no. 6, pp. 2826–2834, 2012.
- [120] P. Kontis *et al.*, “Atomic-scale grain boundary engineering to overcome hot-cracking in additively-manufactured superalloys,” *Acta Mater.*, vol. 177, pp. 209–221, 2019.
- [121] L. N. Carter, “Selective laser melting of nickel superalloys for high temperature applications.” University of Birmingham, 2013.
- [122] C. Li, Z. Y. Liu, X. Y. Fang, and Y. B. Guo, “Residual stress in metal additive manufacturing,” *Procedia Cirp*, vol. 71, pp. 348–353, 2018.
- [123] A. E. Wessman, “Physical Metallurgy of Rene 65, a Next-Generation Cast and Wrought Nickel Superalloy for use in Aero Engine Components.” University of Cincinnati, 2016.
- [124] D. Grange, J. D. Bartout, B. Macquaire, and C. Colin, “Processing a non-weldable nickel-base superalloy by Selective Laser Melting: role of the shape and size of the melt pools on solidification cracking,” *Materialia*, vol. 12, p. 100686, 2020.
- [125] Y. Wang, J. Shi, and Y. Liu, “Competitive grain growth and dendrite morphology evolution in selective laser melting of Inconel 718 superalloy,” *J. Cryst. Growth*, vol. 521, pp. 15–29, 2019.
- [126] R. C. Reed, *The Superalloys: Fundamentals and Applications*. Cambridge: Cambridge University Press, 2006.
- [127] N. Eftekhari, W. Muhammad, F. Haftlang, A. Zarei-Hanzaki, and É. Martin, “Microstructural evolution and corrosion behavior of Sanicro 28 during thermomechanical processing,” *Mater. Today Commun.*, p. 101228, 2020.
- [128] Y. Lu *et al.*, “Study on the microstructure, mechanical property and residual stress of SLM Inconel-718 alloy manufactured by differing island scanning strategy,” *Opt. Laser Technol.*, vol. 75, no. Complete, pp. 197–206, 2015, doi: 10.1016/j.optlastec.2015.07.009.

- [129] A. Bandyopadhyay and K. D. Traxel, “Invited review article: Metal-additive manufacturing—Modeling strategies for application-optimized designs,” *Addit. Manuf.*, vol. 22, pp. 758–774, 2018.
- [130] P. J. Withers and H. Bhadeshia, “Residual stress. Part 1—measurement techniques,” *Mater. Sci. Technol.*, vol. 17, no. 4, pp. 355–365, 2001.
- [131] P. J. Withers and H. Bhadeshia, “Residual stress. Part 2—Nature and origins,” *Mater. Sci. Technol.*, vol. 17, no. 4, pp. 366–375, 2001.
- [132] I. Setien, M. Chiumenti, S. van der Veen, M. San Sebastian, F. Garcíandía, and A. Echeverría, “Empirical methodology to determine inherent strains in additive manufacturing,” *Comput. Math. with Appl.*, vol. 78, no. 7, pp. 2282–2295, 2019.
- [133] A. S. Tremsin *et al.*, “Monitoring residual strain relaxation and preferred grain orientation of additively manufactured Inconel 625 by in-situ neutron imaging,” *Addit. Manuf.*, vol. 46, p. 102130, 2021, doi: <https://doi.org/10.1016/j.addma.2021.102130>.
- [134] H. Huang, Y. Wang, J. Chen, and Z. Feng, “A Comparative Study of Layer Heating and Continuous Heating Methods on Prediction Accuracy of Residual Stresses in Selective Laser Melted Tube Samples,” *Integr. Mater. Manuf. Innov.*, vol. 10, no. 2, pp. 218–230, 2021, doi: [10.1007/s40192-021-00217-4](https://doi.org/10.1007/s40192-021-00217-4).
- [135] R. Tangestani, T. Sabiston, A. Chakraborty, W. Muhammad, L. Yuan, and É. Martin, “An efficient track-scale model for laser powder bed fusion additive manufacturing: Part 1- thermal model,” *Front. Mater.*, 2021.
- [136] J. Robinson, I. Ashton, P. Fox, E. Jones, and C. Sutcliffe, “Determination of the effect of scan strategy on residual stress in laser powder bed fusion additive manufacturing,” *Addit. Manuf.*, vol. 23, pp. 13–24, 2018.
- [137] L. Scime and J. Beuth, “Melt pool geometry and morphology variability for the Inconel 718 alloy in a laser powder bed fusion additive manufacturing process,” *Addit. Manuf.*, vol. 29, p. 100830, 2019.
- [138] S. Taira, K. Tanaka, and T. Yamasaki, “A method of X-ray microbeam measurement of local stress and its application to fatigue crack growth problems,” *J. Soc. Mater. Sci.*, vol. 27, no. 294, pp. 251–256, 1978, doi: [10.2472/jsms.27.251](https://doi.org/10.2472/jsms.27.251).
- [139] D. Delbergue, D. Texier, M. Lévesque, and P. Bocher, “Comparison of two X-ray residual stress measurement methods: $\sin^2 \psi$ and $\cos \alpha$, through the determination of a martensitic steel X-ray elastic constant,” in *Residual Stresses 2016: ICRS-10*, 2016, vol. 2, pp. 55–60.
- [140] I. Serrano-Munoz *et al.*, “Scanning Manufacturing Parameters Determining the Residual Stress State in LPBF IN718 Small Parts,” *Adv. Eng. Mater.*, p. 2100158, 2021.

- [141] Z. Luo and Y. Zhao, “Numerical simulation of part-level temperature fields during selective laser melting of stainless steel 316L,” *Int. J. Adv. Manuf. Technol.*, vol. 104, no. 5, pp. 1615–1635, 2019.
- [142] T. P. Gabb, J. Gayda, P. T. Kantzos, T. Biles, and W. Konkel, “The tensile properties of advanced Nickel-based disk superalloys during quenching heat treatments,” 2001.
- [143] T. R. Walker, C. J. Bennett, T. L. Lee, and A. T. Clare, “A validated analytical-numerical modelling strategy to predict residual stresses in single-track laser deposited IN718,” *Int. J. Mech. Sci.*, vol. 151, pp. 609–621, 2019.
- [144] C. Chen, Z. Xiao, H. Zhu, and X. Zeng, “Distribution and evolution of thermal stress during multi-laser powder bed fusion of Ti-6Al-4 V alloy,” *J. Mater. Process. Technol.*, vol. 284, p. 116726, 2020, doi: <https://doi.org/10.1016/j.jmatprotec.2020.116726>.
- [145] Z. Xiao *et al.*, “Study of residual stress in selective laser melting of Ti6Al4V,” *Mater. Des.*, vol. 193, p. 108846, 2020.
- [146] J.-P. Kruth, J. Deckers, E. Yasa, and R. Wauthlé, “Assessing and comparing influencing factors of residual stresses in selective laser melting using a novel analysis method,” *Proc. Inst. Mech. Eng. Part B J. Eng. Manuf.*, vol. 226, no. 6, pp. 980–991, 2012.
- [147] L. Parry, I. A. Ashcroft, and R. D. Wildman, “Understanding the effect of laser scan strategy on residual stress in selective laser melting through thermo-mechanical simulation,” *Addit. Manuf.*, vol. 12, pp. 1–15, 2016.
- [148] R. Tangestani, T. Sabiston, A. Chakraborty, L. Yuan, N. Krutz, and É. Martin, “An efficient track-scale model for laser powder bed fusion additive manufacturing: Part 2- mechanical model,” *Front. Mater.*, 2021.
- [149] A. Chakraborty *et al.*, “Micro-cracking mechanism of RENÉ 108 thin-wall components built by laser powder bed fusion additive manufacturing,” *Mater. Today Commun.*, vol. 30, p. 103139, 2022, doi: <https://doi.org/10.1016/j.mtcomm.2022.103139>.
- [150] X. Quelennec, E. Martin, L. Jiang, and J. J. Jonas, “Work hardening and kinetics of dynamic recrystallization in hot deformed austenite,” in *Journal of Physics: Conference Series*, 2010, vol. 240, no. 1, p. 12082.
- [151] É. Martin, W. Muhammad, A. J. Detor, I. Spinelli, A. Wessman, and D. Wei, “‘Strain-annealed’ grain boundary engineering process investigated in Hastelloy-X,” *Materialia*, vol. 9, p. 100544, 2020.
- [152] W. J. Sames, F. A. List, S. Pannala, R. R. Dehoff, and S. S. Babu, “The metallurgy and processing science of metal additive manufacturing,” *Int. Mater. Rev.*, vol. 61, no. 5, pp. 315–360, 2016.

- [153] M. Ziaee and N. B. Crane, “Binder jetting: A review of process, materials, and methods,” *Addit. Manuf.*, vol. 28, pp. 781–801, 2019.
- [154] E. Martin, A. Natarajan, S. Kottilingam, and R. Batmaz, “Binder jetting of ‘Hard-to-Weld’ high gamma prime nickel-based superalloy RENÉ 108,” *Addit. Manuf.*, vol. 39, p. 101894, 2021.
- [155] W. Muhammad, R. Batmaz, A. Natarajan, and E. Martin, “Effect of binder jetting microstructure variability on low cycle fatigue behavior of 316L,” *Mater. Sci. Eng. A*, vol. 839, p. 142820, 2022.
- [156] D. Dev Singh, T. Mahender, and A. Raji Reddy, “Powder bed fusion process: A brief review,” *Mater. Today Proc.*, vol. 46, pp. 350–355, 2021, doi: <https://doi.org/10.1016/j.matpr.2020.08.415>.
- [157] A. Salmi, F. Calignano, M. Galati, and E. Atzeni, “An integrated design methodology for components produced by laser powder bed fusion (L-PBF) process,” *Virtual Phys. Prototyp.*, vol. 13, no. 3, pp. 191–202, Jul. 2018, doi: 10.1080/17452759.2018.1442229.
- [158] L. Cao, J. Li, J. Hu, H. Liu, Y. Wu, and Q. Zhou, “Optimization of surface roughness and dimensional accuracy in LPBF additive manufacturing,” *Opt. Laser Technol.*, vol. 142, p. 107246, 2021, doi: <https://doi.org/10.1016/j.optlastec.2021.107246>.
- [159] H. C. Taylor, E. A. Garibay, and R. B. Wicker, “Toward a common laser powder bed fusion qualification test artifact,” *Addit. Manuf.*, vol. 39, p. 101803, 2021.
- [160] S. Catchpole-Smith, N. Aboulkhair, L. Parry, C. Tuck, I. A. Ashcroft, and A. Clare, “Fractal scan strategies for selective laser melting of ‘unweldable’ nickel superalloys,” *Addit. Manuf.*, vol. 15, pp. 113–122, 2017.
- [161] M. Bayat *et al.*, “Part-scale thermo-mechanical modelling of distortions in Laser Powder Bed Fusion – Analysis of the sequential flash heating method with experimental validation,” *Addit. Manuf.*, vol. 36, p. 101508, 2020, doi: <https://doi.org/10.1016/j.addma.2020.101508>.
- [162] Ł. Rakoczy *et al.*, “Characterization of γ' precipitates in cast Ni-based superalloy and their behaviour at high-homologous temperatures studied by TEM and in Situ XRD,” *Materials (Basel)*, vol. 13, no. 10, p. 2397, 2020.
- [163] Y. Wang, S. Roy, H. Choi, and T. Rimon, “Cracking suppression in additive manufacturing of hard-to-weld nickel-based superalloy through layer-wise ultrasonic impact peening,” *J. Manuf. Process.*, vol. 80, pp. 320–327, 2022, doi: <https://doi.org/10.1016/j.jmapro.2022.05.041>.
- [164] M. Ghasri-Khouzani *et al.*, “Experimental measurement of residual stress and distortion in additively manufactured stainless steel components with various dimensions,” *Mater. Sci. Eng. A*, vol. 707, pp. 689–700, 2017, doi: <https://doi.org/10.1016/j.msea.2017.09.108>.

- [165] M. Mostafaei and S. M. Abbasi, "Solutioning and solidification process control in Ta-modified CM247 LC superalloy," *J. Mater. Process. Technol.*, vol. 231, pp. 113–124, 2016.
- [166] R. Przeliorz, F. Binczyk, P. Gradoń, M. Góral, and T. Mikuszewski, "Evaluation of Heat Capacity and Resistance to Cyclic Oxidation of Nickel Superalloys," *Arch. Foundry Eng.*, vol. 14, 2014.
- [167] A. J. Torroba *et al.*, "Investment casting of nozzle guide vanes from nickel-based superalloys: part I—thermal calibration and porosity prediction," *Integr. Mater. Manuf. Innov.*, vol. 3, no. 1, pp. 344–368, 2014.
- [168] R. Pramod, S. Mohan Kumar, A. Rajesh Kannan, N. Siva Shanmugam, and R. Tangestani, "Fabrication of gas metal arc welding based wire plus arc additive manufactured 347 stainless steel structure: behavioral analysis through experimentation and finite element method," *Met. Mater. Int.*, vol. 28, no. 1, pp. 307–321, 2022.
- [169] L.-E. Lindgren, A. Lundbäck, M. Fisk, R. Pederson, and J. Andersson, "Simulation of additive manufacturing using coupled constitutive and microstructure models," *Addit. Manuf.*, vol. 12, pp. 144–158, 2016.
- [170] J. Thorborg, P. Esser, and M. Bayat, "Thermomechanical modeling of additively manufactured structural parts - different approaches on the macroscale," *IOP Conf. Ser. Mater. Sci. Eng.*, vol. 861, no. 1, p. 12008, 2020, doi: 10.1088/1757-899x/861/1/012008.
- [171] T. Q. Phan *et al.*, "Elastic residual strain and stress measurements and corresponding part deflections of 3D additive manufacturing builds of IN625 AM-bench artifacts using neutron diffraction, synchrotron X-ray diffraction, and contour method," *Integr. Mater. Manuf. Innov.*, vol. 8, no. 3, pp. 318–334, 2019.
- [172] E. M. R Tangestani, A Chakraborty, T Sabiston, "Interdependent influences of the laser power and printing pattern on residual stresses in laser powder bed fusion additive manufacturing," in *Proceedings M2D2022 - 9th International Conference on Mechanics and Materials in Design*, 2022, pp. 879–884.
- [173] D. W. A. Rees, *Mechanics of optimal structural design: minimum weight structures*. John Wiley & Sons, 2009.
- [174] A. C. Ugural, *Stresses in beams, plates, and shells*. CRC press, 2009.